

We greatly value the careful reading and the detailed comments provided by the referees. The responses to the comments of referee 1 in our direct reply (shown below) and within the revised manuscript (see marked copy) are provided. The pages and lines indicated below correspond to those in the marked copy.

Response to Referee 1 (Referees' comments are italicized)

1. Referee comment: *“The authors have well addressed my comments for an earlier version of manuscript except for the one on pH definition. The revised manuscript says that “ γ_{H^+} is the molarity-based hydronium ion activity coefficient (assumed to be 1), H_{aq}^+ (mole L⁻¹) is the molar concentration of hydronium ions in particle water (i.e., pH is calculated in terms of molarity)”. My understanding is that the molarity (or molar concentration) is defined on the basis of volume of the solution instead of that of the water. H_{aq}^+ calculated by ISORROPIA is actually the molality (mole kg⁻¹ water). Please correct me if I was wrong. See more here: https://en.wikipedia.org/wiki/Molar_concentration”*

Author response: The referee is correct, and we have changed the manuscript to state that it is molality-based:

Page 10 line 273: “Since most thermodynamic equilibrium models (e.g., ISORROPIA-II, E-AIM) do not report liquid concentrations, but instead report species in terms of concentration per volume of air (e.g., $\mu\text{g m}^{-3}$, $\mu\text{mol m}^{-3}$), we have calculated the particle pH by:

$$pH = -\log_{10} \gamma_{H^+} H_{aq}^+ = -\log_{10} \frac{1000 \gamma_{H^+} H_{air}^+}{W_i + W_o} \cong -\log_{10} \frac{1000 \gamma_{H^+} H_{air}^+}{W_i} \quad (1b)$$

where γ_{H^+} is the hydronium ion activity coefficient (assumed to be 1), H_{aq}^+ is the concentration of hydronium ions in particle water in mole L⁻¹ (i.e., the density of water is assumed to be 1000 kg m⁻³, and so pH is calculated in terms of molality), H_{air}^+ ($\mu\text{g m}^{-3}$) is the hydronium ion concentration per volume of air, and W_i and W_o ($\mu\text{g m}^{-3}$) are the bulk particle water concentrations associated with inorganic and organic species per volume of air, respectively. In equation 1b, the molecular weight of H⁺ is taken as 1 g mole⁻¹, and 1000 is the factor needed for unit conversion of g L⁻¹ to $\mu\text{g m}^{-3}$. H_{air}^+ and W_i are outputs of the ISORROPIA-II model.”

The referee is correct in stating that H_{aq}^+ has units of molality (mol kg⁻¹). However, H_{aq}^+ is not reported by ISORROPIA but is defined in equation 1b. As stated in the manuscript, ISORROPIA report species in terms of concentration per volume of air (e.g., $\mu\text{g m}^{-3}$, $\mu\text{mol m}^{-3}$). H_{air}^+ and W_i are outputs of the ISORROPIA model, and they are expressed in terms of $\mu\text{g m}^{-3}$ by ISORROPIA. In using H_{air}^+ and W_i in Equation 1b to calculate the aerosol pH, we are defining H_{aq}^+ as a molality-based concentration.

We refer the referee to page 8 of the User's Manual found on the ISORROPIA website (http://isorropia.eas.gatech.edu/index.php?title=User%27s_Manual) for more information regarding the units used by ISORROPIA.

2. Referee comment: *“I have another minor comment on this change made in the revised manuscript: Page 25 line 791: “In addition, formic and acetic acids may not be internally mixed with most of the other PM₁ aerosol components (e.g., SO₄²⁻, NO₃⁻, NH₄⁺, CH₃CO₂H), and thus are not associated with acidic aerosols, as assumed above.” What does “CH₃CO₂H” mean here?”*

Author response: CH₃COOH is the chemical formula of acetic acid. We meant to write C₂O₄²⁻, chemical formula of oxalate, which has been shown to be internally mixed with PM₁ aerosol components SO₄²⁻, NO₃⁻, NH₄⁺ in section 3.5.1 of our manuscript. This is corrected in the revised manuscript:

Page 25 line 717: “In addition, formic and acetic acids may not be internally mixed with most of the other PM₁ aerosol components (e.g., SO₄²⁻, NO₃⁻, NH₄⁺, C₂O₄²⁻), and thus are not associated with acidic aerosols, as assumed above.”

Additional minor revisions

1. The affiliation of the first author was updated.
2. We changed the range of the x-axis of graphs shown in Figs. 4, 7, 8, S12 and S13. The x-axis of the previous version of these graphs had their range starting from pH value -2. The x-axis of the revised version of these graphs have their range starting from pH value -1. We made these changes because the particle pH of ambient aerosol does not go below -1. Note that these changes do not affect our results.

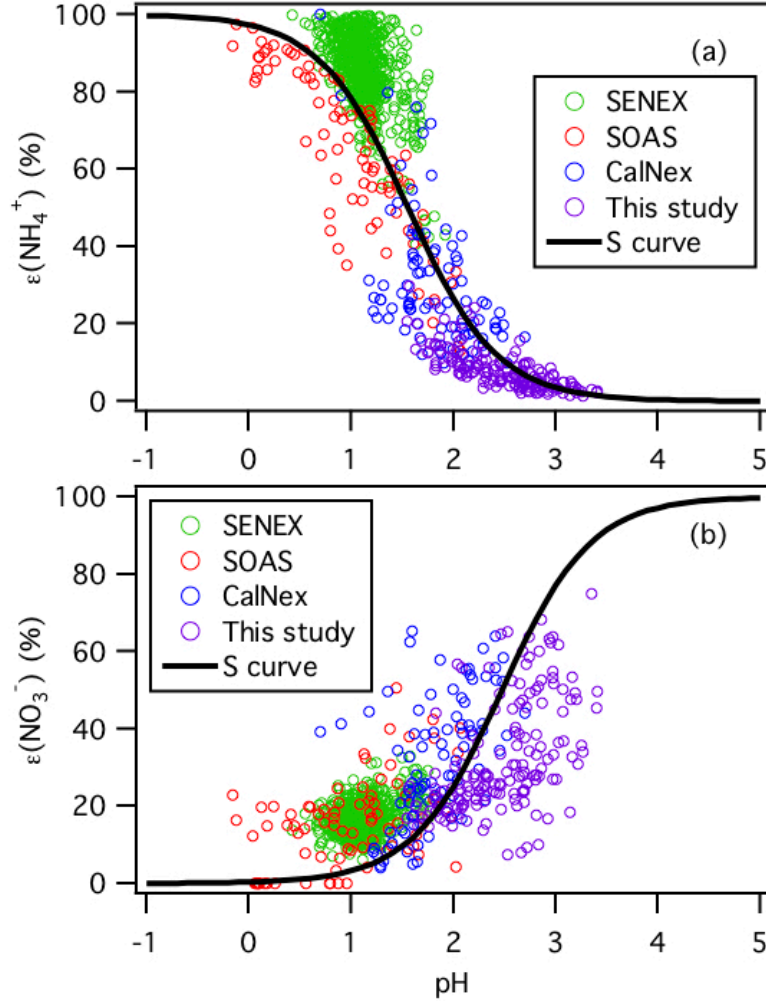


Figure 4: Analytically calculated S curves of $\epsilon(\text{NH}_4^+)$ and $\epsilon(\text{NO}_3^-)$ and ambient data plotted against ISORROPIA-predicted particle pH for this study, SENEX, SOAS and CalNex. For the ambient datasets, a narrow range of W_i (1 to 4 $\mu\text{g m}^{-3}$) and temperature (15 to 25 $^\circ\text{C}$) are selected to be close to the analytical calculation input (i.e., $W_i = 2.5 \mu\text{g m}^{-3}$ and temperature = 20 $^\circ\text{C}$). Similar to Guo et al. (2017a), $\gamma_{\text{NH}_4^+} = 1$ and $\gamma_{\text{H}^+ - \text{NO}_3^-} = \sqrt{\gamma_{\text{H}^+} \gamma_{\text{NO}_3^-}} = 0.28$ are used for the analytically calculated S curves.

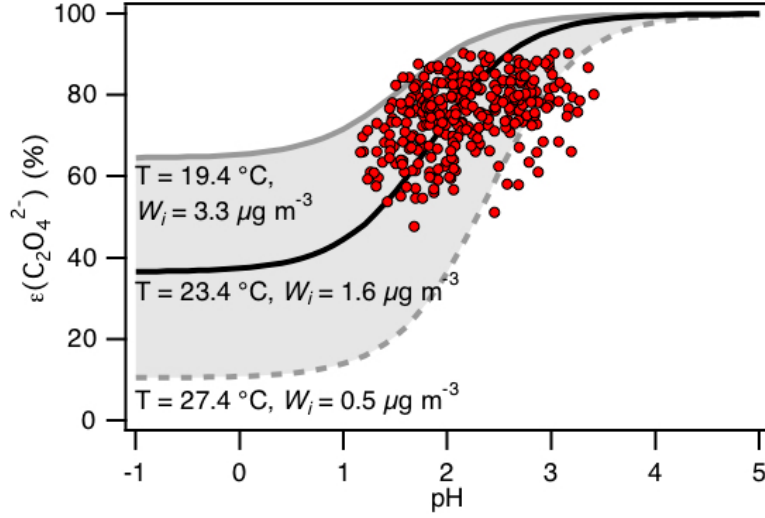


Figure 7: Analytically calculated S curve of $\varepsilon(\text{C}_2\text{O}_4^{2-})$ and ambient data from 13 September to 6 October 2016 plotted against ISORROPIA-predicted particle pH. For the ambient data, a range in W_i (0.5 to $4 \mu\text{g m}^{-3}$) and temperature (15 to $31 \text{ }^\circ\text{C}$) are chosen to be close to the analytically calculated outputs. For the analytically calculated S curves, we used $\gamma_{\text{C}_2\text{H}_2\text{O}_4} = 0.0492$ (AIOMFAC predicted). We also assumed that $\gamma_{\text{H}^+} + \gamma_{\text{C}_2\text{HO}_4^-} = \gamma_{\text{H}^+} + \gamma_{\text{NO}_3^-}$, and used the ISORROPIA-predicted $\gamma_{\text{H}^+} + \gamma_{\text{NO}_3^-} = \sqrt{\gamma_{\text{H}^+} \gamma_{\text{NO}_3^-}} = 0.265$. The black line is the S curve calculated using the selected time period's average temperature ($23.4 \pm 4.0 \text{ }^\circ\text{C}$) and W_i ($1.6 \pm 1.7 \mu\text{g m}^{-3}$). The grey lines are S curves calculated using one standard deviation from the average temperature and W_i (i.e., temperature = $27.4 \text{ }^\circ\text{C}$ and $W_i = 0.5 \mu\text{g m}^{-3}$ for dotted grey line, temperature = $19.4 \text{ }^\circ\text{C}$ and $W_i = 3.3 \mu\text{g m}^{-3}$ for solid grey line).

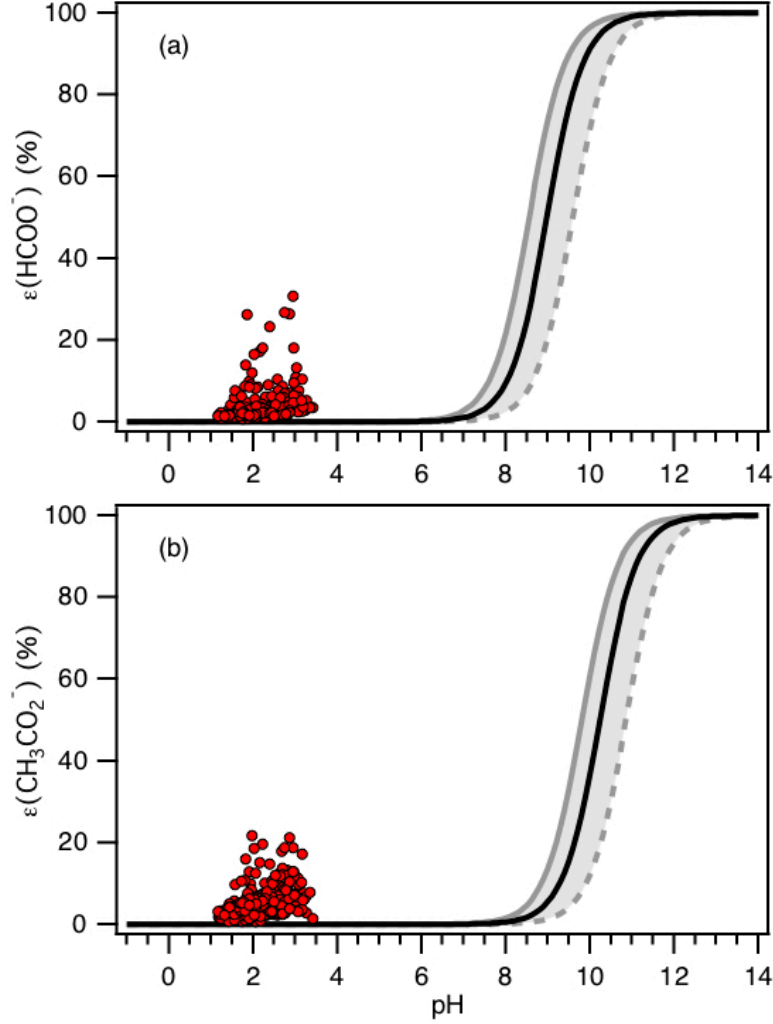


Figure 8: Analytically calculated S curves of $\varepsilon(\text{HCOO}^-)$ and $\varepsilon(\text{CH}_3\text{CO}_2^-)$ (solid black lines) and ambient data from 13 September to 6 October 2016 plotted against ISORROPIA-predicted particle pH (shown in panels (a) and (b), respectively). For the ambient data, a narrow range in W_i (0.5 to $4 \mu\text{g m}^{-3}$) and RH (20 to 90 %) is chosen to be close to the analytically calculated outputs. For the analytically calculated S curves, we used $\gamma_{\text{HCOOH}} = 0.334$ and $\gamma_{\text{CH}_3\text{COOH}} = 2.150$ (AIOMFAC predicted). We also assumed that $\gamma_{\text{H}^+}\gamma_{\text{HCOO}^-} = \gamma_{\text{H}^+}\gamma_{\text{CH}_3\text{COO}^-} = \gamma_{\text{H}^+}\gamma_{\text{NO}_3^-}$, and used the ISORROPIA-predicted $\gamma_{\text{H}^+-\text{NO}_3^-} = \sqrt{\gamma_{\text{H}^+}\gamma_{\text{NO}_3^-}} = 0.265$. The black lines are S curves calculated using the selected time period's average temperature ($23.4 \pm 4.0 \text{ }^\circ\text{C}$) and W_i ($1.6 \pm 1.7 \mu\text{g m}^{-3}$). The grey lines are S curves calculated using one standard deviation from the average temperature and W_i (i.e., temperature = $27.4 \text{ }^\circ\text{C}$ and $W_i = 0.5 \mu\text{g m}^{-3}$ for dotted grey line, temperature = $19.4 \text{ }^\circ\text{C}$ and $W_i = 3.3 \mu\text{g m}^{-3}$ for solid grey line).

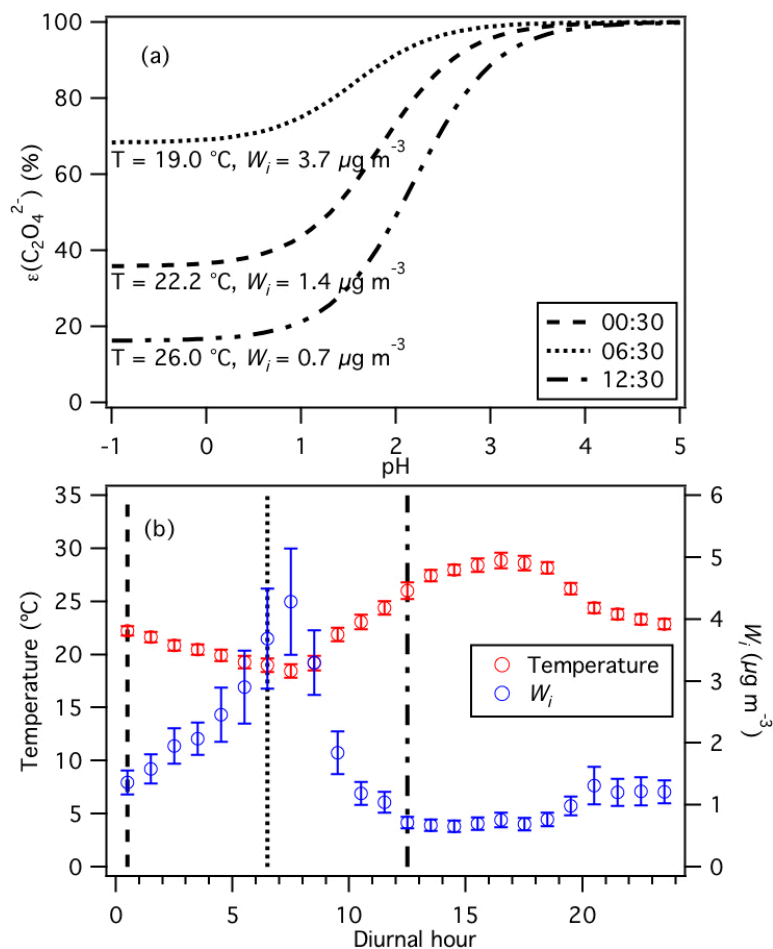


Figure S12: (a) Analytically calculated S curves of $\epsilon(\text{C}_2\text{O}_4^{2-})$ at different times of the day: 00:30, 06:30 and 12:30. These S curves are calculated using values obtained from (b) the diurnal profiles of temperature and W_i . The set of 1-hour average temperatures and W_i at diurnal hours 00:30, 06:30 and 12:30 is used to calculate each S curve shown in panel (a). Similar to Fig. 7, we used $\gamma_{\text{C}_2\text{H}_2\text{O}_4} = 0.0492$ (AIOMFAC predicted) and assumed that $\gamma_{\text{H}^+ - \text{NO}_3^-} = \sqrt{\gamma_{\text{H}^+} \gamma_{\text{NO}_3^-}} = \sqrt{\gamma_{\text{H}^+} \gamma_{\text{C}_2\text{HO}_4^-}} = 0.265$ (ISORROPIA-II predicted) to generate these S curves.

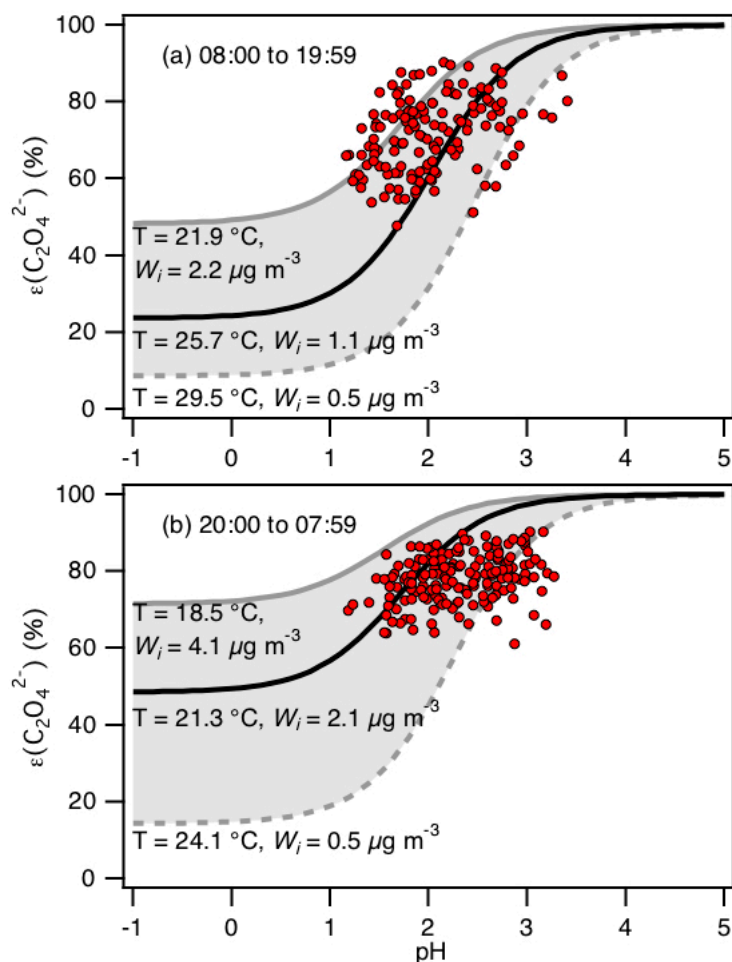


Figure S13: Analytically calculated S curve of $\varepsilon(\text{C}_2\text{O}_4^{2-})$ and ambient data from 13 September to 6 October 2016 plotted against ISORROPIA-predicted particle pH. For the ambient data, a narrow range in W_i (0.5 to $4 \mu\text{g m}^{-3}$) and RH (20 to 90%) is chosen to be close to the analytically calculated outputs. We divided the ambient data into two sets: panel (a) 08:00 to 19:59, and panel (b) 20:00 to 07:59. For both analytically calculated S curves, we used $\gamma_{\text{C}_2\text{H}_2\text{O}_4} = 0.0492$ (AIOMFAC predicted). We also assumed that $\gamma_{\text{H}^+}\gamma_{\text{C}_2\text{HO}_4^-} = \gamma_{\text{H}^+}\gamma_{\text{NO}_3^-}$, and used the ISORROPIA-predicted $\gamma_{\text{H}^+}\gamma_{\text{NO}_3^-} = \sqrt{\gamma_{\text{H}^+}\gamma_{\text{NO}_3^-}} = 0.265$. In panel (a), we used the average temperature and W_i ($25.7 \pm 3.8 \text{ }^\circ\text{C}$ and $1.1 \pm 1.1 \mu\text{g m}^{-3}$) for the data between 08:00 to 19:59 to calculate the S curve (black line). In panel (b), we used the average temperature and W_i ($21.3 \pm 2.8 \text{ }^\circ\text{C}$ and $2.1 \pm 2.0 \mu\text{g m}^{-3}$) for the data between 20:00 to 07:59 to calculate the S curve (black line). Grey lines in both panels are S curves calculated using one standard deviation from the average temperature and W_i for the two datasets. In panel (a), the dotted grey line is the S curve calculated using $29.5 \text{ }^\circ\text{C}$

and $0.5 \mu\text{g m}^{-3}$ while the solid grey line is the S curve calculated using 21.9°C and $2.2 \mu\text{g m}^{-3}$. In panel (b), the dotted grey line is the S curve calculated using 24.1°C and $0.5 \mu\text{g m}^{-3}$ while the solid grey line is the S curve calculated using 18.5°C and $4.1 \mu\text{g m}^{-3}$.

Characterization of Aerosol Composition, Aerosol Acidity and Organic Acid Partitioning at an Agriculture-Intensive Rural Southeastern U.S. Site

Theodora Nah,^{1,✉} Hongyu Guo,¹ Amy P. Sullivan,² Yunle Chen,¹ David J. Tanner,¹ Athanasios Nenes,^{1,3,4,5} Armistead Russell,⁶ Nga Lee Ng,^{1,3} L. Gregory Huey¹ and Rodney J. Weber^{1,*}

¹*School of Earth and Atmospheric Sciences, Georgia Institute of Technology, Atlanta, GA, USA*

²*Department of Atmospheric Science, Colorado State University, Fort Collins, CO, USA*

³*School of Chemical and Biomolecular Engineering, Georgia Institute of Technology, Atlanta, GA, USA*

⁴*ICE-HT, Foundation for Research and Technology, Hellas, 26504 Patras, Greece*

⁵*IERSD, National Observatory of Athens, P. Penteli, 15236, Athens, Greece*

⁶*School of Civil and Environmental Engineering, Georgia Institute of Technology, Atlanta, GA, USA*

[✉]*Now at School of Energy and Environment, City University of Hong Kong, Kowloon, Hong Kong, China*

* To whom correspondence should be addressed: rweber@eas.gatech.edu

Abstract

The implementation of stringent emission regulations has resulted in the decline of anthropogenic pollutants including sulfur dioxide (SO₂), nitrogen oxides (NO_x) and carbon monoxide (CO). In contrast, ammonia (NH₃) emissions are largely unregulated, with emissions projected to increase in the future. We present real-time aerosol and gas measurements from a field study conducted in an agricultural-intensive region in the southeastern U.S. during the fall of 2016 to investigate how NH₃ affects particle acidity and secondary organic aerosol (SOA) formation via the gas-particle partitioning of semi-volatile organic acids. Particle water and pH were determined using the ISORROPIA-II thermodynamic model and validated by comparing predicted inorganic HNO₃-NO₃⁻ and NH₃-NH₄⁺ gas-particle partitioning ratios with measured values. Our results showed that despite the high NH₃ concentrations (average 8.1 ± 5.2 ppb), PM₁ were highly acidic with pH values ranging from 0.9 to 3.8, and an average pH of 2.2 ± 0.6. PM₁ pH varied by approximately 1.4 units diurnally. Formic and acetic acids were the most abundant gas-phase organic acids, and oxalate was the most abundant particle-phase water-soluble organic acid anion. Measured particle-phase water-soluble organic acids were on average 6 % of the total non-refractory PM₁ organic aerosol mass. The measured molar fraction of oxalic acid in the particle phase (i.e., particle-phase oxalic acid molar concentration divided by the total oxalic acid molar concentration) ranged between 47 and 90 % for PM₁ pH 1.2 to 3.4. The measured oxalic acid gas-particle partitioning ratios were in good agreement with their corresponding thermodynamic predictions, calculated based on oxalic acid's physicochemical properties, ambient temperature, particle water and pH. In contrast, gas-particle partitioning of formic and acetic acids were not well predicted for reasons

currently unknown. For this study, higher NH_3 concentrations relative to what has been measured in the region in previous studies had minor effects on PM_{10} organic acids and their influence on the overall organic aerosol and PM_{10} mass concentrations.

1. Introduction

Ammonia (NH_3) is the most abundant basic gas in the troposphere and plays an important role in many atmospheric processes. It is a major neutralizer of atmospheric acidic species, reacting readily with sulfuric acid (H_2SO_4) and nitric acid (HNO_3) to form ammonium sulfate and nitrate salts (e.g., $(\text{NH}_4)_2\text{SO}_4$, and other forms such as NH_4HSO_4 , $(\text{NH}_4)_3\text{H}(\text{SO}_4)_2$, and NH_4NO_3), which are often the main inorganic components of atmospheric aerosols. The formation of particle-phase ammonium sulfate and nitrate salts in the aerosol phase depends on the thermodynamic states of their precursors and the environmental conditions, which can consequently affect aerosol pH. For example, Guo et al. (2017b) showed that for Southeast U.S. summertime conditions, as aerosol pH increases, the relative fractions of SO_4^{2-} and HSO_4^- increases and decreases, respectively. Wet and dry deposition are the principle NH_3 sinks (Dentener and Crutzen, 1994). NH_3 is spatially heterogeneous, with the highest concentrations typically found near emission sources (Seinfeld and Pandis, 2016). The dominant NH_3 sources in rural areas are agricultural in nature, and include the application of fertilizers and volatilization of livestock waste (Reis et al., 2009; Ellis et al., 2013; Van Damme et al., 2014). Biomass burning, either from wildfires or from controlled burning during land-clearing operations, is also a significant source of NH_3 in rural environments. The primary source of NH_3 in urban areas are industrial emissions (e.g., NH_3 synthesis, manufacture of ammonium nitrate and urea, fluid and thermal catalytic cracking processes in petroleum refinery), though vehicular emissions can be a significant NH_3 source in some heavily populated cities (Reis et al., 2009; Lamarque et al., 2010; Yao et al., 2013; Sun et al., 2017). Vehicular NH_3 emissions are thought to be produced primarily from the reaction of nitrogen oxide with hydrogen in the presence of carbon monoxide in three-way catalysts of gasoline light duty vehicles (Barbier-Jr and Duprez, 1994; Whittington et al., 1995; Livingston et al., 2009; Suarez-Bertoa et al., 2014).

In the US, implementation of stringent emission controls on traditional anthropogenic air pollutants, such as sulfur dioxide (SO_2), nitrogen oxides (NO_x) and carbon monoxide (CO), have led to steady decreases in their emissions, and consequently their concentrations (Blanchard et al., 2013b; Xing et al., 2013). In contrast, NH_3 emissions are largely unregulated, and are projected to

increase due to increased agricultural operations to feed a growing world population (Reis et al., 2009; Ellis et al., 2013). Satellite observations showed that gas-phase NH_3 concentrations have increased substantially in US agricultural areas from 2002 to 2014 (Warner et al., 2017). More wildfires from a changing climate, or from controlled burning for land clearing for agricultural use, may also lead to increased NH_3 emissions (Reis et al., 2009; Pechony and Shindell, 2010; Warner et al., 2016). These trends suggest that NH_3 could play an increasingly important role in atmospheric chemistry.

Previous laboratory studies have shown that NH_3 can influence secondary organic aerosol (SOA) formation and processing. For example, NH_3 increases SOA mass yields in the α -pinene ozonolysis system, and is hypothesized to be due to the formation of ammonium salts from the reaction of NH_3 with organic acids (Na et al., 2007). The heterogeneous uptake of NH_3 by SOA can also lead to the formation of particulate organonitrogen compounds, a class of brown carbon species that can reduce visibility and impact climate (Laskin et al., 2010; Updyke et al., 2012; Lee et al., 2013; Laskin et al., 2015).

The southeastern U.S. is a natural outdoor laboratory for studying the effects of biogenic-anthropogenic interactions on atmospheric aerosol formation and processing. Subtropical vegetation composed mainly of mixed conifer and deciduous forests emit large quantities of biogenic volatile organic compounds (BVOCs) that can act as precursors for SOA formation (Blanchard et al., 2011; Guenther et al., 2012; Blanchard et al., 2013a). Large urban centers and small towns are surrounded by large expanses of forests and widespread rural areas with agricultural activities. Scattered within the southeastern U.S. are also coal-burning power plants and industrial facilities. Anthropogenic activities in this region emit large concentrations of VOCs, SO_2 , NO_x , CO, NH_3 and aerosols (Blanchard et al., 2013c). Similar to other parts of the U.S., SO_2 , CO and NO_x concentrations have decreased steadily in the southeastern U.S. due to the implementation of emission controls (Blanchard et al., 2013b). In contrast, gas-phase NH_3 concentrations have increased in the southeastern U.S. over the same time period (Saylor et al., 2015). These factors make the southeastern U.S. an intriguing place to study the influence of NH_3 on atmospheric aerosol chemistry.

We performed aerosol and gas measurements during a field study conducted in Yorkville, Georgia, U.S., in the fall of 2016, with the goal of understanding how NH_3 affects aerosol acidity

97 and SOA formation. The field site is surrounded by forest and agricultural land, affording an
98 opportunity to make ambient observations in an area impacted by local emissions of BVOCs and
99 NH_3 . In this paper, we present gas and aerosol composition measurements that includes a suite of
100 organic acids. The thermodynamic equilibrium model, ISORROPIA-II, is used to calculate particle
101 water and pH based on measured inorganic aerosol and gas composition (Nenes et al., 1998;
102 Fountoukis and Nenes, 2007), and these predictions are compared to observed gas-particle
103 partitioning of NH_3 , HNO_3 and organic acids. Together, these measurements are used to determine
104 how aerosol acidity affects the mass concentration of particle-phase organic acids at this site.

105 **2. Methods**

106 **2.1. Field site**

107 Aerosol and gas measurements were conducted at the Yorkville, Georgia (33.929 N,
108 85.046 W) SouthEastern Aerosol Research and Characterization (SEARCH) field site from mid-
109 August to mid-October 2016. This is one of the sampling sites for the Southeastern Center for Air
110 Pollution and Epidemiology (SCAPE) study where aerosol characterization measurements were
111 conducted in the summer and winter of 2012 (Xu et al., 2015a; Xu et al., 2015b). A detailed
112 description of the field site can be found in Hansen et al. (2003). This rural site is situated in a
113 mixed forest-agriculture area approximately 55 km northwest and generally upwind of Atlanta.
114 The immediate surrounding area is used for cattle grazing and poultry concentrated animal feeding
115 operations (CAFOs) (Fig. S1). There are no major roads near the field site and nearby traffic
116 emissions were negligible. A large coal-fired power plant (Plant Bowen) is situated approximately
117 25 km north of the site. Hence, the field site is impacted mainly by BVOC and NH_3 emissions,
118 with occasional spikes in SO_2 and minimal influence from urban anthropogenic pollutants such as
119 HNO_3 , O_3 , NO_x and CO (Fig. S2). The sampling period was characterized by moderate
120 temperatures (24.0 °C average, 32.6 °C max, 9.5 °C min) and high relative humidities (68.9 % RH
121 average, 100 % RH max, 21.6 % RH min). Meteorological data are shown in Fig. S3. Data reported
122 are displayed in eastern daylight time (EDT).

123 **2.2. Instrumentation**

124 Instruments were housed in a temperature controlled (~20 °C) trailer during the field study.
125 Gas-phase HNO_3 , SO_2 and organic acids (formic, acetic, oxalic, butyric, glycolic, propionic,

126 valeric, malonic and succinic acids) were measured by a custom-built chemical ionization mass
127 spectrometer (CIMS) using sulfur hexafluoride ions (SF_6^-) as reagent ions. SO_2 and HNO_3 were
128 detected as fluoride adducts (F_2SO_2^- and $\text{NO}_3 \cdot \text{HF}$, respectively) while the organic acids (HX) were
129 detected primarily as conjugated anions (X^-) by the quadrupole mass spectrometer (Huey et al.,
130 1995; Huey et al., 2004; Nah et al., 2018). This CIMS is referred hereafter as the SF_6 -CIMS. Gas-
131 phase NH_3 was measured by an additional custom-built CIMS using protonated ethanol clusters
132 ($(\text{C}_2\text{H}_5\text{OH})_n^+$) as reagent ions. NH_3 was detected primarily as NH_4^+ ions by the quadrupole mass
133 spectrometer (Nowak et al., 2002; Yu and Lee, 2012; You et al., 2014a). This CIMS is referred
134 hereafter as the NH_3 -CIMS.

135 Since HNO_3 , NH_3 and organic acids may condense on surfaces, both SF_6 -CIMS and NH_3 -
136 CIMS used inlet configurations that minimized wall interactions (Huey et al., 2004; Nowak et al.,
137 2006). Each CIMS was connected to an inlet (a 7.6 cm ID aluminum pipe) that protruded beyond
138 the trailer's wall by ~40 cm into the ambient air. Both inlets were ~2 m above the ground. A donut-
139 shaped ring was attached to the ambient sampling port of each pipe to curtail the influence of
140 crosswinds on the pipe's flow dynamics. Both rings were wrapped with a fine wire mesh to prevent
141 ingestion of insects. A flow of ~2800 L min^{-1} was maintained in each pipe using regenerative
142 blowers (AMETEK Windjammer 116637-03). Part of this flow (7 L min^{-1} for the SF_6 -CIMS and
143 4.6 L min^{-1} for the NH_3 -CIMS) was sampled through a custom-made three-way PFA Teflon valve,
144 which connected the pipe's center to the CIMS sampling orifice and could be switched
145 automatically between ambient and background measurements.

146 Background measurements were performed every 25 min for 4 min for both the SF_6 -CIMS
147 and NH_3 -CIMS. During each background measurement, the sampled air flow was passed through
148 an activated charcoal scrubber (Sigma Aldrich) that removed SO_2 , HNO_3 and organic acids prior
149 to delivery into the SF_6 -CIMS, and through a silicon phosphate scrubber (Perma Pure Inc.) that
150 removed NH_3 prior to delivery into the NH_3 -CIMS. > 99 % of the targeted species were removed
151 during background measurements for both the SF_6 -CIMS and NH_3 -CIMS. Standard addition
152 calibrations were performed every 5 h for the SF_6 -CIMS using the outputs of a 1.12 ppm $^{34}\text{SO}_2$
153 gas cylinder (Scott-Marrin Inc.) and a formic or acetic acid permeation device (VICI Metronics).
154 Calibrations for the other gases measured by the SF_6 -CIMS were performed in post-field
155 laboratory work, details of which can be found in Nah et al. (2018) and SI section S1. Standard

156 addition calibrations were performed hourly for the NH₃-CIMS using the output of a NH₃
157 permeation device (KIN-TEK). The outputs of the formic and acetic acid permeation devices were
158 measured periodically by scrubbing the output of the permeation tube in deionized water, followed
159 by ion chromatography analysis for formate and acetate. The emission rate of the NH₃ permeation
160 device was measured using UV optical absorption (Neuman et al., 2003).

161 The detection limits for species measured by the SF₆-CIMS and NH₃-CIMS were
162 approximated from 3 times the standard deviation values (3σ) of the ion signals measured during
163 background mode. The detection limits for HNO₃, SO₂ and the various organic acids measured by
164 the SF₆-CIMS ranged from 1 to 60 ppt for 2.5 min integration periods, which corresponded to the
165 length of a background measurement with a ~4 % duty cycle for each m/z (Table S1). Measurement
166 uncertainties for the concentrations of HNO₃, SO₂ and the various organic acids originate mainly
167 from calibration measurements, and were between 12 and 25 % (Table S1). The detection limit for
168 NH₃ measured by the NH₃-CIMS was 1 ppb for 2.3 min integration periods, which corresponded
169 to the length of a background measurement with a ~29 % duty cycle for the NH₄⁺ ion.
170 Measurement uncertainties for NH₃ concentrations were 13 %.

171 A high-resolution time-of-flight aerosol mass spectrometer (HR-ToF-AMS, Aerodyne
172 Research Inc.) was used to measure the elemental composition of ambient non-refractory PM₁
173 (particles with aerodynamic diameters < 1 μ m). Ambient air was sampled at 16.7 L min⁻¹ through
174 a URG PM₁ cyclone and then through a nafion dryer prior to delivery into the HR-ToF-AMS.
175 Aerosols were dried to RH < 20 % to eliminate the influence of RH on the HR-ToF-AMS's particle
176 collection efficiency. A detailed description of the HR-ToF-AMS can be found in the literature
177 (DeCarlo et al., 2006; Canagaratna et al., 2007; Canagaratna et al., 2015). Briefly, the aerodynamic
178 lens of the HR-ToF-AMS focused the dried submicron aerosols into a narrow beam. The aerosols
179 were then impacted onto a heated tungsten surface (~600 °C) where they were flash vaporized.
180 The resulting vapors were ionized by electron impact ionization (70 eV), and the ions were
181 detected by a time-of-flight mass spectrometer. Gas-phase interferences were accounted for by
182 subtracting the signals obtained during daily measurements of filtered, particle-free sampling air.
183 Ionization efficiency calibrations were performed weekly using 300 nm ammonium nitrate and
184 ammonium sulfate particles. Composition-dependent collection efficiency (CDCE) values of 0.44
185 to 0.55 were determined using the procedure detailed by Middlebrook et al. (2012), where CDCE

186 values are derived based largely on aerosol inorganic species concentrations and the relative
187 humidity in the sampling line. In addition, a constant collection efficiency (CE) value of 0.9 was
188 determined from the comparison of raw HR-ToF-AMS SO_4^{2-} data with other particulate SO_4^{2-}
189 measurements performed during the study. Comparisons of aerosol mass concentrations obtained
190 from the application of CDCE values (i.e., 0.44 to 0.55) vs. a constant CE value (i.e., 0.9) to the
191 raw HR-ToF-AMS data are discussed in section 3.2. Uncertainties in HR-ToF-AMS measurements
192 were estimated to be approximately 25 % (Canagaratna et al., 2007).

193 Particle-phase water-soluble organic acids, inorganic cations and anions were measured
194 using two Particle-into-Liquid Sampler (PILS) systems coupled to ion chromatographs (ICs)
195 (Orsini et al., 2003). Each PILS sampled ambient air at nominally 16.7 L min^{-1} through a URG
196 PM_{10} cyclone. Before PILS1, which was used to measure water-soluble inorganic cation and
197 anions, two long (24 cm) URG glass annular denuders coated with sodium carbonate and
198 phosphorous acid were used to remove acidic and basic gases. Before PILS2, which measured
199 water-soluble organic acids, a 28 cm parallel plate carbon denuder (Sunset Lab) was used to
200 remove organic gases (Eatough et al., 1993). In each PILS, aerosols were mixed with water vapor
201 at $\sim 100^\circ\text{C}$ generated from heated ultrapure deionized water (Weber et al., 2001; Orsini et al.,
202 2003). The resulting droplets were impacted onto a plate, with the resulting liquid sample analyzed
203 by ICs. Each IC system was calibrated at the beginning and end of the study using five multi-
204 compound standards in order to create calibration curves. Periodically, a HEPA filter (Pall Life
205 Sciences) was placed on the inlet to determine the background in near real-time. The measurement
206 uncertainty for each IC system was about 10 %.

207 PILS1 was connected to two Dionex ICS-1500 ICs (Thermo Fisher Scientific) to measure
208 the water-soluble inorganic ions. These two IC systems include an isocratic pump, self-
209 regenerating anion or cation suppressor, and conductivity detector. This system will be referred
210 hereafter as the PILS-IC. Anions were separated using a Dionex IonPac AS15 guard and analytical
211 column (4 x 250 mm, Thermo Fisher Scientific) employing an eluent of 38 mM sodium hydroxide
212 at a flow rate of 1.5 mL min^{-1} . Cations were separated using a Dionex IonPac CS12A guard and
213 analytical column (4 x 250 mm, Thermo Fisher Scientific) employing an eluent of 18 mM
214 methanesulfonic acid at a flow rate of 1 mL min^{-1} . A new chromatogram was obtained every 30

215 min with a sample loop fill time (i.e., ambient sample integration time) of 20 min. The limit of
216 detection for the various anions and cations was approximately $0.01 \mu\text{g m}^{-3}$.

217 PILS2 was coupled to a Dionex ICS-4000 capillary high-pressure ion chromatography
218 (HPIC) system to measure the water-soluble organic acids. The HPIC includes an eluent generator,
219 isocratic pump, degasser, suppressor, carbonate removal device, and conductivity detector. This
220 system will be referred hereafter as the PILS-HPIC. The organic acids were separated using a
221 Dionex AS11-HC- $4\mu\text{m}$ capillary guard and analytical column ($0.4 \times 250\text{mm}$, Thermo Fisher
222 Scientific), which used a potassium hydroxide gradient separation method at a flow rate of 0.015
223 mL min^{-1} . A new chromatogram was obtained every 60 min with a sample loop fill time of 2 min.
224 The limit of detection for the various organic acids was approximately $0.001 \mu\text{g m}^{-3}$.

225 Particle- and gas-phase water-soluble organic carbon (WSOC_p and WSOC_g , respectively)
226 were measured using two Sievers 900 series total organic carbon (TOC) analyzers (GE Analytical
227 Instruments), as described by Sullivan et al. (2004). For WSOC_p measurements, ambient air was
228 sampled at 15.2 L min^{-1} through a URG PM_{10} cyclone and a parallel plate carbon denuder into a
229 PILS coupled to the first TOC analyzer. For WSOC_g measurements, ambient air was sampled at
230 20 L min^{-1} through a Teflon filter (45 mm diameter, $2.0 \mu\text{m}$ pore size, Pall Life Sciences) to remove
231 particles in the air stream. This filter was changed every 3 to 4 days. The particle-free air was then
232 directed to a MIST chamber filled with ultrapure deionized water, which scrubbed the soluble
233 gases at an air flow rate of 20 L min^{-1} . Soluble gases with Henry's law constants greater than 10^3
234 $\text{mole L}^{-1} \text{ atm}^{-1}$ were scrubbed into deionized water in the MIST chamber (Spaulding et al., 2002).
235 The resulting MIST chamber liquid sample was analyzed by the second TOC analyzer. The TOC
236 analyzers converted the organic carbon in the liquid samples to carbon dioxide using UV radiation
237 and chemical oxidation. The carbon dioxide formed was then measured by conductivity. The
238 amount of organic carbon in the liquid samples is proportional to the measured increase in
239 conductivity of the dissolved carbon dioxide. Each WSOC_p and WSOC_g measurement lasted 4
240 min. Background WSOC_p and WSOC_g measurements were performed for 45 min every 12 h by
241 stopping the sample air flow and rinsing the system with deionized water. Both TOC analyzers
242 were calibrated at the beginning and end of the study using varying concentrations of sucrose
243 solutions to create calibration curves (as specified by the instrument manual). The limit of
244 detections for WSOC_p and WSOC_g were 0.2 and $0.4 \mu\text{gC m}^{-3}$, respectively. The measurement

uncertainties for WSOC_p and WSOC_g were estimated to be 10 % based on uncertainties in the TOC analyzer, sample air and liquid flows.

A suite of instruments operated by the SEARCH network provided supporting gas and aerosol measurements (Hansen et al., 2003; Edgerton et al., 2005, 2006). O₃ was measured by a UV absorption instrument (Thermo Fisher Scientific) with a temporal resolution of 1 min. NO and NO_x were measured by a chemiluminescence instrument (Thermo Fisher Scientific) with a temporal resolution of 1 min. NO₂ was obtained from the difference between NO and NO_x. CO was measured by a non-dispersive infrared absorption instrument (Thermo Fisher Scientific) with a temporal resolution of 1 min. NH₃ was measured by a denuder-based instrument (ARA) with a temporal resolution of 5 min. Comparisons of measurements by the NH₃-CIMS and denuder-based instrument will be presented in section 3.1. A filter-based particle composition monitor (ARA) provided 24 h-integrated PM_{2.5} measurements of particle mass and major inorganic ions measured offline by ion chromatography. Organic carbon (OC) and elemental carbon (EC) in PM_{2.5} were measured by a OCEC Analyzer (Sunset Labs) with a temporal resolution of 1 h. This analyzer determined OC by thermal optical transmittance. VOCs were measured by a gas chromatography-flame ionization detector (GC-FID, Agilent Technologies) with a temporal resolution of 1h.

2.2. Particle pH and water calculation

The thermodynamic equilibrium model ISORROPIA-II was used to determine the phase state and composition of an NH₄⁺-SO₄²⁻-NO₃⁻-Cl⁻-Na⁺-Ca²⁺-K⁺-Mg²⁺-water inorganic aerosol in equilibrium with its corresponding gas-phase species (Fountoukis and Nenes, 2007; Nenes et al., 1998). This approach was used in previous studies to determine particle water and pH in different parts of the world (Guo et al., 2015; Bougiatioti et al., 2016; Guo et al., 2016; Weber et al., 2016; Guo et al., 2017a; Guo et al., 2017c; Shi et al., 2017). The pH of an aqueous solution is defined as the negative logarithm of the hydronium ion (H₃O⁺) activity on a molality basis (www.goldbook.iupac.org/html/P/P04524.html, last access: 6 July 2018):

$$pH = -\log_{10}[a(H^+)] = -\log_{10}\left[m(H^+)\gamma_m(H^+)/m^\theta\right] \quad (1a)$$

where $a(H^+)$ is the hydronium ion activity in an aqueous solution, $m(H^+)$ is the hydronium ion molality, $\gamma_m(H^+)$ is the molality-based hydronium ion activity coefficient, and m^θ is the standard molality (1 mol kg⁻¹). For simplicity, H₃O⁺ is denoted here as H⁺ even though we recognize that

the unhydrated hydrogen ion is rare in aqueous solutions. Since most thermodynamic equilibrium models (e.g., ISORROPIA-II, E-AIM) **do not report liquid concentrations, but instead** report species in terms of concentration per volume of air (e.g., $\mu\text{g m}^{-3}$, $\mu\text{mol m}^{-3}$), **we have calculated** the particle pH **by**:

$$\text{pH} = -\log_{10} \gamma_{H^+} H_{aq}^+ = -\log_{10} \frac{1000 \gamma_{H^+} H_{air}^+}{W_i + W_o} \cong -\log_{10} \frac{1000 \gamma_{H^+} H_{air}^+}{W_i} \quad (1b)$$

where γ_{H^+} is the hydronium ion activity coefficient (assumed to be 1), H_{aq}^+ is the concentration of hydronium ions in particle water **in mole L⁻¹** (i.e., **the density of water is assumed to be 1000 kg m⁻³, and so** pH is calculated in terms of molarity), H_{air}^+ ($\mu\text{g m}^{-3}$) is the hydronium ion concentration per volume of air, and W_i and W_o ($\mu\text{g m}^{-3}$) are the bulk particle water concentrations associated with inorganic and organic species per volume of air, respectively. In equation 1b, the molecular weight of H^+ is taken as 1 g mole⁻¹, and 1000 is the factor needed for unit conversion of g L⁻¹ to $\mu\text{g m}^{-3}$. H_{air}^+ and W_i are outputs of the ISORROPIA-II model. Previous studies have shown that particle pH values predicted using only W_i are reasonably accurate since the sensitivity of particle pH to the effects of W_o is small (Guo et al., 2015). For the southeastern U.S., Guo et al. (2015) reported that particle pH values predicted using only W_i were systematically 0.15 to 0.23 units lower than those predicted using $W_i + W_o$ during the 2013 Southern Oxidant Aerosol Study (SOAS) and SCAPE campaigns. Given this small deviation and that organic aerosol hygroscopicity was not measured in this field study, we report particle pH only considering W_i .

ISORROPIA-II was run in “forward” mode, which assumes that aerosols are “metastable” with no solid precipitates, to predict particle pH and the partitioning of semi-volatile compounds. In “forward” mode, the model calculates the gas-particle equilibrium partitioning concentrations based on the input of the total concentration of a species (i.e., gas + particle). In “reverse” mode, the model calculates the gas-particle equilibrium partitioning concentrations based on the input of only the particle-phase concentration of a species. We used “forward” mode because the “reverse” mode is sensitive to measurement errors, which often result in large model biases in the predicted particle pH (Hennigan et al., 2015). The measured particle-phase inorganic NH_4^+ , SO_4^{2-} and NO_3^- concentrations and gas-phase HNO_3 and NH_3 concentrations were used as model inputs. The “metastable” assumption is reasonable since the high RH (average RH 68.9 %) observed during the study indicated that the aerosols had likely deliquesced. We excluded data for periods where

Deleted: can be calculated as

Deleted: molarity-based

Deleted: (mole L⁻¹)

Deleted: molar

305 the RH was above 95 % since the exponential growth in particle liquid water with RH introduces
306 large pH uncertainties (Malm and Day, 2001; Guo et al., 2015).

307 In using ISORROPIA-II to predict particle pH and the partitioning of semi-volatile
308 compounds, we also assumed that the aerosols are internally mixed and that the particle pH does
309 not change with particle size (i.e., the overall particle pH is characterized by the particle's bulk
310 properties). As long as some small fraction of sulfate is mixed with various aerosol components,
311 (e.g., non-volatile cations), the assumption that aerosols are completely internally mixed has a
312 small effect on the predicted pH (Guo et al., 2017b). However, the presence of multiple organic
313 and inorganic species in ambient aerosols may lead to multiple phases within the particle (i.e.,
314 phase separation). Consequently, this may result in the unequal distribution of inorganic species
315 among different phases, each with its own water activity and inorganic concentration. Previous
316 studies have shown that liquid-liquid and solid-liquid phase separations may occur for mixed
317 organic and inorganic aerosols at low RH and organic aerosol oxygen-to-carbon atomic ratios
318 (O/C) (Bertram et al., 2011; Song et al., 2012; You et al., 2013; You et al., 2014b; You and
319 Bertram, 2015). Phase separations were always observed at $O/C \leq 0.5$, while no phase separation
320 was observed at $O/C \geq 0.8$. The probability for the occurrence of phase separation decreased at
321 higher RH for $0.5 < O/C < 0.8$. The average O/C for this field study is 0.69 ± 0.06 . Organic acids
322 were not included in the calculation of particle pH. This is reasonable since their total mass
323 concentration was small compared to the total inorganic mass concentration. The average ratio of
324 the organic acid mass concentration to the inorganic mass concentration is 0.25. Furthermore, Song
325 et al. (2018) showed that including organic acid mass concentrations in thermodynamic model
326 calculations had minor effects on particle pH if the system is in equilibrium. The validity of these
327 assumptions and the resulting thermodynamic model predictions will be evaluated by comparing
328 the predicted gas-particle partitioning ratios of semi-volatile inorganic compounds with measured
329 values in section 3.3.

330 **3. Results and Discussion**

331 **3.1. NH₃ observations**

332 Continuous measurements of NH₃ were made using the NH₃-CIMS from 13 September to
333 12 October. Figures 1a and 1b show the time series and average diurnal profile of NH₃,

334 respectively. NH_3 concentrations ranged from 0.7 to 39.0 ppb (0.5 to $28.5 \mu\text{g m}^{-3}$), and exhibited
335 consistent diurnal cycles. NH_3 was generally higher in the late mornings and early afternoons.
336 Concentrations started to increase at 07:30, which coincided with an increase in temperature at
337 sunrise (Fig. S3). Possible reasons for the morning increase include volatilization of particulate
338 ammonium and animal waste, entrainment from the residual layer where NH_3 may not have been
339 depleted, evaporation of dew or fog that contained dissolved NH_3 , and emission from plant stomata
340 (Ellis et al., 2011). NH_3 decreased at 14:30, approximately 1 hour before temperature decreased,
341 and may be due to changes in the boundary layer height. However, this hypothesis cannot be tested
342 since the boundary layer height was not measured during the study. The diurnal plot does not
343 account for dilution as the boundary layer expanded, and only indicates that if emissions were
344 solely from the surface and lower concentrations aloft, these NH_3 sources were of significant
345 magnitude.

346 The average NH_3 concentration measured by the NH_3 -CIMS is 8.1 ± 5.2 ppb. This is
347 approximately 2 times higher than the average NH_3 concentration (3.8 ± 2.9 ppb) measured by the
348 denuder-based instrument operated by the SEARCH network over the same time period (Fig. S4).
349 Differences in NH_3 concentrations measured by the two instruments may be due to positive and
350 negative sampling artifacts caused by differences in sampling inlets (e.g., inlet length and
351 location), frequency of calibration and background measurements, and (in the case of the denuder-
352 based instrument) possible sample contamination during chemical analysis. Discussions on how
353 differences in measured NH_3 concentrations affect PM_{10} pH predictions will be presented in section
354 3.3. Nevertheless, there is a record of NH_3 concentrations measured by the denuder-based
355 instrument at this site since 2008. Just prior to, and during this study, NH_3 concentrations are
356 generally the highest observed since 2011 (Fig. S5). These elevated NH_3 concentrations may be
357 due to sporadic biomass burning episodes caused by elevated temperatures and widespread
358 drought across the southeastern U.S. in 2016 (Park Williams et al., 2017; Case and Zavodsky,
359 2018).

360 The NH_3 -CIMS measurements are examined with the meteorological data to gain insights
361 on the primary NH_3 sources during the sampling period. To account for wind speed, the 1-hour
362 averaged NH_3 concentrations are first multiplied by their corresponding 1-hour averaged wind
363 speeds. These normalized NH_3 concentrations are then used to construct a wind direction polar

plot showing the average normalized NH_3 concentration per 10 degrees bin (Fig. 1c). The wind direction polar plot shows that the normalized NH_3 is approximately 2 times greater than the average when air masses are transported from the south-east, the general direction of the poultry CAFOs located approximately 2 km from the field site (Fig. S1), which are known for high NH_3 emissions. This conclusion is reaffirmed by NH_3 measurements by the SEARCH network's denuder-based instrument.

NH_3 concentrations measured by the two instruments in this study are substantially higher than those measured in three recent field studies conducted in the continental U.S.: 2010 California Nexus (CalNex) study, 2013 Southeast Nexus (SENEX) study and 2013 SOAS study (see Table 1). The differences in NH_3 may be attributed to differences in land use, proximity to CAFOs and meteorological conditions. The high NH_3 concentrations in this study allow us to make ambient observations of the effect of NH_3 on particle acidity and the gas-particle partitioning of semi-volatile inorganic and organic compounds, and compare them with previous studies.

3.2. PM_{10} composition

The aerosol inorganic chemical composition was measured by several instruments during this study. The HR-ToF-AMS, PILS-IC and PILS-HPIC measured the composition of PM_{10} , while a filter-based particle composition monitor measured the composition of $\text{PM}_{2.5}$. Comparisons of aerosol SO_4^{2-} , NO_3^- and NH_4^+ mass concentrations obtained from the application of CDCE values to the raw HR-ToF-AMS data are compared to those measured by the other three instruments in Fig. S6. NH_4^+ measurements by the PILS-IC are not available for comparison due to denuder breakthrough that occurred during the study.

SO_4^{2-} measurements by the various instruments are generally well correlated with each other, with R^2 values ranging from 0.64 to 0.92. Although PM_{10} SO_4^{2-} measurements by the two PILS systems show good agreement with each other, HR-ToF-AMS CDCE-applied SO_4^{2-} measurements are approximately two times higher than the PILS and filter measurements. Similar systematic differences are also observed for NO_3^- and NH_4^+ measurements. NO_3^- and NH_4^+ measurements by the four instruments are moderately correlated ($R^2 = 0.54$ to 0.79 and $R^2 = 0.94$, respectively). NO_3^- measurements by the PILS and filter systems are mostly similar; however, HR-ToF-AMS CDCE-applied PM_{10} NO_3^- and NH_4^+ measurements are approximately three times and

393 two times higher than the PILS and filter measurements. One possible reason is that the calculated
 394 CDCE is lower due to organics dominating the aerosol composition during the study (average of
 395 74.2 ± 7.9 % of the non-refractory PM₁ mass concentration). Lee et al. (2015) suggested that a
 396 high organic mass fraction may impede the complete efflorescence of aerosols when they are
 397 passed through the drier prior to delivery into the HR-ToF-AMS, thus reducing the particle bounce
 398 and increasing the CE value. Hence, we estimated HR-ToF-AMS PM₁ mass concentrations that
 399 would be consistent with PILS and filter measurements by multiplying all the raw HR-ToF-AMS
 400 data by a constant CE value of 0.9, which was obtained from comparisons of the raw HR-ToF-
 401 AMS SO₄²⁻ data with PILS-IC and PILS-HPIC SO₄²⁻ measurements. The constant CE-applied HR-
 402 ToF-AMS data is used in all our subsequent analyses.

403 Figure 2 shows the time series and average diurnal profiles of non-refractory PM₁ species.
 404 The average non-refractory PM₁ organics, SO₄²⁻, NO₃⁻ and NH₄⁺ mass concentrations are $5.0 \pm$
 405 2.3 , 1.6 ± 0.4 , 0.2 ± 0.1 and 0.4 ± 0.2 $\mu\text{g m}^{-3}$, respectively. Organics are the dominant non-
 406 refractory PM₁ species, accounting for 74.2 ± 7.9 % of the non-refractory PM₁ mass concentration
 407 during the field study. Organic aerosol mass concentration was slightly higher at night, which is
 408 likely caused by changes in the boundary layer height, emission sources and SOA formation
 409 processes (Xu et al., 2015b). Previous studies have shown that nighttime SOA production in the
 410 Southeastern U.S. is largely attributed to nitrate radical oxidation and ozonolysis of monoterpenes,
 411 which are abundant at night (Pye et al., 2015; Xu et al., 2015a; Xu et al., 2015b; Lee et al., 2016;
 412 Zhang et al., 2018). Specifically, the nitrate radical oxidation of some monoterpenes (e.g., β -
 413 pinene) could form low volatility organic nitrates that are condensable and could contribute
 414 substantially to the nocturnal organic aerosol mass (Boyd et al., 2015; Boyd et al., 2017; Ng et al.,
 415 2017). Apportionment of organic aerosol sources will be discussed in an upcoming publication.
 416 SO₄²⁻ is the second most abundant non-refractory PM₁ species (16.3 ± 5.7 % mass fraction),
 417 followed by NH₄⁺ (5.9 ± 2 % mass fraction) and NO₃⁻ (3.6 ± 2.2 % mass fraction). SO₄²⁻ mass
 418 concentration peaked in the afternoon due to enhanced SO₂ photooxidation (Weber et al., 2003).
 419 The NO₃⁻ mass concentration measured by the HR-ToF-AMS is the nitrate functional group (-
 420 ONO₂) present on organic and inorganic nitrates. Hence, the diurnal profile of the NO₃⁻ mass
 421 concentration in Fig. 2 has contributions from both organic and inorganic nitrates. The mass
 422 concentrations of organic and inorganic nitrates increased after sunset and peaked at sunrise (Fig.
 423 S7), likely due to the formation of organic nitrates from nighttime NO₃ chemistry and increased

gas-to-particle partitioning of organic and inorganic nitrates as temperature decreased (Xu et al., 2015a; Xu et al., 2015b). Quantification and characterization of organic nitrates based on HR-ToF-AMS and PILS-IC PM₁ NO₃⁻ measurements will be discussed in a future publication. NH₄⁺ mass concentration has moderate diurnal variations with marginally higher concentrations in the afternoon, likely due to the contrasting day/night phases of ammonium sulfate and ammonium nitrate formation. SO₄²⁻, NO₃⁻ and NH₄⁺ molar concentrations indicated that NH₄⁺ is mainly associated with SO₄²⁻ in PM₁.

3.3. PM₁ pH predictions

CIMS HNO₃ and NH₃ data, HR-ToF-AMS PM₁ SO₄²⁻ and NH₄⁺ data, PILS-IC PM₁ NO₃⁻ and non-volatile cation (Cl⁻, Na⁺, Ca²⁺, K⁺ and Mg²⁺) data, measured temperature and RH are used as ISORROPIA-II model inputs to predict PM₁ W_i and pH from 13 September to 6 October. Figure 3 shows the time series and average diurnal profiles of ISORROPIA-predicted PM₁ W_i and pH. PM₁ are highly acidic with pH values ranging from 0.9 to 3.8, and an average pH of 2.2 ± 0.6 . The average PM₁ pH was 2.5 ± 0.6 during periods where the NH₃ concentration was higher than 13.3 ppb (i.e., average NH₃ concentration + 1 standard deviation = $8.1 + 5.2 = 13.3$ ppb). The PM₁ pH values in this study are generally similar to those reported by Guo et al. (2015) at the same field site during winter 2012. Our observation that PM₁ are acidic despite the high NH₃ concentrations in this study is consistent with previous studies showing that particle pH has weak sensitivities to wide NH₃ and SO₄²⁻ mass concentration ranges due to pH buffering caused by the partitioning of NH₃ between the gas and particle phases (Weber et al., 2016; Guo et al., 2017c). This weak particle pH sensitivity also explains the small changes in PM₁ pH values (about 10 % lower, Fig. S8) when NH₃ measurements by the SEARCH network denuder-based instrument are used in ISORROPIA-II calculations (instead of NH₃-CIMS measurements).

PM₁ pH varied by approximately 1.4 units throughout the day. W_i has an average value of $1.6 \pm 1.7 \mu\text{g m}^{-3}$. PM₁ W_i and pH showed similar diurnal profiles, with both peaking in the mid-morning and reaching their minima in the mid-afternoon. These diurnal trends are consistent with those previously reported by Guo et al. (2015) for PM₁ measured during the summer and winter in different parts of the southeastern U.S. Also shown in Fig. 3b is the diurnal profile of H_{air}^+ , which peaked in the mid-afternoon. The W_i and H_{air}^+ maximum/minimum ratios are comparable (6.5 and

453 5.3, respectively), thus indicating that the diurnal variation in particle pH is driven by both W_i and
454 H_{air}^+ .

455 The average PM₁ pH for this study is about 1 unit higher than those for the SENEX and
456 SOAS campaigns (Table 1), and is likely due to the much higher abundance of NH₃ in this study.
457 The average NH₃ mass concentration in this study is approximately 49 times and 15 times higher
458 than those in the SENEX and SOAS campaigns, respectively. The average PM₁ pH for this study
459 is similar to that for the CalNex campaign even though the average NH₃ mass concentration in this
460 study is only approximately 4 times higher than that in the CalNex campaign (Guo et al., 2017a).
461 This may be due, in part, to PM₁ SO₄²⁻ and NO₃⁻ mass concentrations at CalNex being
462 approximately 2 times and 18 times larger than those of this study, respectively. Aerosol inorganic
463 SO₄²⁻ and NO₃⁻ species are hygroscopic species. The much higher NO₃⁻ mass concentrations in the
464 CalNex campaign (due, in part, to high NO_x emissions) increased particle W_i substantially, which
465 diluted H⁺ and raised particle pH, resulting in more gas-to-particle partitioning of NO₃⁻, and
466 eventually leading to pH levels similar to those observed in this study. This type of feedback does
467 not happen in the southeastern U.S. where non-volatile SO₄²⁻ dominates the uptake of particle
468 water. It is also possible that the higher RH and lower temperatures during the CalNex campaign
469 (relative to this study) contributed to high particle W_i , which diluted H⁺ and raised particle pH
470 levels similar to those observed in this study.

471 The validity of this study's thermodynamic model predictions is evaluated by comparing
472 the predicted gas-particle partitioning ratios of semi-volatile inorganic compounds (i.e., NO₃⁻ and
473 NH₄⁺) with measured values (Fig. S9). CIMS HNO₃ and NH₃ data, PILS-IC NO₃⁻ and HR-ToF-
474 AMS NH₄⁺ data are used in this comparison. $\epsilon(\text{NO}_3^-)$ and $\epsilon(\text{NH}_4^+)$ are defined as the particle-phase
475 molar concentration divided by the total molar concentration (gas + particle), i.e., $\epsilon(\text{NO}_3^-) = \text{NO}_3^-$
476 / (HNO₃ + NO₃⁻) and $\epsilon(\text{NH}_4^+) = \text{NH}_4^+ / (\text{NH}_3 + \text{NH}_4^+)$. Predicted NH₃, NH₄⁺ and $\epsilon(\text{NH}_4^+)$ values
477 are generally within 10 % of and are highly correlated ($R^2 = 0.96$ to 0.99) with measured values
478 (Fig. S9). While predicted HNO₃ values generally agreed with measurements, substantial scatter
479 can be seen between the predicted and measured values for NO₃⁻ and $\epsilon(\text{NO}_3^-)$. This scatter can be
480 attributed, at least in part, to uncertainties brought about by the low PM₁ NO₃⁻ mass concentrations
481 and effects of coarse mode cations (e.g., Na⁺, Ca²⁺, K⁺ and Mg²⁺) on fine mode HNO₃-NO₃⁻ gas-
482 particle equilibrium (i.e., HNO₃ can partition to both fine and coarse modes, thereby affecting fine

mode NO_3^- concentrations; no such effect occurs for $\text{NH}_3\text{-NH}_4^+$ gas-particle equilibrium). In general, the overall good agreement between model predictions and measurements indicated that our assumptions that aerosols are metastable (i.e., aerosols are supersaturated aqueous droplets) with no phase separation for the thermodynamic calculations are reasonable for the conditions of this study, and do not affect model predictions.

The molar fractions of NO_3^- and NH_4^+ in the particle phase (i.e., $\varepsilon(\text{NO}_3^-)$ and $\varepsilon(\text{NH}_4^+)$) measured in this study are compared with those measured during the CalNex, SENEX and SOAS campaigns. Figure 4 shows the measured $\varepsilon(\text{NO}_3^-)$ and $\varepsilon(\text{NH}_4^+)$ values as a function of their ISORROPIA-predicted particle pH for the various field studies. For each field study, only a subset of the data is chosen for this comparison ($1 \leq W_i \leq 4 \mu\text{g m}^{-3}$ and $15 \text{ }^\circ\text{C} \leq \text{temperature} \leq 25 \text{ }^\circ\text{C}$) to reduce the effects of variability of W_i and temperature on gas-particle partitioning for comparison with the calculated S (or sigmoidal) curves, which are calculated based on $W_i = 2.5 \mu\text{g m}^{-3}$ and temperature = $20 \text{ }^\circ\text{C}$. The S curves for $\text{HNO}_3\text{-NO}_3^-$ and $\text{NH}_3\text{-NH}_4^+$ partitioning as a function of particle pH are also plotted as solid lines. The S curves are calculated based on the solubility and dissociation of NO_3^- and NH_4^+ species in water:

$$\varepsilon(\text{NO}_3^-) = \frac{H_{\text{HNO}_3}^* RT W_i \times 0.987 \times 10^{-14}}{\gamma_{\text{H}^+} \gamma_{\text{NO}_3^-} 10^{-\text{pH}} + H_{\text{HNO}_3}^* RT W_i \times 0.987 \times 10^{-14}} \quad (2)$$

$$\varepsilon(\text{NH}_4^+) = \frac{\frac{\gamma_{\text{H}^+} 10^{-\text{pH}}}{\gamma_{\text{NH}_4^+}} H_{\text{NH}_3}^* RT W_i \times 0.987 \times 10^{-14}}{1 + \frac{\gamma_{\text{H}^+} 10^{-\text{pH}}}{\gamma_{\text{NH}_4^+}} H_{\text{NH}_3}^* RT W_i \times 0.987 \times 10^{-14}} \quad (3)$$

where $H_{\text{HNO}_3}^*$ and $H_{\text{NH}_3}^*$ ($\text{mole}^2 \text{ kg}^{-2} \text{ atm}^{-1}$) are equilibrium constants and are the products of the Henry's law constant and the dissociation constant of HNO_3 and NH_3 , respectively, R is the gas constant ($8.314 \text{ m}^3 \text{ Pa K}^{-1} \text{ mol}^{-1}$), T is temperature (K), and γ_i 's are activity coefficients. $H_{\text{HNO}_3}^*$ and $H_{\text{NH}_3}^*$ values at $20 \text{ }^\circ\text{C}$ are calculated using equations found in Clegg and Brimblecombe (1990) and Clegg et al. (1998), respectively. Activity coefficients predicted by ISORROPIA-II are $\gamma_{\text{H}^+ - \text{NO}_3^-} = \sqrt{\gamma_{\text{H}^+} \gamma_{\text{NO}_3^-}} = 0.28$, $\gamma_{\text{H}^+} = 1$ and $\gamma_{\text{NH}_4^+} = 1$. Derivations of the analytically calculated S curves for $\varepsilon(\text{NO}_3^-)$ and $\varepsilon(\text{NH}_4^+)$ in equations 2 and 3 can be found in Guo et al. (2017a). As shown in Fig. 4, the measured $\varepsilon(\text{NO}_3^-)$ and $\varepsilon(\text{NH}_4^+)$ values for the four field studies all generally converged on the calculated S curves. The higher particle pH values in this study and the CalNex

campaign relative to those for the SENEX and SOAS campaigns resulted in less NH_3 and more HNO_3 partitioned to the particle phase, as predicted by these simple analytical expressions. A similar analysis will be performed for the organic acids in section 3.5.

3.4. WSOC and water-soluble organic acids

The time series and average diurnal profiles of WSOC_g and WSOC_p are shown in Fig. S10. The average WSOC_g mass concentration ($3.6 \pm 2.7 \mu\text{gC m}^{-3}$) is roughly four times higher than that of WSOC_p ($1.0 \pm 0.6 \mu\text{gC m}^{-3}$). The diurnal profile of WSOC_p is somewhat flat, likely due to various organic aerosol sources having different water solubility and diurnal cycles, and compensating each other throughout the day (Xu et al., 2015b; Xu et al., 2017). In contrast, WSOC_g displayed strong diurnal variations. WSOC_g increased at 07:30, which coincided with the sharp increase in solar irradiance (Fig. S3). WSOC_g decreased at 21:30, approximately 2 hours after sunset. Also shown in Fig. S10 are the time series and average diurnal profile of the mass fraction of total WSOC in the particle phase, i.e., $F_p = \text{WSOC}_p / (\text{WSOC}_p + \text{WSOC}_g)$. The peak F_p coincided with the minima of WSOC_g at 07:30.

The average WSOC_g and WSOC_p ($3.6 \pm 2.7 \mu\text{gC m}^{-3}$ and $1.0 \pm 0.6 \mu\text{gC m}^{-3}$) are slightly lower than those measured during the SOAS campaign (SOAS $\text{WSOC}_g = 4.9 \mu\text{gC m}^{-3}$ and $\text{WSOC}_p = 1.7 \mu\text{gC m}^{-3}$) (Xu et al., 2017). While the diurnal profiles of WSOC_p in both studies are flat, the diurnal profiles of WSOC_g measured in the two studies are different. WSOC_g measured in the SOAS study decreased at sunset, while WSOC_g measured in this study decreased 2 hours after sunset. Differences in WSOC_g diurnal profiles in the two studies are likely due to differences in emission sources as a result of different sampling periods (SOAS was in early summer and this study was in early fall), land use and/or land cover. The ratio of WSOC_p to OC for this study was estimated at 30 %, but this comparison is imprecise because WSOC_p was PM_{10} and OC was $\text{PM}_{2.5}$ (refer to Fig. S11 and SI section S2).

Figure 5 shows the time series of particle- and gas-phase concentrations of formic, acetic, oxalic, malonic, succinic, glutaric and maleic acids. Their diurnal profiles are shown in Fig. 6. Gas-phase measurements of glutaric and maleic acids are not available. Gas-phase measurements of butyric, glycolic, propionic and valeric acids were also measured during the study and have

535 been presented in Nah et al. (2018), but will not be discussed here since their particle-phase
536 measurements are not available.

537 Assuming that all the measured organic acids are completely water-soluble, 30 % of the
538 WSOC_g is comprised of these organic acids (Nah et al., 2018). Formic and acetic acids are the
539 most abundant gas-phase organic acids, with averages of 2.2 ± 1.6 and $1.9 \pm 1.3 \mu\text{g m}^{-3}$,
540 respectively. The average carbon mass fraction of WSOC_g comprised of formic and acetic acids
541 are 7 and 13 %, respectively. All the gas-phase organic acids displayed strong and consistent
542 diurnal cycles, with higher concentrations being measured during warm and sunny days. Their
543 concentrations start to increase at sunrise (at 07:30), building to a peak between 15:30 and 19:30,
544 then decrease overnight.

545 Nah et al. (2018) previously showed that the measured gas-phase organic acids during the
546 study, including oxalic acid, likely have the same or similar sources. Poor correlations between
547 gas-phase organic acid concentrations and those of anthropogenic pollutants (HNO₃, SO₂, CO and
548 O₃) indicated that these organic acids are not due to anthropogenic emissions, and are likely
549 biogenic in nature. Biogenic emissions of gas-phase organic acids and/or their BVOC precursors
550 are elevated at high temperatures, resulting in higher organic acid concentrations during warm and
551 sunny days. For example, isoprene, which is the dominant BVOC in Yorkville, has a somewhat
552 similar diurnal profile as the organic acids. In addition, the concentration of isoprene is moderately
553 correlated with those of formic and acetic acids (Fig. S10 of Nah et al., 2018), which are known
554 products of isoprene photooxidation. Some of these gas-phase organic acids may also be formed
555 in the particle phase during organic aerosol photochemical aging, with subsequent volatilization
556 into the gas phase. The gas-particle partitioning of organic acids likely depends on thermodynamic
557 conditions, which are controlled by particle pH and W_i and meteorological conditions as will be
558 shown in section 3.5.

559 The measured particle-phase water-soluble organic acids contributed on average 6 % to the
560 HR-ToF-AMS-measured organic aerosol mass concentration. The average carbon mass fraction
561 of WSOC_p comprised of these organic acids is 4 %. Previous studies have shown that particle-
562 phase organic acids found in rural environments are oxidation products of gas-phase aliphatic
563 monocarboxylic acids, which are formed in the photochemical oxidation of biogenic unsaturated
564 fatty acids and other BVOC precursors (Kawamura and Gagosian, 1987; Kawamura and Ikushima,

1993; Kerminen et al., 2000; Kawamura and Bikkina, 2016). These particle-phase organic acids can also be produced during the multiphase photochemical aging of ambient organic aerosols (Ervens et al., 2004; Lim et al., 2005; Sorooshian et al., 2007; Sorooshian et al., 2010).

Oxalate is the most abundant measured particle-phase water-soluble organic acid anion (contributing on average 26 % to the total particle-phase organic acid mass concentration), with mass concentrations ranging from 0.01 to 0.34 $\mu\text{g m}^{-3}$ and a average of $0.07 \pm 0.05 \mu\text{g m}^{-3}$. Acetate (average of $0.06 \pm 0.03 \mu\text{g m}^{-3}$) and formate (average of $0.05 \pm 0.03 \mu\text{g m}^{-3}$) are the second and third most abundant measured particle-phase water-soluble organic acid anions, respectively. Particle-phase formate, acetate and maleate showed weak diurnal variations, and may be due, in part, to various emission sources having different diurnal cycles and compensating each other throughout the day. Particle-phase oxalate, malonate and succinate peaked in the mid- to late afternoon, while glutarate generally peaked in the mid-morning. This suggests that while the production of these organic acids is photochemically-driven, they may have different BVOC precursors and/or different photochemical production pathways. In addition, since oxalic (C_2), malonic (C_3), succinic (C_4) and glutaric (C_5) acids belong to the same homologous series of organic diacids, it is possible that the photochemical aging of particle-phase glutaric acid resulted in the formation of its successive homologues via the cleavage of C-C bonds. Hence, organic aerosol photochemical aging may also have contributed to the diurnal profiles of particle-phase oxalate, malonate, succinate and glutarate.

3.5. Gas-particle partitioning of organic acids

The online and simultaneous measurements of gas- and particle-phase organic acid mass concentrations provided the opportunity to study gas-particle partitioning behavior of semi-volatile organic compounds with respect to particle pH, as is more commonly done with semi-volatile inorganic species (see section 3.3). Since formic, acetic and oxalic acids are the three most abundant measured organic acids present in the gas and particle phases, we focus on the gas-particle partitioning behaviors of these three organic acids. The average molar fractions (± 1 standard deviation) of formic, acetic and oxalic acid in the particle phase (i.e., $\epsilon(\text{HCOO}^-)$, $\epsilon(\text{CH}_3\text{CO}_2^-)$ and $\epsilon(\text{C}_2\text{O}_4^{2-})$) are $3.6 \pm 3.6 \%$, $5.8 \pm 5.0 \%$ and $73.7 \pm 9.8 \%$, respectively. The uncertainties of these ratios for formic, acetic and oxalic acids are 16, 16 and 17 %, respectively,

594 which are obtained from the propagation of their SF₆-CIMS and PILS-HPIC measurement
595 uncertainties.

596 3.5.1. Oxalic acid

597 To investigate the factors affecting oxalic acid gas-particle partitioning, the equation for
598 the S curve describing the dependence of oxalic acid gas-particle partitioning (i.e., $\varepsilon(\text{C}_2\text{O}_4^{2-}) =$
599 $\text{C}_2\text{O}_4^{2-} / (\text{C}_2\text{H}_2\text{O}_4 + \text{C}_2\text{O}_4^{2-})$) on particle pH is derived. As shown in SI section S3, the analytically
600 calculated S curve for $\varepsilon(\text{C}_2\text{O}_4^{2-})$ can be simplified to:

$$601 \quad \varepsilon(\text{C}_2\text{O}_4^{2-}) \cong \frac{H_{\text{C}_2\text{H}_2\text{O}_4} W_i RT \left(\frac{\gamma_H + \gamma_{\text{C}_2\text{HO}_4^-}}{\gamma_{\text{C}_2\text{H}_2\text{O}_4}} 10^{-\text{pH} + K_{a1}} \right) \times 0.987 \times 10^{-14}}{\gamma_H + \gamma_{\text{C}_2\text{HO}_4^-} 10^{-\text{pH}} + H_{\text{C}_2\text{H}_2\text{O}_4} W_i RT \left(\frac{\gamma_H + \gamma_{\text{C}_2\text{HO}_4^-}}{\gamma_{\text{C}_2\text{H}_2\text{O}_4}} 10^{-\text{pH} + K_{a1}} \right) \times 0.987 \times 10^{-14}} \quad (4)$$

602 where $H_{\text{C}_2\text{H}_2\text{O}_4}$ (mole L⁻¹ atm⁻¹) is the Henry's law constant for oxalic acid, K_{a1} (mole L⁻¹) is the
603 first acid dissociation constant for oxalic acid, R is the gas constant (8.314 m³ Pa K⁻¹ mol⁻¹), T is
604 temperature (K), and γ_i 's are activity coefficients. We used the web version of AIOMFAC
605 (www.aiomfac.caltech.edu) (Zuend et al., 2008; Zuend et al., 2011; Zuend et al., 2012) to compute
606 an average $\gamma_{\text{C}_2\text{H}_2\text{O}_4}$ value of 0.0492. Since AIOMFAC does not predict $\gamma_H + \gamma_{\text{C}_2\text{HO}_4^-}$, we assumed
607 that $\gamma_H + \gamma_{\text{C}_2\text{HO}_4^-} = \gamma_H + \gamma_{\text{NO}_3^-}$, and used the ISORROPIA-predicted $\gamma_H + \gamma_{\text{NO}_3^-}$ value of 0.07. We used
608 the average of $H_{\text{C}_2\text{H}_2\text{O}_4}$ values provided by Clegg et al. (1996), Compernelle and Muller (2014)
609 and Saxena and Hildemann (1996) (6.11×10^8 mole L⁻¹ atm⁻¹ at 25 °C), and accounted for the
610 effect of temperature using equation 19 in Sander (2015). Although K_{a1} also depends on
611 temperature, we used the K_{a1} value at 25 °C (5.62×10^{-2} mole L⁻¹, (Haynes, 2014)) for all the
612 oxalic acid S curve calculations since equations that compute K_{a1} values for pure aqueous oxalic
613 acid solutions at different temperatures are not available in the literature. In addition, the
614 temperatures observed in this study were close to 25 °C (study-average temperature = 23.4 ± 4.0
615 °C).

616 Different S curves for $\varepsilon(\text{C}_2\text{O}_4^{2-})$ are calculated using 1-hour average values obtained from
617 the diurnal profiles of temperature and W_i (specifically at 00:30, 06:30 and 12:30). The shape of
618 the S curve changes with the time of day due to the diurnal variations of temperature and W_i (Fig
619 S12 and SI section S3). The S curves for $\varepsilon(\text{C}_2\text{O}_4^{2-})$ are very different from those of other acids,

620 such as $\varepsilon(\text{NO}_3^-)$ (shown in Fig. 4b). From the S curves for $\varepsilon(\text{C}_2\text{O}_4^{2-})$, which are calculated using
 621 conditions in this study, some molar fraction of oxalic acid is always expected to be present in the
 622 particle phase, even at low particle pH (i.e., the S curve does not go to zero at low pH). In contrast,
 623 HNO_3 is expected to be present primarily in the gas phase at low particle pH (i.e., $\text{pH} < 1$) under
 624 similar temperature and W_i conditions. This is due primarily to differences in the Henry's law
 625 constants for the two acids. H_{HNO_3} ($2.57 \times 10^5 \text{ mole L}^{-1} \text{ atm}^{-1}$) at 23.4°C is three orders of
 626 magnitude smaller than $H_{\text{C}_2\text{H}_2\text{O}_4}$ ($7.27 \times 10^8 \text{ mole L}^{-1} \text{ atm}^{-1}$) (Clegg and Brimblecombe, 1990;
 627 Sander, 2015). This means that some undissociated form of oxalate can be found in the particle
 628 phase at any pH, and the molar fraction of this form increases with particle W_i (see Fig. S12).
 629 Oxalic acid's very high Henry's law constant combined with the W_i conditions in this study
 630 ensures that some fraction of the organic acid will be in the particle phase regardless the particle
 631 pH.

632 Figure 7 compares the measured $\varepsilon(\text{C}_2\text{O}_4^{2-})$ vs. ISORROPIA-predicted PM_1 pH to the
 633 analytically calculated S curves(s). The S curve is calculated based on the average temperature and
 634 W_i from 13 September to 6 October ($23.4 \pm 4.0^\circ\text{C}$ and $1.6 \pm 1.7 \mu\text{g m}^{-3}$, respectively). We also
 635 calculated the “upper” and “lower” bounds of this S curve based on one standard deviation from
 636 the average temperature and average W_i . Temperature = 27.4°C and $W_i = 0.5 \mu\text{g m}^{-3}$ are used for
 637 calculations of the “lower” bound, while temperature = 19.4°C and $W_i = 3.3 \mu\text{g m}^{-3}$ are used for
 638 calculations of the “upper” bound. For the ambient data, a range in W_i (0.5 to $4 \mu\text{g m}^{-3}$) and
 639 temperature (15 to 31°C) is chosen to be close to the analytical calculation. As shown in Fig. 7,
 640 the measured $\varepsilon(\text{C}_2\text{O}_4^{2-})$ generally converged around the S curve calculated using the average
 641 temperature and W_i values. Although there is some scatter, the measured ratios are mostly within
 642 the “upper” and “lower” bounds of the S curve.

643 Since the measured $\varepsilon(\text{C}_2\text{O}_4^{2-})$ are in general agreement with the analytically calculated S
 644 curve (Fig. 7), we can use the S curve to understand qualitatively how high NH_3 events at the site
 645 affect oxalic acid gas-particle partitioning. Here we define high NH_3 events as periods where the
 646 NH_3 concentration was higher than 13.3 ppb (which is the average NH_3 concentration + 1 standard
 647 deviation). As discussed in section 3.3, the PM_1 pH during high NH_3 events is 2.5 ± 0.6 , which is
 648 slightly higher than the average PM_1 pH of 2.2 ± 0.6 . Based on the S curve calculated using the

average temperature and W_i values, $\epsilon(\text{C}_2\text{O}_4^{2-})$ increases from 81 % to 89 % when particle pH increases from 2.2 to 2.5. While this result indicates that high NH_3 concentrations can raise the particle pH sufficiently such that it can promote gas-to-particle partitioning of oxalic acid, this is not always the case. Specifically, increasing the particle pH from -2 (or lower) to 1 will not result in a significant increase in $\epsilon(\text{C}_2\text{O}_4^{2-})$. Therefore, whether or not particle pH, and consequently oxalic acid gas-particle partitioning, is sensitive to NH_3 concentration depends strongly on particle pH values.

We also examined how well the analytically calculated S curve for $\epsilon(\text{C}_2\text{O}_4^{2-})$ captures diurnal variations of the measured $\epsilon(\text{C}_2\text{O}_4^{2-})$. The ambient data is divided into two 12 hour sets (08:00 to 19:59 and 20:00 to 07:59) based on the diurnal profile of solar irradiance. Two S curves and their corresponding “upper” and “lower” bounds are calculated based on the average temperature and W_i of the two data sets, and are subsequently compared to the ambient data. As shown in Fig. S13, the measured $\epsilon(\text{C}_2\text{O}_4^{2-})$ in both data sets are generally consistent with predicted values.

A number of inferences can be drawn from the overall good agreement between the predicted and measured molar fractions of oxalic acid in the particle phase in Figs. 7 and S13. Our assumptions regarding the activity coefficients, Henry’s law constant and acid dissociation constants used in the S curve calculations of $\epsilon(\text{C}_2\text{O}_4^{2-})$ are reasonable for the conditions of this study (or are at least self-consistent). Analytically calculated S curves are a simple way of exploring how the gas-particle partitioning of semi-volatile inorganic and organic compounds in the atmosphere are affected by the compound’s physicochemical properties (e.g., Henry’s law constants and acid dissociation constants), temperature, W_i and pH. Overall, these results indicate that particle-phase oxalate is in equilibrium with gas-phase oxalic acid, and that particle pH can influence particle-phase oxalate concentrations. It also showed that particle-phase oxalate can be found over a broad pH range, and that the presence of oxalate does not necessarily provide insights of the particle pH. Because of its high Henry’s law constant, particle-phase oxalate can be found in aerosols even at extremely low pH values (i.e., the flat region in Fig. 7), although our data cannot be used to test this since ambient particle pH values in this study are too high.

3.5.2 Formic and acetic acids

Similar comparisons between the predicted and measured $\varepsilon(\text{HCOO}^-)$ and $\varepsilon(\text{CH}_3\text{CO}_2^-)$ can also be made. Derivation of the equations for S curves describing the dependence of formic and acetic acid gas-particle partitioning (i.e., $\varepsilon(\text{HCOO}^-) = \text{HCOO}^- / (\text{HCOOH} + \text{HCOO}^-)$ and $\varepsilon(\text{CH}_3\text{CO}_2^-) = \text{CH}_3\text{CO}_2^- / (\text{CH}_3\text{CO}_2\text{H} + \text{CH}_3\text{CO}_2^-)$, respectively) on particle pH are similar to that of HNO_3 since they are monoprotic acids:

$$\varepsilon(\text{HCOO}^-) = \frac{H_{\text{HCOOH}} W_i R T \left(\frac{\gamma_H + \gamma_{\text{HCOO}^-}}{\gamma_{\text{HCOOH}}} 10^{-\text{pH} + K_{a1}} \right) \times 0.987 \times 10^{-14}}{\gamma_H + \gamma_{\text{HCOO}^-} 10^{-\text{pH}} + H_{\text{HCOOH}} W_i R T \left(\frac{\gamma_H + \gamma_{\text{HCOO}^-}}{\gamma_{\text{HCOOH}}} 10^{-\text{pH} + K_{a1}} \right) \times 0.987 \times 10^{-14}} \quad (5)$$

$$\varepsilon(\text{CH}_3\text{CO}_2^-) = \frac{H_{\text{CH}_3\text{CO}_2\text{H}} W_i R T \left(\frac{\gamma_H + \gamma_{\text{CH}_3\text{CO}_2^-}}{\gamma_{\text{CH}_3\text{CO}_2\text{H}}} 10^{-\text{pH} + K_{a1}} \right) \times 0.987 \times 10^{-14}}{\gamma_H + \gamma_{\text{CH}_3\text{CO}_2^-} 10^{-\text{pH}} + H_{\text{CH}_3\text{CO}_2\text{H}} W_i R T \left(\frac{\gamma_H + \gamma_{\text{CH}_3\text{CO}_2^-}}{\gamma_{\text{CH}_3\text{CO}_2\text{H}}} 10^{-\text{pH} + K_{a1}} \right) \times 0.987 \times 10^{-14}} \quad (6)$$

where H_{HCOOH} and $H_{\text{CH}_3\text{CO}_2\text{H}}$ (mole $\text{L}^{-1} \text{atm}^{-1}$) are the Henry's law constants for formic and acetic acid, K_{a1} 's (mole L^{-1}) are the first acid dissociation constants, R is the gas constant ($8.314 \text{ m}^3 \text{ Pa K}^{-1} \text{ mol}^{-1}$), T is temperature (K), and γ_i 's are activity coefficients. We used the web version of AIOMFAC (www.aiomfac.caltech.edu) (Zuend et al., 2008; Zuend et al., 2011; Zuend et al., 2012) to compute average γ_{HCOOH} and $\gamma_{\text{CH}_3\text{CO}_2\text{H}}$ values of 0.334 and 2.150, respectively. Similar to the case of oxalic acid, we assumed that $\gamma_H + \gamma_{\text{HCOO}^-} = \gamma_H + \gamma_{\text{CH}_3\text{CO}_2^-} = \gamma_H + \gamma_{\text{NO}_3^-}$, and used the ISORROPIA-predicted $\gamma_H + \gamma_{\text{NO}_3^-}$ value of 0.07. Temperature-dependent H_{HCOOH} and $H_{\text{CH}_3\text{CO}_2\text{H}}$ values are obtained from Sander (2015) using the same methodology employed to determine temperature-dependent $H_{\text{C}_2\text{H}_2\text{O}_4}$ values. We used K_{a1} values at 25°C (1.78×10^{-4} mole L^{-1} for formic acid, and 1.75×10^{-5} mole L^{-1} for acetic acid (Haynes, 2014)) for the S curve calculations.

S curves for $\varepsilon(\text{HCOO}^-)$ and $\varepsilon(\text{CH}_3\text{CO}_2^-)$ calculated based on temperature = 23.4°C and $W_i = 1.6 \mu\text{g m}^{-3}$ can be seen in Fig. 8. Practically no formic or acetic acids are predicted to partition to the particle phase (relative to oxalic acid) for the range of PM_1 pH calculated in this study. This is due to significant differences in the Henry's law constants and acid dissociation constants for the three organic acids. H_{HCOOH} and $H_{\text{CH}_3\text{CO}_2\text{H}}$ (9540 and 5370 mole $\text{L}^{-1} \text{atm}^{-1}$, respectively) at 23.4°C are substantially smaller than $H_{\text{C}_2\text{H}_2\text{O}_4}$ (7.27×10^8 mole $\text{L}^{-1} \text{atm}^{-1}$) (Sander, 2015). The K_{a1} values for formic and acetic acids (1.78×10^{-4} and 1.75×10^{-5} mole L^{-1} , respectively) are also considerably smaller than the K_{a1} value for oxalic acid (5.62×10^{-2} mole L^{-1}) (Haynes, 2014). Note

703 that H_{HNO_3} is between that of $H_{\text{C}_2\text{H}_2\text{O}_4}$ and those of H_{HCOOH} and $H_{\text{CH}_3\text{CO}_2\text{H}}$ (compare Fig. 4b with
704 Figs. 7 and 8).

705 As shown in Fig. 8, higher than expected levels of formate and acetate are observed in the
706 particle phase. This has also been reported in previous studies (Liu et al., 2012). Laboratory tests
707 showed that the disagreement cannot be explained by positive biases in the particle-phase formate
708 and acetate PILS-HPIC measurements resulting from less than 100 % gas removal by the carbon
709 denuder. The measured denuder efficiency for formic acid was $\geq 99.97\%$ (SI section S4). The
710 possibility that formic and acetic acid dimers in the aqueous phase (Schrier et al., 1964; Gilson et
711 al., 1997; Chen et al., 2008) may result in higher than predicted molar fractions of formate and
712 acetate in the particle phase was explored, but also could not explain the observed gas-particle
713 partitioning of these acids (SI section S5). The disagreement could be due to incorrect Henry's law
714 constants for formic and acetic acids. However, the Henry's law constants for formic and acetic
715 acid would have to be $\sim 10^4$ times and $\sim 3 \times 10^5$ times larger than their literature values, respectively,
716 in order for their S curves to match our measured molar fractions of formic and acetic acid in the
717 particle phase. In addition, formic and acetic acids may not be internally mixed with most of the
718 other PM₁ aerosol components (e.g., SO_4^{2-} , NO_3^- , NH_4^+ , $\text{C}_2\text{O}_4^{2-}$), and thus are not associated with
719 acidic aerosols, as assumed above. They may instead be associated with aerosols largely composed
720 of non-volatile cations and have a pH closer to neutral. More research is needed to explain this
721 disagreement.

722 4. Summary

723 Gas- and particle-phase measurements were conducted in Yorkville, Georgia (a rural field
724 site) during fall 2016. The goal of the field study was to understand how NH_3 affects particle
725 acidity, and consequently SOA formation through the gas-particle partitioning of semi-volatile
726 inorganic and organic compounds. Since it is a rural site surrounded by forest, agricultural land
727 and CAFOs, this study provided an opportunity for ambient observations in an area impacted by
728 high local emissions of BVOCs and NH_3 .

729 NH_3 concentrations measured by the NH_3 -CIMS ranged from 0.7 to 39.0 ppb (average 8.1
730 ± 5.2 ppb), which were substantially higher than typical levels in the southeastern U.S.. PM₁
731 inorganic chemical composition, gas-phase HNO_3 and NH_3 concentrations, temperature and RH

Deleted: $\text{CH}_3\text{CO}_2\text{H}$

were used as model inputs in the ISORROPIA-II thermodynamic model to calculate PM_1 pH and W_i . PM_1 pH ranged from 0.9 to 3.8, with an average pH of 2.2 ± 0.6 . The measured and predicted HNO_3 - NO_3^- and NH_3 - NH_4^+ gas-particle partitioning ratios were in good agreement. The measured gas-phase organic acids were estimated to contribute 30 % of the overall $WSOC_g$ on a carbon mass basis, whereas measured particle-phase organic acids comprised 6 % of the total organic aerosol mass concentration and 4 % of the overall $WSOC_p$ on a carbon mass basis. Formic and acetic acids were the most abundant gas-phase organic acids, with averages of 2.2 ± 1.6 and $1.9 \pm 1.3 \mu g m^{-3}$, respectively. Oxalate was the most abundant particle-phase water-soluble organic acid anion, with a average of $0.07 \pm 0.05 \mu g m^{-3}$. Measured oxalic acid gas-particle partitioning ratios generally agreed with analytical predictions, which were based on oxalic acid's physicochemical properties (specifically, its Henry's law constants, acid dissociation constants and activity coefficients), temperature, W_i and particle pH. The partitioning of oxalic acid to the particle phase is highly sensitive to temperature and W_i . In contrast, the partitioning of formic and acetic acids to the particle phase were higher than predicted for reasons currently unknown.

Although past air regulations have resulted in decreased sulfate, nitrate and ammonium aerosol mass concentrations across the U.S., our study suggests that the current limited regulation of NH_3 emissions may result in some increase in the organic aerosol mass concentration due to increased gas-to-particle partitioning of some organic acids. However, in this study, the effect was small since the organic acids comprised a small fraction of the overall organic aerosol mass.

5. Acknowledgements

The authors thank Eric Edgerton (Atmospheric Research and Analysis, Inc.) for providing SEARCH network measurements and meteorological data.

6. Funding

This publication was developed under U.S. Environmental Protection Agency (EPA) STAR Grant R835882 awarded to Georgia Institute of Technology. It has not been formally reviewed by the EPA. The views expressed in this document are solely those of the authors and do not necessarily reflect those of the EPA. EPA does not endorse any products or commercial services mentioned in this publication.

761 **7. Competing financial interests**

762 The authors declare no competing financial interests.

763 **8. Data availability**

764 Data can be accessed by request (rweber@eas.gatech.edu).

765 **9. References**

766 Barbier-Jr, J., and Duprez, D.: Steam Effects in 3-way catalysis, *Applied Catalysis B-Environmental*, 4, 105-140, 10.1016/0926-3373(94)80046-4, 1994.

768 Bertram, A. K., Martin, S. T., Hanna, S. J., Smith, M. L., Bodsworth, A., Chen, Q., Kuwata, M.,
769 Liu, A., You, Y., and Zorn, S. R.: Predicting the relative humidities of liquid-liquid phase
770 separation, efflorescence, and deliquescence of mixed particles of ammonium sulfate, organic
771 material, and water using the organic-to-sulfate mass ratio of the particle and the oxygen-to-carbon
772 elemental ratio of the organic component, *Atmos. Chem. Phys.*, 11, 10995-11006, 10.5194/acp-
773 11-10995-2011, 2011.

774 Blanchard, C. L., Hidy, G. M., Tanenbaum, S., and Edgerton, E. S.: NMOC, ozone, and organic
775 aerosol in the southeastern United States, 1999-2007: 3. Origins of organic aerosol in Atlanta,
776 Georgia, and surrounding areas, *Atmospheric Environment*, 45, 1291-1302,
777 10.1016/j.atmosenv.2010.12.004, 2011.

778 Blanchard, C. L., Hidy, G. M., Tanenbaum, S., Edgerton, E. S., and Hartsell, B. E.: The
779 Southeastern Aerosol Research and Characterization (SEARCH) study: Spatial variations and
780 chemical climatology, 1999-2010, *Journal of the Air & Waste Management Association*, 63, 260-
781 275, 10.1080/10962247.2012.749816, 2013a.

782 Blanchard, C. L., Hidy, G. M., Tanenbaum, S., Edgerton, E. S., and Hartsell, B. E.: The
783 Southeastern Aerosol Research and Characterization (SEARCH) study: Temporal trends in gas
784 and PM concentrations and composition, 1999-2010, *Journal of the Air & Waste Management*
785 *Association*, 63, 247-259, 10.1080/10962247.2012.748523, 2013b.

786 Blanchard, C. L., Tanenbaum, S., and Hidy, G. M.: Source Attribution of Air Pollutant
 787 Concentrations and Trends in the Southeastern Aerosol Research and Characterization (SEARCH)
 788 Network, *Environmental Science & Technology*, 47, 13536-13545, 10.1021/es402876s, 2013c.

789 Bougiatioti, A., Nikolaou, P., Stavroulas, I., Kouvarakis, G., Weber, R., Nenes, A., Kanakidou,
 790 M., and Mihalopoulos, N.: Particle water and pH in the eastern Mediterranean: source variability
 791 and implications for nutrient availability, *Atmos. Chem. Phys.*, 16, 4579-4591, 10.5194/acp-16-
 792 4579-2016, 2016.

793 Boyd, C. M., Sanchez, J., Xu, L., Eugene, A. J., Nah, T., Tuet, W. Y., Guzman, M. I., and Ng, N.
 794 L.: Secondary organic aerosol formation from the beta-pinene+NO₃ system: effect of humidity
 795 and peroxy radical fate, *Atmos. Chem. Phys.*, 15, 7497-7522, 10.5194/acp-15-7497-2015, 2015.

796 Boyd, C. M., Nah, T., Xu, L., Berkemeier, T., and Ng, N. L.: Secondary Organic Aerosol (SOA)
 797 from Nitrate Radical Oxidation of Monoterpenes: Effects of Temperature, Dilution, and Humidity
 798 on Aerosol Formation, Mixing, and Evaporation, *Environmental Science & Technology*, 51, 7831-
 799 7841, 10.1021/acs.est.7b01460, 2017.

800 Canagaratna, M. R., Jayne, J. T., Jimenez, J. L., Allan, J. D., Alfarra, M. R., Zhang, Q., Onasch,
 801 T. B., Drewnick, F., Coe, H., Middlebrook, A., Delia, A., Williams, L. R., Trimborn, A. M.,
 802 Northway, M. J., DeCarlo, P. F., Kolb, C. E., Davidovits, P., and Worsnop, D. R.: Chemical and
 803 microphysical characterization of ambient aerosols with the aerodyne aerosol mass spectrometer,
 804 *Mass Spectrometry Reviews*, 26, 185-222, 10.1002/mas.20115, 2007.

805 Canagaratna, M. R., Jimenez, J. L., Kroll, J. H., Chen, Q., Kessler, S. H., Massoli, P., Hildebrandt
 806 Ruiz, L., Fortner, E., Williams, L. R., Wilson, K. R., Surratt, J. D., Donahue, N. M., Jayne, J. T.,
 807 and Worsnop, D. R.: Elemental ratio measurements of organic compounds using aerosol mass
 808 spectrometry: characterization, improved calibration, and implications, *Atmos. Chem. Phys.*, 15,
 809 253-272, 10.5194/acp-15-253-2015, 2015.

810 Case, J. L., and Zavodsky, B. T.: Evolution of 2016 drought in the Southeastern United States from
 811 a Land surface modeling perspective, *Results in Physics*, 8, 654-656, 10.1016/j.rinp.2017.12.029,
 812 2018.

813 Chen, J. H., Brooks, C. L., and Scheraga, H. A.: Revisiting the carboxylic acid dimers in aqueous
814 solution: Interplay of hydrogen bonding, hydrophobic interactions, and entropy, *Journal of*
815 *Physical Chemistry B*, 112, 242-249, 10.1021/jp074355h, 2008.

816 Clegg, S. L., and Brimblecombe, P.: Equilibrium partial pressures and mean activity and osmotic
817 coefficients of 0-100-percent nitric- acid as a function of temperature, *Journal of Physical*
818 *Chemistry*, 94, 5369-5380, 10.1021/j100376a038, 1990.

819 Clegg, S. L., Brimblecombe, P., and Khan, L.: The Henry's law constant of oxalic acid and its
820 partitioning into the atmospheric aerosol, *Idojaras*, 100, 51-68, 1996.

821 Clegg, S. L., Brimblecombe, P., and Wexler, A. S.: Thermodynamic model of the system H^+ -
822 NH_4^+ - SO_4^{2-} - NO_3^- - H_2O at tropospheric temperatures, *Journal of Physical Chemistry A*, 102,
823 2137-2154, 10.1021/jp973042r, 1998.

824 DeCarlo, P. F., Kimmel, J. R., Trimborn, A., Northway, M. J., Jayne, J. T., Aiken, A. C., Gonin,
825 M., Fuhrer, K., Horvath, T., Docherty, K. S., Worsnop, D. R., and Jimenez, J. L.: Field-deployable,
826 high-resolution, time-of-flight aerosol mass spectrometer, *Analytical Chemistry*, 78, 8281-8289,
827 10.1021/ac061249n, 2006.

828 Dentener, F. J., and Crutzen, P. J.: A 3-DIMENSIONAL MODEL OF THE GLOBAL AMMONIA
829 CYCLE, *Journal of Atmospheric Chemistry*, 19, 331-369, 10.1007/bf00694492, 1994.

830 Eatough, D. J., Wadsworth, A., Eatough, D. A., Crawford, J. W., Hansen, L. D., and Lewis, E. A.:
831 A multiple-system, multi-channel diffusion denuder sampler for the determination of fine-
832 particulate organic material in the atmosphere, *Atmospheric Environment. Part A. General Topics*,
833 27, 1213-1219, 10.1016/0960-1686(93)90247-V, 1993.

834 Edgerton, E. S., Hartsell, B. E., Saylor, R. D., Jansen, J. J., Hansen, D. A., and Hidy, G. M.: The
835 southeastern aerosol research and characterization study: Part II. Filter-based measurements of
836 fine and coarse particulate matter mass and composition, *Journal of the Air & Waste Management*
837 *Association*, 55, 1527-1542, 2005.

838 Edgerton, E. S., Hartsell, B. E., Saylor, R. D., Jansen, J. J., Hansen, D. A., and Hidy, G. M.: The
839 Southeastern Aerosol Research and Characterization Study, part 3: Continuous measurements of

840 fine particulate matter mass and composition, *Journal of the Air & Waste Management*
841 *Association*, 56, 1325-1341, 10.1080/10473289.2006.10464585, 2006.

842 Edgerton, E. S., Saylor, R. D., Hartsell, B. E., Jansen, J. J., and Hansen, D. A.: Ammonia and
843 ammonium measurements from the southeastern United States, *Atmospheric Environment*, 41,
844 3339-3351, 10.1016/j.atmosenv.2006.12.034, 2007.

845 Ellis, R. A., Murphy, J. G., Markovic, M. Z., VandenBoer, T. C., Makar, P. A., Brook, J., and
846 Mihele, C.: The influence of gas-particle partitioning and surface-atmosphere exchange on
847 ammonia during BAQS-Met, *Atmos. Chem. Phys.*, 11, 133-145, 10.5194/acp-11-133-2011, 2011.

848 Ellis, R. A., Jacob, D. J., Sulprizio, M. P., Zhang, L., Holmes, C. D., Schichtel, B. A., Blett, T.,
849 Porter, E., Pardo, L. H., and Lynch, J. A.: Present and future nitrogen deposition to national parks
850 in the United States: critical load exceedances, *Atmos. Chem. Phys.*, 13, 9083-9095, 10.5194/acp-
851 13-9083-2013, 2013.

852 Ervens, B., Feingold, G., Frost, G. J., and Kreidenweis, S. M.: A modeling study of aqueous
853 production of dicarboxylic acids: 1. Chemical pathways and speciated organic mass production,
854 *Journal of Geophysical Research-Atmospheres*, 109, 10.1029/2003jd004387, 2004.

855 Fountoukis, C., and Nenes, A.: ISORROPIA II: a computationally efficient thermodynamic
856 equilibrium model for $K^+-Ca^{2+}-Mg^{2+}-NH_4^+-Na^+-SO_4^{2-}-NO_3^- -Cl^- -H_2O$ aerosols, *Atmos.*
857 *Chem. Phys.*, 7, 4639-4659, 2007.

858 Gilson, M. K., Given, J. A., Bush, B. L., and McCammon, J. A.: The statistical-thermodynamic
859 basis for computation of binding affinities: A critical review, *Biophysical Journal*, 72, 1047-1069,
860 10.1016/s0006-3495(97)78756-3, 1997.

861 Guenther, A. B., Jiang, X., Heald, C. L., Sakulyanontvittaya, T., Duhl, T., Emmons, L. K., and
862 Wang, X.: The Model of Emissions of Gases and Aerosols from Nature version 2.1 (MEGAN2.1):
863 an extended and updated framework for modeling biogenic emissions, *Geoscientific Model*
864 *Development*, 5, 1471-1492, 10.5194/gmd-5-1471-2012, 2012.

865 Guo, H., Xu, L., Bougiatioti, A., Cerully, K. M., Capps, S. L., Hite, J. R., Jr., Carlton, A. G., Lee,
866 S. H., Bergin, M. H., Ng, N. L., Nenes, A., and Weber, R. J.: Fine-particle water and pH in the

867 southeastern United States, *Atmos. Chem. Phys.*, 15, 5211-5228, 10.5194/acp-15-5211-2015,
868 2015.

869 Guo, H., Sullivan, A. P., Campuzano-Jost, P., Schroder, J. C., Lopez-Hilfiker, F. D., Dibb, J. E.,
870 Jimenez, J. L., Thornton, J. A., Brown, S. S., Nenes, A., and Weber, R. J.: Fine particle pH and
871 the partitioning of nitric acid during winter in the northeastern United States, *Journal of*
872 *Geophysical Research-Atmospheres*, 121, 10355-10376, 10.1002/2016jd025311, 2016.

873 Guo, H., Liu, J. M., Froyd, K. D., Roberts, J. M., Veres, P. R., Hayes, P. L., Jimenez, J. L., Nenes,
874 A., and Weber, R. J.: Fine particle pH and gas-particle phase partitioning of inorganic species in
875 Pasadena, California, during the 2010 CalNex campaign, *Atmos. Chem. Phys.*, 17, 5703-5719,
876 10.5194/acp-17-5703-2017, 2017a.

877 Guo, H., Nenes, A., and Weber, R. J.: The underappreciated role of nonvolatile cations on aerosol
878 ammonium-sulfate molar ratios, *Atmos. Chem. Phys. Discuss.*, 2017, 1-19, 10.5194/acp-2017-
879 737, 2017b.

880 Guo, H., Weber, R. J., and Nenes, A.: High levels of ammonia do not raise fine particle pH
881 sufficiently to yield nitrogen oxide-dominated sulfate production, *Scientific Reports*, 7,
882 10.1038/s41598-017-11704-0, 2017c.

883 Hansen, D. A., Edgerton, E. S., Hartsell, B. E., Jansen, J. J., Kandasamy, N., Hidy, G. M., and
884 Blanchard, C. L.: The southeastern aerosol research and characterization study: Part 1-overview,
885 *Journal of the Air & Waste Management Association*, 53, 1460-1471, 2003.

886 Haynes, W. M.: *CRC handbook of chemistry and physics: A ready-reference book of chemical*
887 *and physical data.* , Boca Raton: CRC Press, 2014.

888 Hennigan, C. J., Izumi, J., Sullivan, A. P., Weber, R. J., and Nenes, A.: A critical evaluation of
889 proxy methods used to estimate the acidity of atmospheric particles, *Atmos. Chem. Phys.*, 15,
890 2775-2790, 10.5194/acp-15-2775-2015, 2015.

891 Huey, L. G., Hanson, D. R., and Howard, C. J.: Reactions of SF₆- and I- with Atmospheric Trace
892 Gases, *Journal of Physical Chemistry*, 99, 5001-5008, 10.1021/j100014a021, 1995.

893 Huey, L. G., Tanner, D. J., Slusher, D. L., Dibb, J. E., Arimoto, R., Chen, G., Davis, D., Buhr, M.
 894 P., Nowak, J. B., Mauldin, R. L., Eisele, F. L., and Kosciuch, E.: CIMS measurements of HNO₃
 895 and SO₂ at the South Pole during ISCAT 2000, *Atmospheric Environment*, 38, 5411-5421,
 896 10.1016/j.atmosenv.2004.04.037, 2004.

897 Kawamura, K., and Gagosian, R. B.: Implication of omega-oxocarboxylic acids in the remote
 898 marine atmosphere for photo-oxidation of unsaturated fatty acids, *Nature*, 325, 330-332,
 899 10.1038/325330a0, 1987.

900 Kawamura, K., and Ikushima, K.: Seasonal changes in the distribution of dicarboxylic acids in the
 901 urban atmosphere, *Environmental Science & Technology*, 27, 2227-2235, 10.1021/es00047a033,
 902 1993.

903 Kawamura, K., and Bikkina, S.: A review of dicarboxylic acids and related compounds in
 904 atmospheric aerosols: Molecular distributions, sources and transformation, *Atmospheric Research*,
 905 170, 140-160, 10.1016/j.atmosres.2015.11.018, 2016.

906 Kerminen, V. M., Ojanen, C., Pakkanen, T., Hillamo, R., Aurela, M., and Merilainen, J.: Low-
 907 molecular-weight dicarboxylic acids in an urban and rural atmosphere, *Journal of Aerosol Science*,
 908 31, 349-362, 10.1016/s0021-8502(99)00063-4, 2000.

909 Lamarque, J. F., Bond, T. C., Eyring, V., Granier, C., Heil, A., Klimont, Z., Lee, D., Lioussé, C.,
 910 Mieville, A., Owen, B., Schultz, M. G., Shindell, D., Smith, S. J., Stehfest, E., Van Aardenne, J.,
 911 Cooper, O. R., Kainuma, M., Mahowald, N., McConnell, J. R., Naik, V., Riahi, K., and van
 912 Vuuren, D. P.: Historical (1850-2000) gridded anthropogenic and biomass burning emissions of
 913 reactive gases and aerosols: methodology and application, *Atmos. Chem. Phys.*, 10, 7017-7039,
 914 10.5194/acp-10-7017-2010, 2010.

915 Laskin, A., Laskin, J., and Nizkorodov, S. A.: Chemistry of Atmospheric Brown Carbon, *Chemical*
 916 *Reviews*, 115, 4335-4382, 10.1021/cr5006167, 2015.

917 Laskin, J., Laskin, A., Roach, P. J., Slys, G. W., Anderson, G. A., Nizkorodov, S. A., Bones, D.
 918 L., and Nguyen, L. Q.: High-Resolution Desorption Electrospray Ionization Mass Spectrometry

919 for Chemical Characterization of Organic Aerosols, *Analytical Chemistry*, 82, 2048-2058,
 920 10.1021/ac902801f, 2010.

921 Lee, B. H., Mohr, C., Lopez-Hilfiker, F. D., Lutz, A., Hallquist, M., Lee, L., Romer, P., Cohen, R.
 922 C., Iyer, S., Kurten, T., Hu, W. W., Day, D. A., Campuzano-Jost, P., Jimenez, J. L., Xu, L., Ng,
 923 N. L., Guo, H. Y., Weber, R. J., Wild, R. J., Brown, S. S., Koss, A., de Gouw, J., Olson, K.,
 924 Goldstein, A. H., Seco, R., Kim, S., McAvey, K., Shepson, P. B., Starn, T., Baumann, K.,
 925 Edgerton, E. S., Liu, J. M., Shilling, J. E., Miller, D. O., Brune, W., Schobesberger, S., D'Ambro,
 926 E. L., and Thornton, J. A.: Highly functionalized organic nitrates in the southeast United States:
 927 Contribution to secondary organic aerosol and reactive nitrogen budgets, *Proceedings of the*
 928 *National Academy of Sciences of the United States of America*, 113, 1516-1521,
 929 10.1073/pnas.1508108113, 2016.

930 Lee, B. P., Li, Y. J., Yu, J. Z., Louie, P. K. K., and Chan, C. K.: Characteristics of submicron
 931 particulate matter at the urban roadside in downtown Hong Kong-Overview of 4 months of
 932 continuous high-resolution aerosol mass spectrometer measurements, *Journal of Geophysical*
 933 *Research-Atmospheres*, 120, 7040-7058, 10.1002/2015jd023311, 2015.

934 Lee, H. J., Laskin, A., Laskin, J., and Nizkorodov, S. A.: Excitation-Emission Spectra and
 935 Fluorescence Quantum Yields for Fresh and Aged Biogenic Secondary Organic Aerosols,
 936 *Environmental Science & Technology*, 47, 5763-5770, 10.1021/es400644c, 2013.

937 Lim, H. J., Carlton, A. G., and Turpin, B. J.: Isoprene forms secondary organic aerosol through
 938 cloud processing: Model simulations, *Environmental Science & Technology*, 39, 4441-4446,
 939 10.1021/es048039h, 2005.

940 Liu, J., Zhang, X., Parker, E. T., Veres, P. R., Roberts, J. M., de Gouw, J. A., Hayes, P. L., Jimenez,
 941 J. L., Murphy, J. G., Ellis, R. A., Huey, L. G., and Weber, R. J.: On the gas-particle partitioning of
 942 soluble organic aerosol in two urban atmospheres with contrasting emissions: 2. Gas and particle
 943 phase formic acid, *Journal of Geophysical Research-Atmospheres*, 117, 10.1029/2012jd017912,
 944 2012.

945 Livingston, C., Rieger, P., and Winer, A.: Ammonia emissions from a representative in-use fleet
 946 of light and medium-duty vehicles in the California South Coast Air Basin, *Atmospheric*
 947 *Environment*, 43, 3326-3333, 10.1016/j.atmosenv.2009.04.009, 2009.

948 Malm, W. C., and Day, D. E.: Estimates of aerosol species scattering characteristics as a function
 949 of relative humidity, *Atmospheric Environment*, 35, 2845-2860, 10.1016/s1352-2310(01)00077-
 950 2, 2001.

951 Middlebrook, A. M., Bahreini, R., Jimenez, J. L., and Canagaratna, M. R.: Evaluation of
 952 Composition-Dependent Collection Efficiencies for the Aerodyne Aerosol Mass Spectrometer
 953 using Field Data, *Aerosol Science and Technology*, 46, 258-271, 10.1080/02786826.2011.620041,
 954 2012.

955 Na, K., Song, C., Switzer, C., and Cocker, D. R.: Effect of ammonia on secondary organic aerosol
 956 formation from alpha-Pinene ozonolysis in dry and humid conditions, *Environmental Science &*
 957 *Technology*, 41, 6096-6102, 10.1021/es061956y, 2007.

958 Nah, T., Ji, Y., Tanner, D. J., Guo, H., Sullivan, A. P., Ng, N. L., Weber, R. J., and Huey, L. G.:
 959 Real-time measurements of gas-phase organic acids using SF₆- chemical ionization mass
 960 spectrometry, *Atmos. Meas. Tech. Discuss.*, 2018, 1-40, 10.5194/amt-2018-46, 2018.

961 Nenes, A., Pandis, S. N., and Pilinis, C.: ISORROPIA: A new thermodynamic equilibrium model
 962 for multiphase multicomponent inorganic aerosols, *Aquatic Geochemistry*, 4, 123-152,
 963 10.1023/a:1009604003981, 1998.

964 Neuman, J. A., Ryerson, T. B., Huey, L. G., Jakoubek, R., Nowak, J. B., Simons, C., and
 965 Fehsenfeld, F. C.: Calibration and evaluation of nitric acid and ammonia permeation tubes by UV
 966 optical absorption, *Environmental Science & Technology*, 37, 2975-2981, 10.1021/es0264221,
 967 2003.

968 Ng, N. L., Brown, S. S., Archibald, A. T., Atlas, E., Cohen, R. C., Crowley, J. N., Day, D. A.,
 969 Donahue, N. M., Fry, J. L., Fuchs, H., Griffin, R. J., Guzman, M. I., Herrmann, H., Hodzic, A.,
 970 Iinuma, Y., Jimenez, J. L., Kiendler-Scharr, A., Lee, B. H., Luecken, D. J., Mao, J. Q., McLaren,
 971 R., Mutzel, A., Osthoff, H. D., Ouyang, B., Picquet-Varrau, B., Platt, U., Pye, H. O. T., Rudich,

972 Y., Schwantes, R. H., Shiraiwa, M., Stutz, J., Thornton, J. A., Tilgner, A., Williams, B. J., and
 973 Zaveri, R. A.: Nitrate radicals and biogenic volatile organic compounds: oxidation, mechanisms,
 974 and organic aerosol, *Atmos. Chem. Phys.*, 17, 2103-2162, 10.5194/acp-17-2103-2017, 2017.

975 Nowak, J. B., Huey, L. G., Eisele, F. L., Tanner, D. J., Mauldin, R. L., Cantrell, C., Kosciuch, E.,
 976 and Davis, D. D.: Chemical ionization mass spectrometry technique for detection of
 977 dimethylsulfoxide and ammonia, *Journal of Geophysical Research-Atmospheres*, 107,
 978 10.1029/2001jd001058, 2002.

979 Nowak, J. B., Huey, L. G., Russell, A. G., Tian, D., Neuman, J. A., Orsini, D., Sjostedt, S. J.,
 980 Sullivan, A. P., Tanner, D. J., Weber, R. J., Nenes, A., Edgerton, E., and Fehsenfeld, F. C.:
 981 Analysis of urban gas phase ammonia measurements from the 2002 Atlanta Aerosol Nucleation
 982 and Real-Time Characterization Experiment (ANARChE), *Journal of Geophysical Research-*
 983 *Atmospheres*, 111, 14, 10.1029/2006jd007113, 2006.

984 Orsini, D. A., Ma, Y. L., Sullivan, A., Sierau, B., Baumann, K., and Weber, R. J.: Refinements to
 985 the particle-into-liquid sampler (PILS) for ground and airborne measurements of water soluble
 986 aerosol composition, *Atmospheric Environment*, 37, 1243-1259, 10.1016/s1352-2310(02)01015-
 987 4, 2003.

988 Park Williams, A., Cook, B. I., Smerdon, J. E., Bishop, D. A., Seager, R., and Mankin, J. S.: The
 989 2016 Southeastern U.S. Drought: An Extreme Departure From Centennial Wetting and Cooling,
 990 *Journal of Geophysical Research: Atmospheres*, 122, 10,888-810,905, 10.1002/2017JD027523,
 991 2017.

992 Pechony, O., and Shindell, D. T.: Driving forces of global wildfires over the past millennium and
 993 the forthcoming century, *Proceedings of the National Academy of Sciences of the United States*
 994 *of America*, 107, 19167-19170, 10.1073/pnas.1003669107, 2010.

995 Pye, H. O. T., Luecken, D. J., Xu, L., Boyd, C. M., Ng, N. L., Baker, K. R., Ayres, B. R., Bash, J.
 996 O., Baumann, K., Carter, W. P. L., Edgerton, E., Fry, J. L., Hutzell, W. T., Schwede, D. B., and
 997 Shepson, P. B.: Modeling the Current and Future Roles of Particulate Organic Nitrates in the
 998 Southeastern United States, *Environmental Science & Technology*, 49, 14195-14203,
 999 10.1021/acs.est.5b03738, 2015.

1000 Reis, S., Pinder, R. W., Zhang, M., Lijie, G., and Sutton, M. A.: Reactive nitrogen in atmospheric
 1001 emission inventories, *Atmos. Chem. Phys.*, 9, 7657-7677, 10.5194/acp-9-7657-2009, 2009.

1002 Sander, R.: Compilation of Henry's law constants (version 4.0) for water as solvent, *Atmos. Chem.*
 1003 *Phys.*, 15, 4399-4981, 10.5194/acp-15-4399-2015, 2015.

1004 Saxena, P., and Hildemann, L. M.: Water-soluble organics in atmospheric particles: A critical
 1005 review of the literature and application of thermodynamics to identify candidate compounds,
 1006 *Journal of Atmospheric Chemistry*, 24, 57-109, 10.1007/bf00053823, 1996.

1007 Saylor, R., Myles, L., Sibble, D., Caldwell, J., and Xing, J.: Recent trends in gas-phase ammonia
 1008 and PM_{2.5} ammonium in the Southeast United States, *Journal of the Air & Waste Management*
 1009 *Association*, 65, 347-357, 10.1080/10962247.2014.992554, 2015.

1010 Schrier, E. E., Pottle, M., and Scheraga, H. A.: The Influence of Hydrogen and Hydrophobic Bonds
 1011 on the Stability of the Carboxylic Acid Dimers in Aqueous Solution, *Journal of the American*
 1012 *Chemical Society*, 86, 3444-3449, 10.1021/ja01071a009, 1964.

1013 Seinfeld, J. H., and Pandis, S. N.: *Atmospheric chemistry and physics : from air pollution to*
 1014 *climate change*, Third edition. ed., John Wiley & Sons, Inc., Hoboken, New Jersey, xxvi, 1120
 1015 pages pp., 2016.

1016 Shi, G. L., Xu, J., Peng, X., Xiao, Z. M., Chen, K., Tian, Y. Z., Guan, X. B., Feng, Y. C., Yu, H.
 1017 F., Nenes, A., and Russell, A. G.: pH of Aerosols in a Polluted Atmosphere: Source Contributions
 1018 to Highly Acidic Aerosol, *Environmental Science & Technology*, 51, 4289-4296,
 1019 10.1021/acs.est.6b05736, 2017.

1020 Song, M., Marcolli, C., Krieger, U. K., Zuend, A., and Peter, T.: Liquid-liquid phase separation
 1021 and morphology of internally mixed dicarboxylic acids/ammonium sulfate/water particles, *Atmos.*
 1022 *Chem. Phys.*, 12, 2691-2712, 10.5194/acp-12-2691-2012, 2012.

1023 Song, S., Gao, M., Xu, W., Shao, J., Shi, G., Wang, S., Wang, Y., Sun, Y., and McElroy, M. B.:
 1024 Fine particle pH for Beijing winter haze as inferred from different thermodynamic equilibrium
 1025 models, *Atmos. Chem. Phys. Discuss.*, 2018, 1-26, 10.5194/acp-2018-6, 2018.

1026 Sorooshian, A., Ng, N. L., Chan, A. W. H., Feingold, G., Flagan, R. C., and Seinfeld, J. H.:
 1027 Particulate organic acids and overall water-soluble aerosol composition measurements from the
 1028 2006 Gulf of Mexico Atmospheric Composition and Climate Study (GoMACCS), *Journal of*
 1029 *Geophysical Research-Atmospheres*, 112, 16, 10.1029/2007jd008537, 2007.

1030 Sorooshian, A., Murphy, S. M., Hersey, S., Bahreini, R., Jonsson, H., Flagan, R. C., and Seinfeld,
 1031 J. H.: Constraining the contribution of organic acids and AMS m/z 44 to the organic aerosol
 1032 budget: On the importance of meteorology, aerosol hygroscopicity, and region, *Geophys. Res.*
 1033 *Lett.*, 37, 5, 10.1029/2010gl044951, 2010.

1034 Spaulding, R. S., Talbot, R. W., and Charles, M. J.: Optimization of a mist chamber (cofer
 1035 scrubber) for sampling water-soluble organics in air, *Environmental Science & Technology*, 36,
 1036 1798-1808, 10.1021/es011189x, 2002.

1037 Suarez-Bertoa, R., Zardini, A. A., and Astorga, C.: Ammonia exhaust emissions from spark
 1038 ignition vehicles over the New European Driving Cycle, *Atmospheric Environment*, 97, 43-53,
 1039 10.1016/j.atmosenv.2014.07.050, 2014.

1040 Sullivan, A. P., Weber, R. J., Clements, A. L., Turner, J. R., Bae, M. S., and Schauer, J. J.: A
 1041 method for on-line measurement of water-soluble organic carbon in ambient aerosol particles:
 1042 Results from an urban site, *Geophysical Research Letters*, 31, 10.1029/2004gl019681, 2004.

1043 Sun, K., Tao, L., Miller, D. J., Pan, D., Golston, L. M., Zondlo, M. A., Griffin, R. J., Wallace, H.
 1044 W., Leong, Y. J., Yang, M. M., Zhang, Y., Mauzerall, D. L., and Zhu, T.: Vehicle Emissions as an
 1045 Important Urban Ammonia Source in the United States and China, *Environmental Science &*
 1046 *Technology*, 51, 2472-2481, 10.1021/acs.est.6b02805, 2017.

1047 Updyke, K. M., Nguyen, T. B., and Nizkorodov, S. A.: Formation of brown carbon via reactions
 1048 of ammonia with secondary organic aerosols from biogenic and anthropogenic precursors,
 1049 *Atmospheric Environment*, 63, 22-31, 10.1016/j.atmosenv.2012.09.012, 2012.

1050 Van Damme, M., Clarisse, L., Heald, C. L., Hurtmans, D., Ngadi, Y., Clerbaux, C., Dolman, A.
 1051 J., Erisman, J. W., and Coheur, P. F.: Global distributions, time series and error characterization

1052 of atmospheric ammonia (NH₃) from IASI satellite observations, *Atmos. Chem. Phys.*, 14, 2905-
1053 2922, 10.5194/acp-14-2905-2014, 2014.

1054 Warner, J. X., Wei, Z. G., Strow, L. L., Dickerson, R. R., and Nowak, J. B.: The global
1055 tropospheric ammonia distribution as seen in the 13-year AIRS measurement record, *Atmos.*
1056 *Chem. Phys.*, 16, 5467-5479, 10.5194/acp-16-5467-2016, 2016.

1057 Warner, J. X., Dickerson, R. R., Wei, Z., Strow, L. L., Wang, Y., and Liang, Q.: Increased
1058 atmospheric ammonia over the world's major agricultural areas detected from space, *Geophysical*
1059 *Research Letters*, 44, 2875-2884, 10.1002/2016gl072305, 2017.

1060 Weber, R. J., Orsini, D., Daun, Y., Lee, Y. N., Klotz, P. J., and Brechtel, F.: A particle-into-liquid
1061 collector for rapid measurement of aerosol bulk chemical composition, *Aerosol Science and*
1062 *Technology*, 35, 718-727, 10.1080/02786820152546761, 2001.

1063 Weber, R. J., Lee, S., Chen, G., Wang, B., Kapustin, V., Moore, K., Clarke, A. D., Mauldin, L.,
1064 Kosciuch, E., Cantrell, C., Eisele, F., Thornton, D. C., Bandy, A. R., Sachse, G. W., and Fuelberg,
1065 H. E.: New particle formation in anthropogenic plumes advecting from Asia observed during
1066 TRACE-P, *Journal of Geophysical Research-Atmospheres*, 108, 13, 10.1029/2002jd003112,
1067 2003.

1068 Weber, R. J., Guo, H., Russell, A. G., and Nenes, A.: High aerosol acidity despite declining
1069 atmospheric sulfate concentrations over the past 15 years, *Nature Geoscience*, 9, 282-+,
1070 10.1038/ngeo2665, 2016.

1071 Whittington, B. I., Jiang, C. J., and Trimm, D. L.: Vehicle exhaust catalysis: I. The relative
1072 importance of catalytic oxidation, steam reforming and water-gas shift reactions, *Catalysis Today*,
1073 26, 41-45, 10.1016/0920-5861(95)00093-u, 1995.

1074 Xing, J., Pleim, J., Mathur, R., Pouliot, G., Hogrefe, C., Gan, C. M., and Wei, C.: Historical
1075 gaseous and primary aerosol emissions in the United States from 1990 to 2010, *Atmos. Chem.*
1076 *Phys.*, 13, 7531-7549, 10.5194/acp-13-7531-2013, 2013.

1077 Xu, L., Guo, H., Boyd, C. M., Klein, M., Bougiatioti, A., Cerully, K. M., Hite, J. R., Isaacman-
1078 VanWertz, G., Kreisberg, N. M., Knote, C., Olson, K., Koss, A., Goldstein, A. H., Hering, S. V.,

1079 de Gouw, J., Baumann, K., Lee, S.-H., Nenes, A., Weber, R. J., and Ng, N. L.: Effects of
 1080 anthropogenic emissions on aerosol formation from isoprene and monoterpenes in the southeastern
 1081 United States, *Proceedings of the National Academy of Sciences of the United States of America*,
 1082 112, 37-42, 10.1073/pnas.1417609112, 2015a.

1083 Xu, L., Suresh, S., Guo, H., Weber, R. J., and Ng, N. L.: Aerosol characterization over the
 1084 southeastern United States using high-resolution aerosol mass spectrometry: spatial and seasonal
 1085 variation of aerosol composition and sources with a focus on organic nitrates, *Atmos. Chem. Phys.*,
 1086 15, 7307-7336, 10.5194/acp-15-7307-2015, 2015b.

1087 Xu, L., Guo, H. Y., Weber, R. J., and Ng, N. L.: Chemical Characterization of Water-Soluble
 1088 Organic Aerosol in Contrasting Rural and Urban Environments in the Southeastern United States,
 1089 *Environmental Science & Technology*, 51, 78-88, 10.1021/acs.est.6b05002, 2017.

1090 Yao, X. H., Hu, Q. J., Zhang, L. M., Evans, G. J., Godri, K. J., and Ng, A. C.: Is vehicular emission
 1091 a significant contributor to ammonia in the urban atmosphere?, *Atmospheric Environment*, 80,
 1092 499-506, 10.1016/j.atmosenv.2013.08.028, 2013.

1093 You, Y., Renbaum-Wolff, L., and Bertram, A. K.: Liquid-liquid phase separation in particles
 1094 containing organics mixed with ammonium sulfate, ammonium bisulfate, ammonium nitrate or
 1095 sodium chloride, *Atmos. Chem. Phys.*, 13, 11723-11734, 10.5194/acp-13-11723-2013, 2013.

1096 You, Y., Kanawade, V. P., de Gouw, J. A., Guenther, A. B., Madronich, S., Sierra-Hernandez, M.
 1097 R., Lawler, M., Smith, J. N., Takahama, S., Ruggeri, G., Koss, A., Olson, K., Baumann, K., Weber,
 1098 R. J., Nenes, A., Guo, H., Edgerton, E. S., Porcelli, L., Brune, W. H., Goldstein, A. H., and Lee,
 1099 S. H.: Atmospheric amines and ammonia measured with a chemical ionization mass spectrometer
 1100 (CIMS), *Atmos. Chem. Phys.*, 14, 12181-12194, 10.5194/acp-14-12181-2014, 2014a.

1101 You, Y., Smith, M. L., Song, M., Martin, S. T., and Bertram, A. K.: Liquid-liquid phase separation
 1102 in atmospherically relevant particles consisting of organic species and inorganic salts, *International*
 1103 *Reviews in Physical Chemistry*, 33, 43-77, 10.1080/0144235x.2014.890786, 2014b.

1104 You, Y., and Bertram, A. K.: Effects of molecular weight and temperature on liquid-liquid phase
 1105 separation in particles containing organic species and inorganic salts, *Atmos. Chem. Phys.*, 15,
 1106 1351-1365, 10.5194/acp-15-1351-2015, 2015.

1107 Yu, H., and Lee, S. H.: Chemical ionisation mass spectrometry for the measurement of
 1108 atmospheric amines, *Environ. Chem.*, 9, 190-201, 10.1071/en12020, 2012.

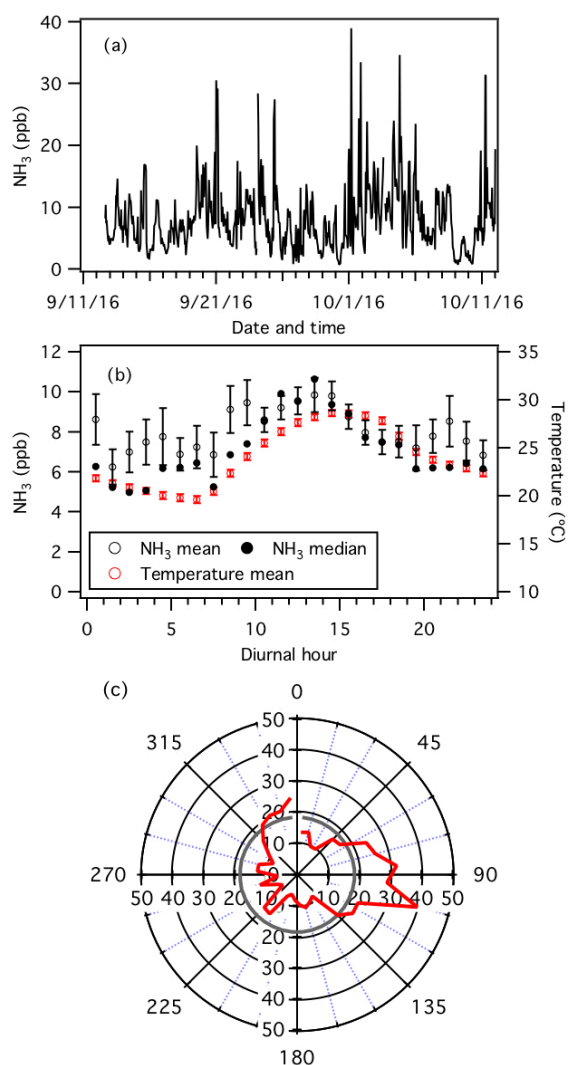
1109 Zhang, H. F., Yee, L. D., Lee, B. H., Curtis, M. P., Worton, D. R., Isaacman-VanWertz, G.,
 1110 Offenberg, J. H., Lewandowski, M., Kleindienst, T. E., Beaver, M. R., Holder, A. L., Lonneman,
 1111 W. A., Docherty, K. S., Jaoui, M., Pye, H. O. T., Hu, W. W., Day, D. A., Campuzano-Jost, P.,
 1112 Jimenez, J. L., Guo, H. Y., Weber, R. J., de Gouw, J., Koss, A. R., Edgerton, E. S., Brune, W.,
 1113 Mohr, C., Lopez-Hilfiker, F. D., Lutz, A., Kreisberg, N. M., Spielman, S. R., Hering, S. V., Wilson,
 1114 K. R., Thornton, J. A., and Goldstein, A. H.: Monoterpenes are the largest source of summertime
 1115 organic aerosol in the southeastern United States, *Proceedings of the National Academy of*
 1116 *Sciences of the United States of America*, 115, 2038-2043, 10.1073/pnas.1717513115, 2018.

1117 Zuend, A., Marcolli, C., Luo, B. P., and Peter, T.: A thermodynamic model of mixed organic-
 1118 inorganic aerosols to predict activity coefficients, *Atmos. Chem. Phys.*, 8, 4559-4593,
 1119 10.5194/acp-8-4559-2008, 2008.

1120 Zuend, A., Marcolli, C., Booth, A. M., Lienhard, D. M., Soonsin, V., Krieger, U. K., Topping, D.
 1121 O., McFiggans, G., Peter, T., and Seinfeld, J. H.: New and extended parameterization of the
 1122 thermodynamic model AIOMFAC: calculation of activity coefficients for organic-inorganic
 1123 mixtures containing carboxyl, hydroxyl, carbonyl, ether, ester, alkenyl, alkyl, and aromatic
 1124 functional groups, *Atmos. Chem. Phys.*, 11, 9155-9206, 10.5194/acp-11-9155-2011, 2011.

1125 Zuend, A., Marcolli, C., Luo, B. P., and Peter, T.: A thermodynamic model of mixed organic-
 1126 inorganic aerosols to predict activity coefficients (vol 8, pg 4559, 2008), *Atmos. Chem. Phys.*, 12,
 1127 10075-10075, 10.5194/acp-12-10075-2012, 2012.

1128

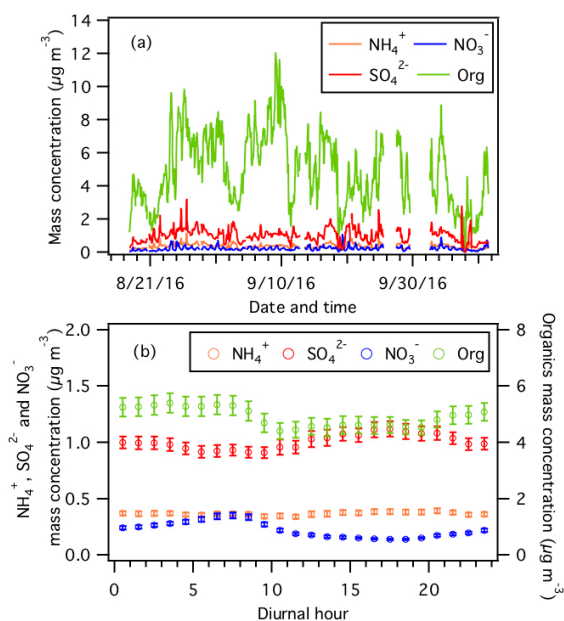


1129

1130 **Figure 1:** Measurements by the NH_3 -CIMS during the second half of the study. (a) Time series of
 1131 NH_3 concentration. The data is displayed as 1-hour averages. (b) Diurnal profiles of NH_3
 1132 concentration (mean and median) and temperature. Error bars shown are the standard errors. Dates
 1133 and times displayed are local time. All the concentrations represent averages in 1-hour intervals

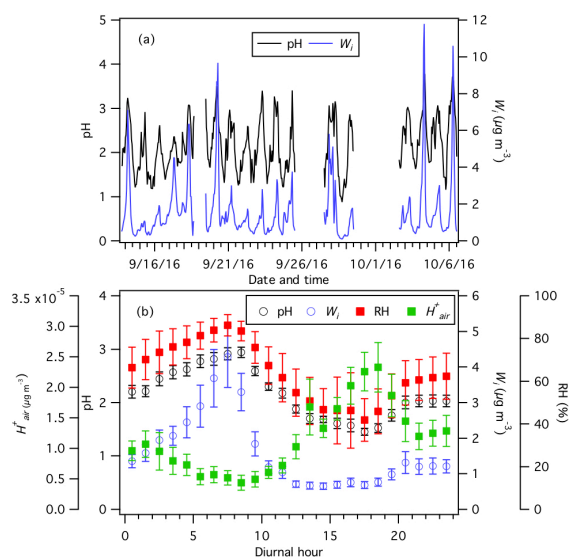
1134 and the standard errors are plotted as error bars. (c) Average NH_3 concentration normalized to
 1135 wind speed (i.e., NH_3 concentration (ppb) \times wind speed (m s^{-1})) in each 10 degrees bin (red line).
 1136 The average normalized NH_3 concentration is shown as a grey line.

1137



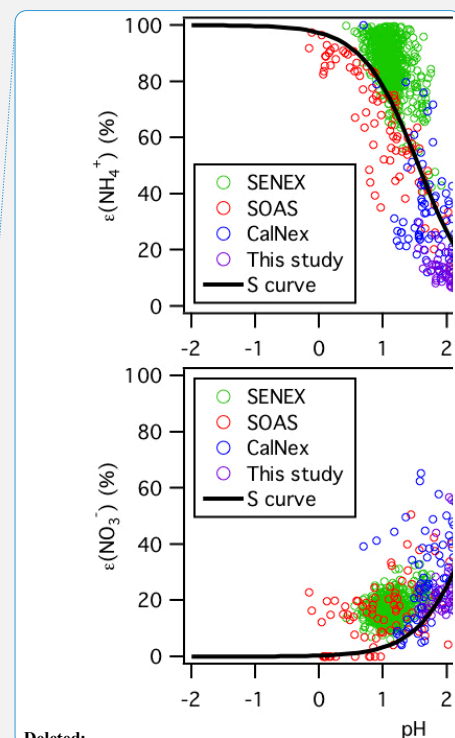
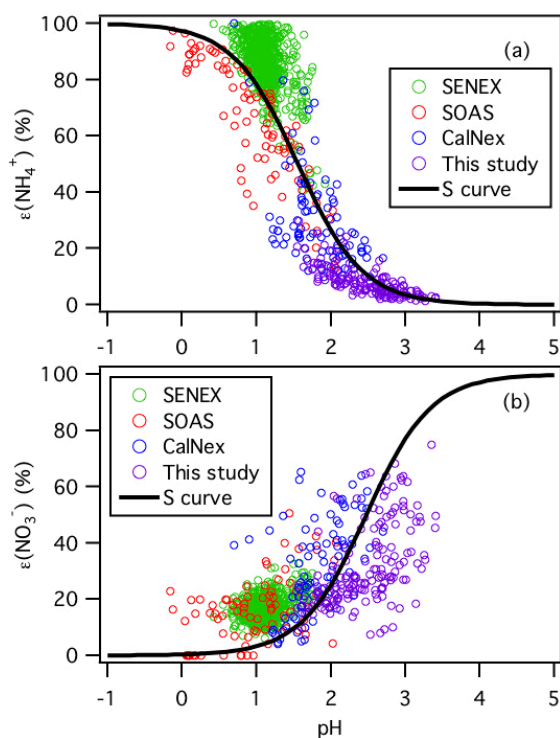
1138

1139 **Figure 2:** (a) Time series and (b) diurnal profiles of non-refractory PM_1 species measured by the
 1140 AMS. Error bars shown in panel (b) are the standard errors. Dates and times displayed are local
 1141 time. All the mass concentrations shown here are obtained from scaling the raw data by 0.5. Refer
 1142 to the text for details.



1143

1144 **Figure 3:** (a) Time series and (b) diurnal profiles of ISORROPIA-predicted PM₁ pH and W_i . The
 1145 diurnal profiles of RH and ISORROPIA-predicted H_{air}^+ are also shown in panel (b). Dates and
 1146 times displayed are local time. All the data shown here represent averages in 1-hour intervals.
 1147 Error bars shown in panel (b) are the standard errors.



1148

1149 **Figure 4:** Analytically calculated S curves of $\epsilon(\text{NH}_4^+)$ and $\epsilon(\text{NO}_3^-)$ and ambient data plotted
 1150 against ISORROPIA-predicted particle pH for this study, SENEX, SOAS and CalNex. For the
 1151 ambient datasets, a narrow range of W_i (1 to 4 $\mu\text{g m}^{-3}$) and temperature (15 to 25 $^\circ\text{C}$) are selected
 1152 to be close to the analytical calculation input (i.e., $W_i = 2.5 \mu\text{g m}^{-3}$ and temperature = 20 $^\circ\text{C}$).
 1153 Similar to Guo et al. (2017a), $\gamma_{\text{NH}_4^+} = 1$ and $\gamma_{\text{H}^+ - \text{NO}_3^-} = \sqrt{\gamma_{\text{H}^+} \gamma_{\text{NO}_3^-}} = 0.28$ are used for the
 1154 analytically calculated S curves.

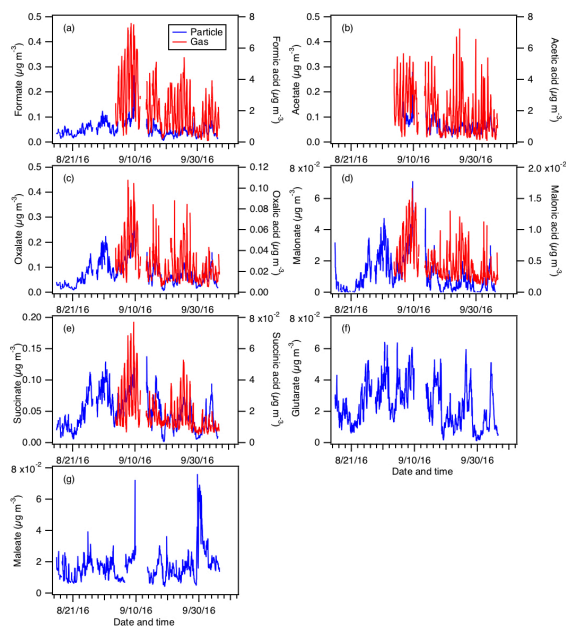


Figure 5: Particle- and gas-phase measurements of (a) formic, (b) acetic, (c) oxalic, (d) malonic, (e) succinic, (f) glutaric, and (g) maleic acids. Particle-phase measurements are shown on the left y axes, while gas-phase measurements are shown on the right y axes. Dates and times displayed are local time. Gas-phase measurements of glutaric and maleic acids are not available.

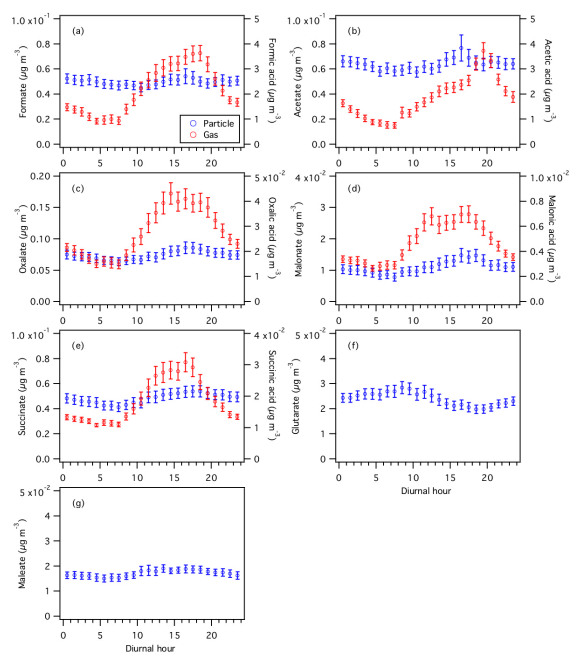
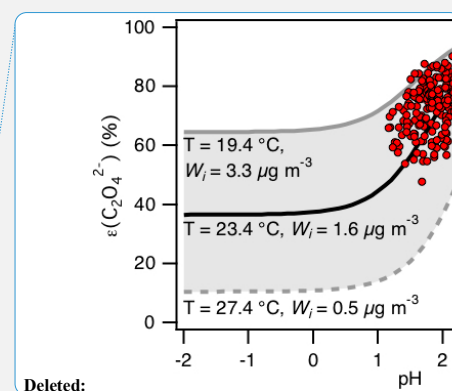
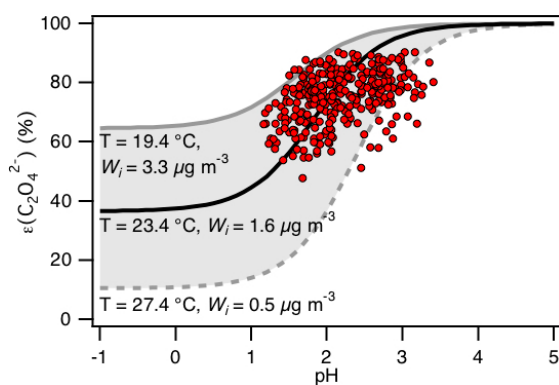


Figure 6: Diurnal profiles of particle- and gas-phase (a) formic, (b) acetic, (c) oxalic, (d) malonic, (e) succinic, (f) glutaric, and (g) maleic acids. Particle-phase measurements are shown on the left y axes, while gas-phase measurements are shown on the right y axes. All the data shown here represent averages in 1-hour intervals. Error bars shown are the standard errors.



Deleted:

Figure 7: Analytically calculated S curve of $\varepsilon(\text{C}_2\text{O}_4^{2-})$ and ambient data from 13 September to 6 October 2016 plotted against ISORROPIA-predicted particle pH. For the ambient data, a range in W_i (0.5 to $4 \mu\text{g m}^{-3}$) and temperature (15 to $31 \text{ }^\circ\text{C}$) are chosen to be close to the analytically calculated outputs. For the analytically calculated S curves, we used $\gamma_{\text{C}_2\text{H}_2\text{O}_4} = 0.0492$ (AIOMFAC predicted). We also assumed that $\gamma_{\text{H}^+}\gamma_{\text{C}_2\text{HO}_4^-} = \gamma_{\text{H}^+}\gamma_{\text{NO}_3^-}$, and used the ISORROPIA-predicted $\gamma_{\text{H}^+}\gamma_{\text{NO}_3^-} = \sqrt{\gamma_{\text{H}^+}\gamma_{\text{NO}_3^-}} = 0.265$. The black line is the S curve calculated using the selected time period's average temperature ($23.4 \pm 4.0 \text{ }^\circ\text{C}$) and W_i ($1.6 \pm 1.7 \mu\text{g m}^{-3}$). The grey lines are S curves calculated using one standard deviation from the average temperature and W_i (i.e., temperature = $27.4 \text{ }^\circ\text{C}$ and $W_i = 0.5 \mu\text{g m}^{-3}$ for dotted grey line, temperature = $19.4 \text{ }^\circ\text{C}$ and $W_i = 3.3 \mu\text{g m}^{-3}$ for solid grey line).

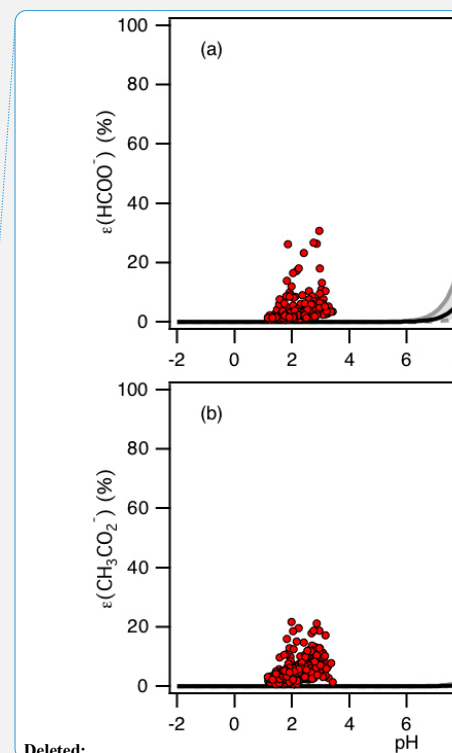
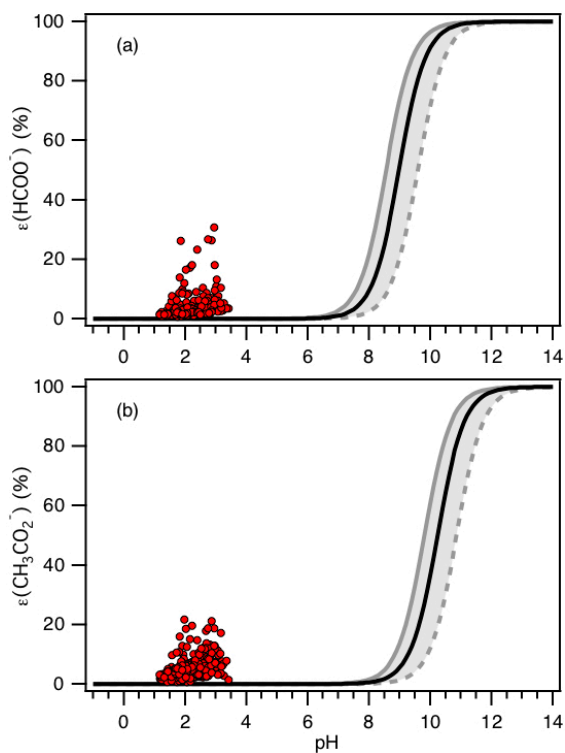


Figure 8: Analytically calculated S curves of $\epsilon(\text{HCOO}^-)$ and $\epsilon(\text{CH}_3\text{CO}_2^-)$ (solid black lines) and ambient data from 13 September to 6 October 2016 plotted against ISORROPIA-predicted particle pH (shown in panels (a) and (b), respectively). For the ambient data, a narrow range in W_i (0.5 to $4 \mu\text{g m}^{-3}$) and RH (20 to 90 %) is chosen to be close to the analytically calculated outputs. For the analytically calculated S curves, we used $\gamma_{\text{HCOOH}} = 0.334$ and $\gamma_{\text{CH}_3\text{COOH}} = 2.150$ (AIOMFAC predicted). We also assumed that $\gamma_{\text{H}^+}\gamma_{\text{HCOO}^-} = \gamma_{\text{H}^+}\gamma_{\text{CH}_3\text{COO}^-} = \gamma_{\text{H}^+}\gamma_{\text{NO}_3^-}$, and used the ISORROPIA-predicted $\gamma_{\text{H}^+}\gamma_{\text{NO}_3^-} = \sqrt{\gamma_{\text{H}^+}\gamma_{\text{NO}_3^-}} = 0.265$. The black lines are S curves calculated using the selected time period's average temperature ($23.4 \pm 4.0 \text{ }^\circ\text{C}$) and W_i ($1.6 \pm 1.7 \mu\text{g m}^{-3}$). The grey lines are S curves calculated using one standard deviation from the average temperature and W_i (i.e., temperature = $27.4 \text{ }^\circ\text{C}$ and $W_i = 0.5 \mu\text{g m}^{-3}$ for dotted grey line, temperature = $19.4 \text{ }^\circ\text{C}$ and $W_i = 3.3 \mu\text{g m}^{-3}$ for solid grey line).

Table 1: Comparisons between different field campaigns for particle pH, major inorganic ions and gases and meteorological conditions. All pH values were calculated using ISORROPIA-II run in forward mode. These statistics were previously compiled by Guo et al. (2017a). Campaign acronyms used here stand for the California Research at the Nexus of Air Quality and Climate Change (CalNex), Southern Oxidant and Aerosol Study (SOAS), and Southeastern Nexus of Air Quality and Climate (SENEX).

Campaign	CalNex		SOAS	SENEX	This study
Type	Ground		Ground	Aircraft	Ground
PM cut size	PM ₁	PM _{2.5} ^a	PM ₁ &PM _{2.5} ^b	PM ₁	PM ₁
Year	2010		2013	2013	2016
Season	(Early Summer)		Summer	Summer	Fall
Region/Location	SW US		SE US	SE US	SE US
SO ₄ ²⁻ , $\mu\text{g m}^{-3}$	2.86 ± 1.70	1.88 ± 0.69	1.73 ± 1.21	2.05 ± 0.80	1.6 ± 0.4
NO ₃ ⁻ , $\mu\text{g m}^{-3}$	3.58 ± 3.65	3.74 ± 1.53	0.08 ± 0.08	0.28 ± 0.09	0.20 ± 0.10
HNO ₃ , $\mu\text{g m}^{-3}$	6.65 ± 7.03	4.45 ± 3.59	0.36 ± 0.14	1.35 ± 0.66	0.50 ± 0.26
$\epsilon(\text{NO}_3^-)$	39 ± 16 %	51 ± 18 %	22 ± 16 %	18 ± 6 %	26 ± 15 %
Total NO ₃ ⁻ , $\mu\text{g m}^{-3}$	10.22 ± 9.74	8.19 ± 3.89	0.45 ± 0.26	1.63 ± 0.70	0.70 ± 0.28
NH ₄ ⁺ , $\mu\text{g m}^{-3}$	2.06 ± 1.67	1.79 ± 0.65	0.46 ± 0.34	1.06 ± 0.25	0.40 ± 0.20
NH ₃ , $\mu\text{g m}^{-3}$	1.37 ± 0.90	0.75 ± 0.61	0.39 ± 0.25	0.12 ± 0.19	5.79 ± 3.67
$\epsilon(\text{NH}_4^+)$	55 ± 25%	71 ± 19%	50 ± 25%	92 ± 11%	7 ± 5 %
Total NH ₄ ⁺ , $\mu\text{g m}^{-3}$	3.44 ± 1.81	2.54 ± 0.89	0.78 ± 0.50	1.17 ± 0.81	6.19 ± 3.68
Na ⁺ , $\mu\text{g m}^{-3}$	\	0.77 ± 0.39	0.03 ± 0.07	\	\
Cl ⁻ , μgm^{-3}	\	0.64 ± 0.48	0.02 ± 0.03	\	0.01 ± 0.01
RH, %	79 ± 17	87 ± 9	74 ± 16	72 ± 9	69 ± 18
T, °C	18 ± 4	18 ± 3	25 ± 3	22 ± 3	24 ± 4
W _i , $\mu\text{g m}^{-3}$	13.9 ± 18.1	29.8 ± 20.7	5.1 ± 3.8	3.2 ± 2.8	1.6 ± 1.7
pH	1.9 ± 0.5	2.7 ± 0.3	0.9 ± 0.6	1.1 ± 0.4	2.2 ± 0.6
Reference	(Guo et al., 2017a)		(Guo et al., 2015)	(Xu et al., 2016)	This study

^aOnly during the last week of CalNex.

^bPM_{2.5} was sampled in the first half and PM₁ sampled in the second half of the study. Various parameters were similar in both cases. Crustal components were higher, but are overall generally in low concentrations so the differences had minor effects. For example, PM_{2.5} Na⁺ was 0.06 ± 0.09 $\mu\text{g m}^{-3}$ and PM₁ Na⁺ was 0.01 ± 0.01 $\mu\text{g m}^{-3}$.

Characterization of Aerosol Composition, Aerosol Acidity and Organic Acid Partitioning at an Agriculture-Intensive Rural Southeastern U.S. Site

Theodora Nah,^{1,✉} Hongyu Guo,¹ Amy P. Sullivan,² Yunle Chen,¹ David J. Tanner,¹ Athanasios Nenes,^{1,3,4,5} Armistead Russell,⁶ Nga Lee Ng,^{1,3} L. Gregory Huey¹ and Rodney J. Weber^{1,*}

¹*School of Earth and Atmospheric Sciences, Georgia Institute of Technology, Atlanta, GA, USA*

²*Department of Atmospheric Science, Colorado State University, Fort Collins, CO, USA*

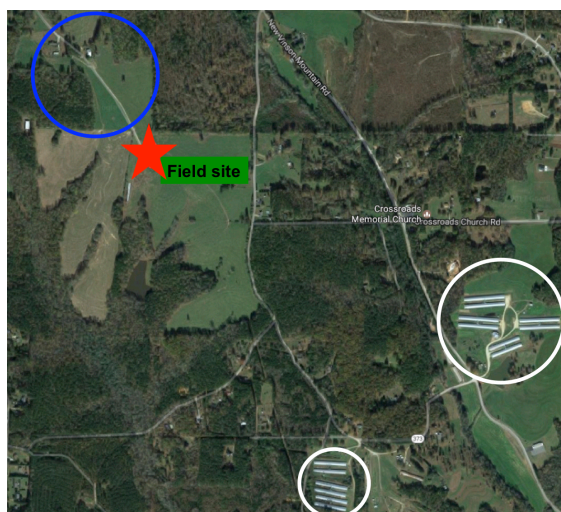
³*School of Chemical and Biomolecular Engineering, Georgia Institute of Technology, Atlanta, GA, USA*

⁴*ICE-HT, Foundation for Research and Technology, Hellas, 26504 Patras, Greece*

⁵*IERSD, National Observatory of Athens, P. Penteli, 15236, Athens, Greece*

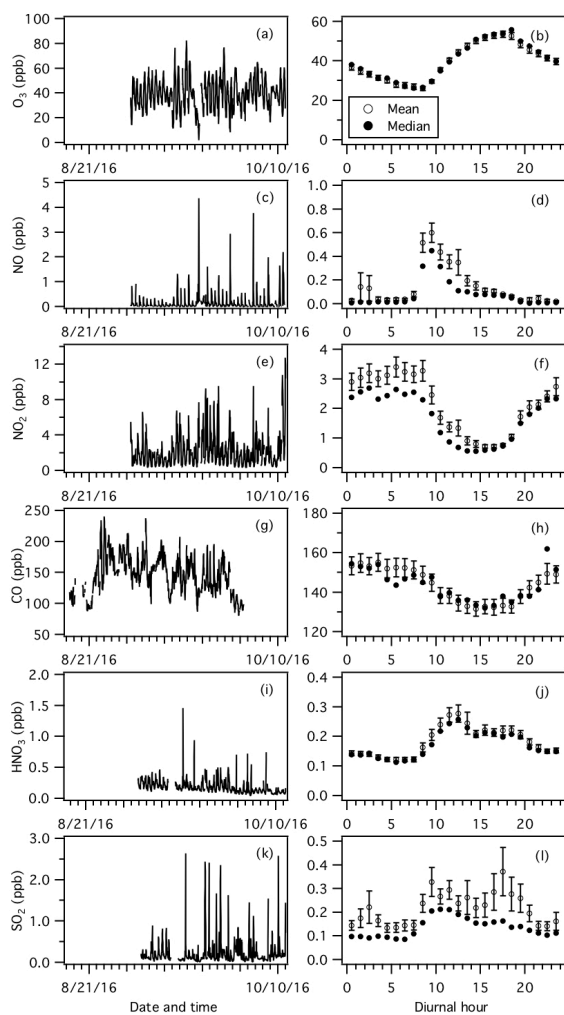
⁶*School of Civil and Environmental Engineering, Georgia Institute of Technology, Atlanta, GA, USA*

[✉]*Now at School of Energy and Environment, City University of Hong Kong, Kowloon, Hong Kong, China*



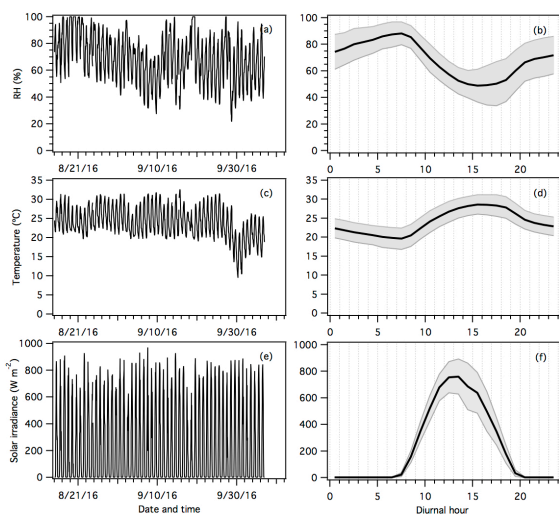
21

22 **Figure S1:** Map of the Yorkville field site (marked by the red diamond) and its surrounding areas
 23 (from Google Maps). Locations of nearby cattle-grazing pastures (north-west direction) and
 24 poultry CAFOs (south-east direction) are marked by the blue and white circles, respectively.



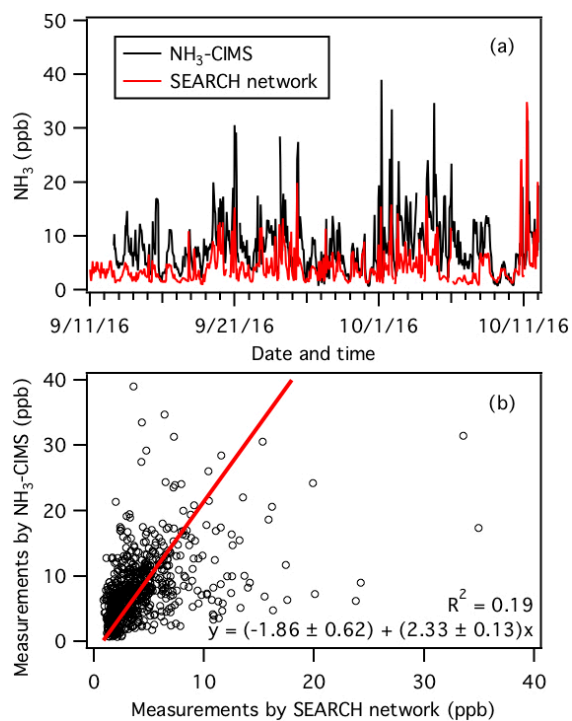
25

26 **Figure S2:** Time series and diurnal profiles of (a and b) O₃, (c and d) NO, (e and f) NO₂, (g and
 27 h) CO, (i and j) HNO₃, and (k and l) SO₂. Dates and times displayed are local time. All the
 28 concentrations represent averages in 1-hour intervals and the standard errors are plotted as error
 29 bars. O₃, NO, NO₂ and CO measurements were provided by the SEARCH network. HNO₃ and
 30 SO₂ were measured by the SF₆-CIMS.



31

32 **Figure S3:** Time series and diurnal profiles of (a and b) RH, (c and d) temperature, and (e and f)
 33 solar irradiance. Dates and times displayed are local time. In panels b, d and f, the lines within the
 34 shaded area represents the average values. The upper and lower boundaries of the shaded areas
 35 mark one standard deviation. RH, temperature and solar irradiance measurements were provided
 36 by the SEARCH network.



37

38 **Figure S4:** (a) Time series of NH₃ concentrations measured by the NH₃-CIMS and denuder-based
 39 instrument operated by the SEARCH network. (b) Comparison of NH₃ concentrations measured
 40 by the NH₃-CIMS and denuder-based instrument. The red line is the orthogonal distance regression
 41 fit to the data. All the data are displayed as 1-hour averages.

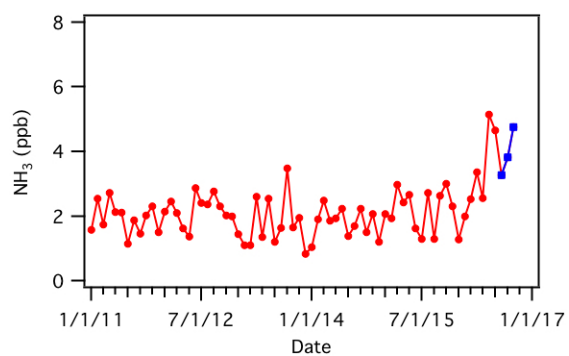


Figure S5: Monthly-averaged NH₃ concentrations at the Yorkville SEARCH monitoring site for 2011 to 2016. These measurements were made using the denuder-based instrument operated by the SEARCH network. Concentrations measured during this study (mid-August to mid-October 2016) are shown in blue.

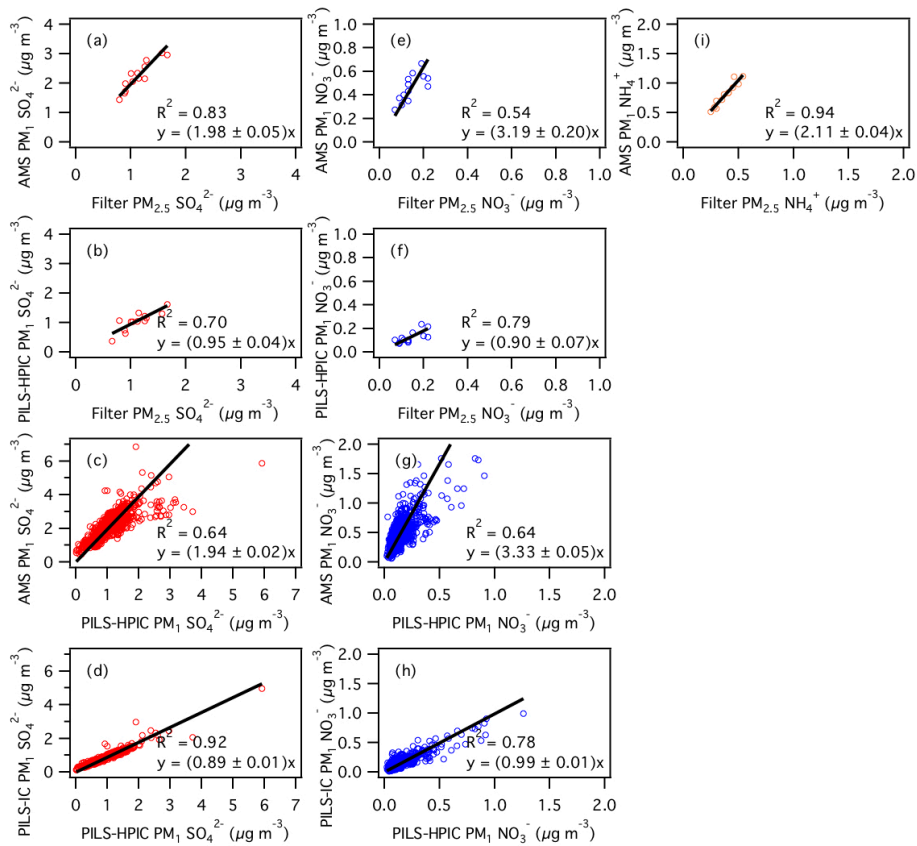


Figure S6: Aerosol (panels a to d) SO_4^{2-} , (panels e to h) NO_3^- , and (i) NH_4^+ comparisons between HR-ToF-AMS, PILS-IC, PILS-HPIC and filters for the entire field study. CDCE values were applied to the raw HR-ToF-AMS data to obtain the mass concentrations shown here (see main text for details). For comparisons between the HR-ToF-AMS, PILS-IC and PILS-HPIC data (panels c, d, g and h), the measurements are averaged over 1 hour intervals. For comparisons with filter data (panels a, b, e, f and i), the HR-ToF-AMS, PILS-IC and PILS-HPIC data are averaged over 24 hour intervals. Orthogonal regression fits are shown. Uncertainties in the fits are 1 standard deviation.

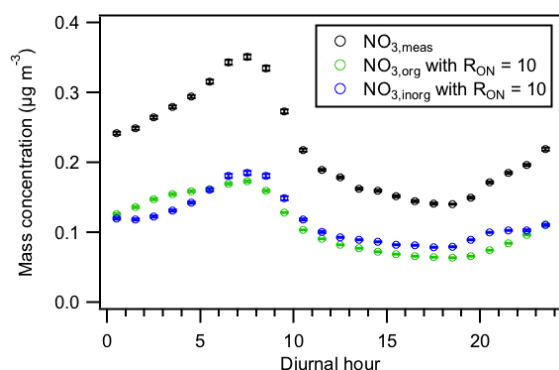


Figure S7: Diurnal profiles of the total nitrate functionality contributed by organic and inorganic nitrates ($\text{NO}_{3,\text{meas}}$), and the nitrate functionality solely from organic nitrates ($\text{NO}_{3,\text{org}}$) and inorganic nitrates ($\text{NO}_{3,\text{inorg}}$). $\text{NO}_{3,\text{org}}$ and $\text{NO}_{3,\text{inorg}}$ are estimated using the $\text{NO}^+/\text{NO}_2^+$ ratio method as described by Farmer et al. (2010) and Xu et al. (2015). Similar to Xu et al. (2015), we used a R_{ON} (defined here as the $\text{NO}^+/\text{NO}_2^+$ ratio for organic nitrates) value of 10 to calculate $\text{NO}_{3,\text{org}}$ and $\text{NO}_{3,\text{inorg}}$. All the data shown here represent averages in 1-hour intervals. Error bars shown are the standard errors.

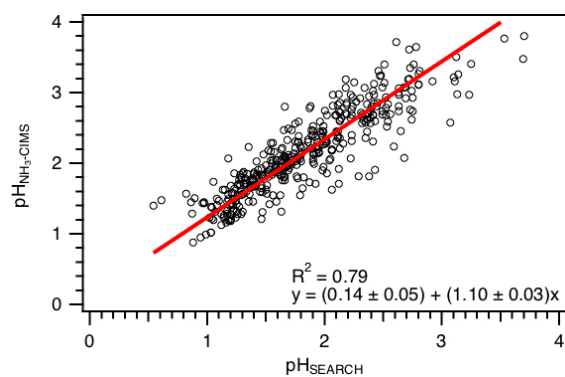
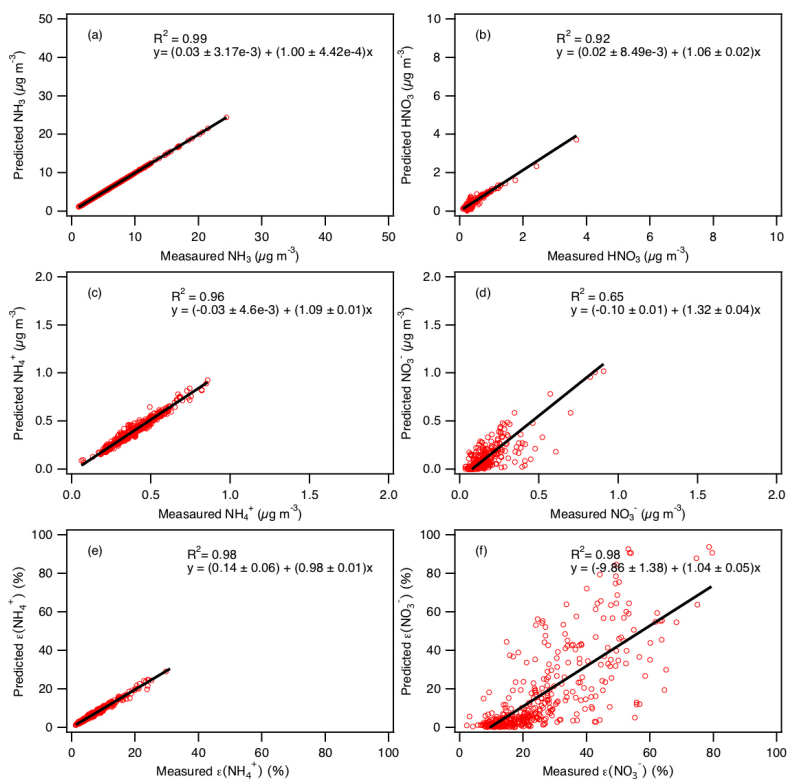
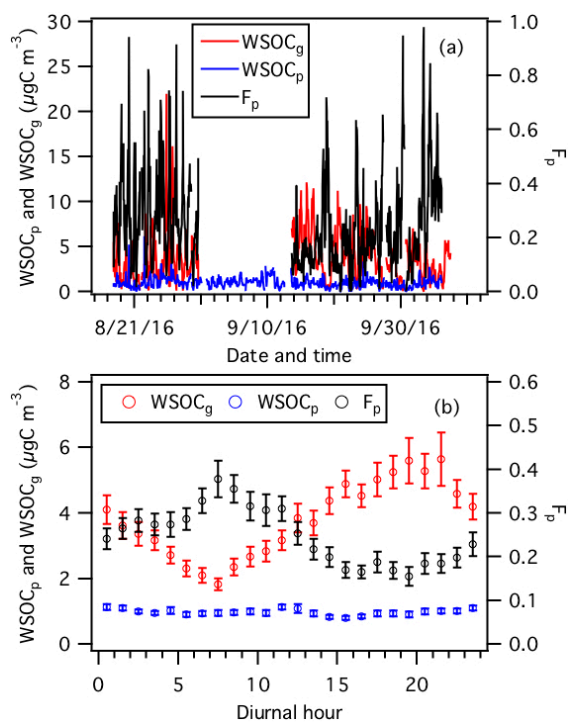


Figure S8: Comparison of predicted PM_{10} pH values determined using NH_3 -CIMS and SEARCH network's NH_3 measurements as ISORROPIA-II model inputs. The other model inputs are the same. The linear fit is obtained by orthogonal distance regression.



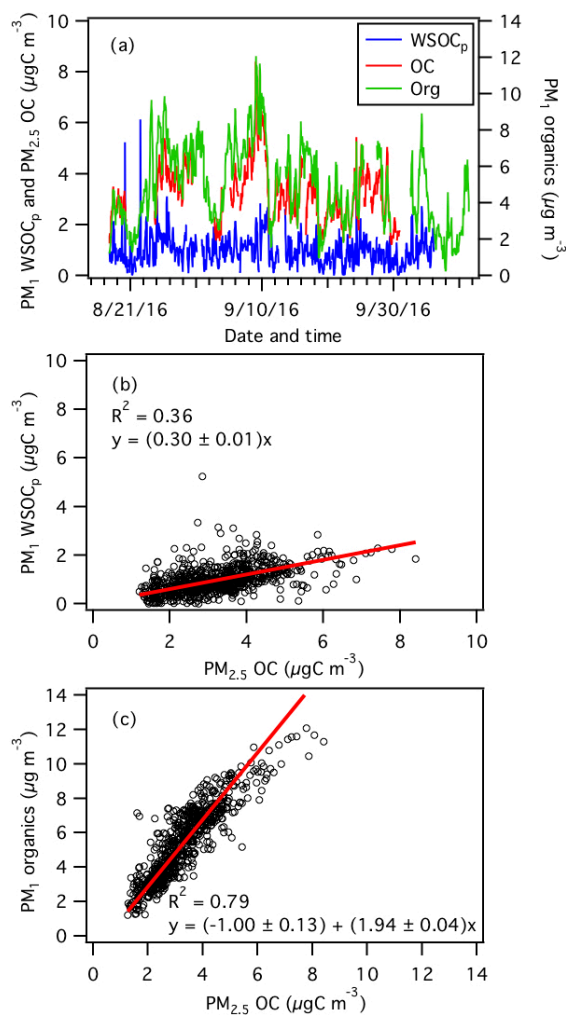
76

77 **Figure S9:** Comparisons of predicted and measured (a) NH_3 , (b) HNO_3 , (c) NH_4^+ , (d) NO_3^- , (e)
 78 $\epsilon(\text{NH}_4^+)$, and (f) $\epsilon(\text{NO}_3^-)$. Orthogonal regression fits are shown. Uncertainties in the fits are 1
 79 standard deviation.



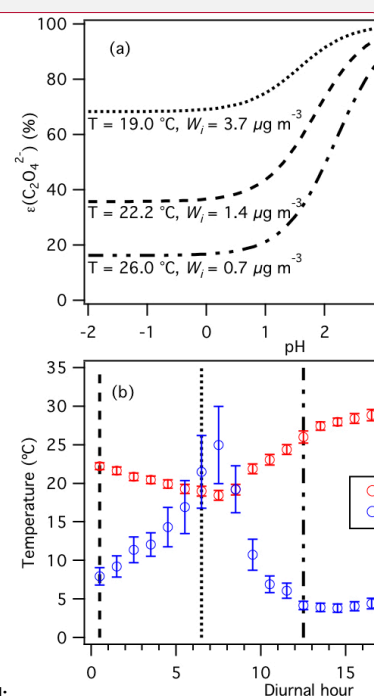
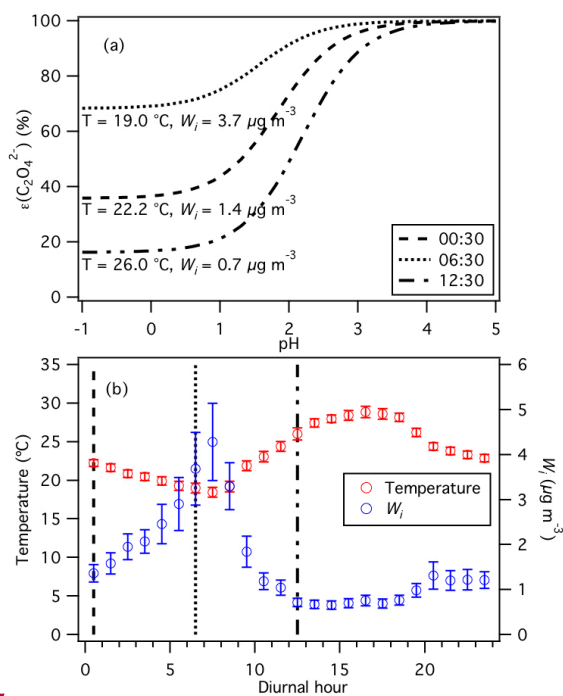
80

81 **Figure S10:** (a) Time series and (b) diurnal profiles of WSOC_g, WSOC_p and F_p. Dates and times
 82 displayed are local time. All the data shown here represent averages in 1-hour intervals. Error bars
 83 shown in panel (b) are the standard errors. $F_p = \text{WSOC}_p / (\text{WSOC}_p + \text{WSOC}_g)$.



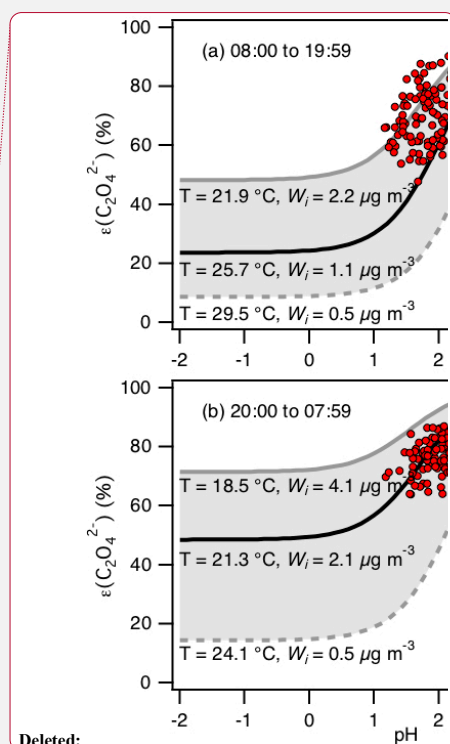
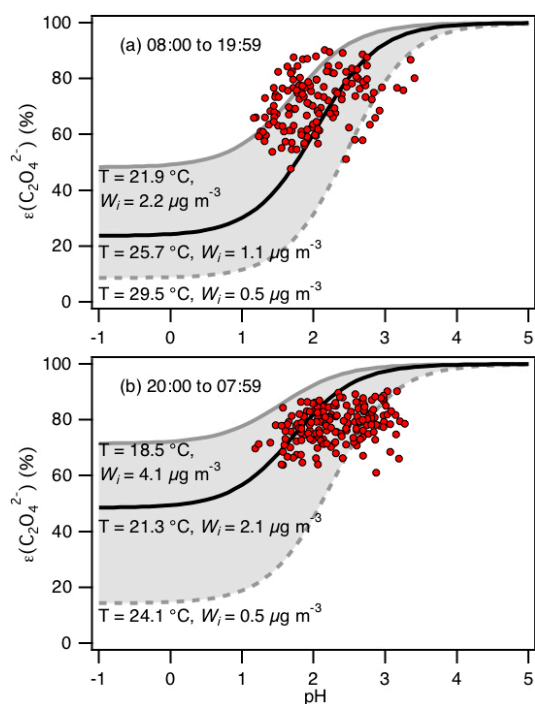
84

85 **Figure S11:** (a) Time series of HR-ToF-AMS organics, WSOC_p and OC. (b) Linear regression
 86 correlation between WSOC_p and OC. (c) Linear regression correlation between HR-ToF-AMS
 87 organics and OC. All the data shown here represent averages in 1-hour intervals. Note that OC
 88 measurements are $PM_{2.5}$, while WSOC_p and HR-ToF-AMS organics measurements are $PM_{1.1}$.
 89 Linear fits are obtained by orthogonal distance regression.



Deleted:

Figure S12: (a) Analytically calculated S curves of $\epsilon(\text{C}_2\text{O}_4^{2-})$ at different times of the day: 00:30, 06:30 and 12:30. These S curves are calculated using values obtained from (b) the diurnal profiles of temperature and W_i . The set of 1-hour average temperatures and W_i at diurnal hours 00:30, 06:30 and 12:30 is used to calculate each S curve shown in panel (a). Similar to Fig. 7, we used $\gamma_{\text{C}_2\text{H}_2\text{O}_4} = 0.0492$ (AIOMFAC predicted) and assumed that $\gamma_{\text{H}^+ - \text{NO}_3^-} = \sqrt{\gamma_{\text{H}^+} \gamma_{\text{NO}_3^-}} = \sqrt{\gamma_{\text{H}^+} \gamma_{\text{C}_2\text{HO}_4^-}} = 0.265$ (ISORROPIA-II predicted) to generate these S curves.



Deleted:

98

99 **Figure S13:** Analytically calculated S curve of $\epsilon(\text{C}_2\text{O}_4^{2-})$ and ambient data from 13 September to
 100 6 October 2016 plotted against ISORROPIA-predicted particle pH. For the ambient data, a narrow
 101 range in W_i (0.5 to $4 \mu\text{g m}^{-3}$) and RH (20 to 90%) is chosen to be close to the analytically calculated
 102 outputs. We divided the ambient data into two sets: panel (a) 08:00 to 19:59, and panel (b) 20:00
 103 to 07:59. For both analytically calculated S curves, we used $\gamma_{\text{C}_2\text{H}_2\text{O}_4} = 0.0492$ (AIOMFAC
 104 predicted). We also assumed that $\gamma_{\text{H}^+} + \gamma_{\text{C}_2\text{HO}_4^-} = \gamma_{\text{H}^+} + \gamma_{\text{NO}_3^-}$, and used the ISORROPIA-predicted
 105 $\gamma_{\text{H}^+ - \text{NO}_3^-} = \sqrt{\gamma_{\text{H}^+} + \gamma_{\text{NO}_3^-}} = 0.265$. In panel (a), we used the average temperature and W_i (25.7 ± 3.8
 106 $^\circ\text{C}$ and $1.1 \pm 1.1 \mu\text{g m}^{-3}$) for the data between 08:00 to 19:59 to calculate the S curve (black line).
 107 In panel (b), we used the average temperature and W_i (21.3 ± 2.8 $^\circ\text{C}$ and $2.1 \pm 2.0 \mu\text{g m}^{-3}$) for the
 108 data between 20:00 to 07:59 to calculate the S curve (black line). Grey lines in both panels are S
 109 curves calculated using one standard deviation from the average temperature and W_i for the two
 110 datasets. In panel (a), the dotted grey line is the S curve calculated using 29.5 $^\circ\text{C}$ and $0.5 \mu\text{g m}^{-3}$

112 while the solid grey line is the S curve calculated using 21.9 °C and 2.2 $\mu\text{g m}^{-3}$. In panel (b), the
113 dotted grey line is the S curve calculated using 24.1 °C and 0.5 $\mu\text{g m}^{-3}$ while the solid grey line is
114 the S curve calculated using 18.5 °C and 4.1 $\mu\text{g m}^{-3}$.

115

116

117

118

119

120

121

122

123

124

125

126

127

128

129

130

131

132

Table S1: List of gas-phase acids measured by SF₆-CIMS, and their measurement uncertainties and detection limits.

Acid	Measurement uncertainty (%)	Detection limits (ppb) ^a
Nitric acid	13	0.20
Formic acid	12	0.03
Acetic acid	12	0.06
Oxalic acid	14	1×10^{-3}
Butyric acid	14	0.03
Glycolic acid	22	2×10^{-3}
Propionic acid	14	6×10^{-3}
Valeric acid	22	0.01
Malonic acid	25	7×10^{-4}
Succinic acid	25	3×10^{-3}

^aDetection limits are approximated from 3 times the standard deviation values (3σ) of the ion signals measured during background mode. Shown here are the average detection limits of the organic acids for 2.5 min integration periods which corresponds to the length of a background measurement at a 0.04 s duty cycle for each mass.

152 **S1. SF₆-CIMS calibration of gas-phase HNO₃ and organic acids**

153 Detailed descriptions of post-field laboratory calibrations of HNO₃, oxalic, butyric,
154 glycolic, propionic, valeric, malonic and succinic acids can be found in Nah et al. (2018). The
155 response of the CIMS acid signals were measured relative to the sensitivity of ³⁴SO₂ in these
156 calibration measurements.

157 The HNO₃ calibration source was a permeation tube (KIN-TEK) whose emission rate was
158 measured using UV optical absorption (Neuman et al., 2003). Solid or liquid samples of oxalic
159 (Sigma Aldrich, ≥ 99 %), butyric (Sigma Aldrich, ≥ 99 %), glycolic (Sigma Aldrich, 99 %),
160 propionic (Sigma Aldrich, ≥ 99.5 %), valeric (Sigma Aldrich, ≥ 99 %), malonic (Sigma Aldrich,
161 ≥ 99.5 %) and succinic (Sigma Aldrich, 99 %) acids were used in calibration measurements. The
162 acid sample was placed in a glass impinger, which was immersed in a water bath at a fixed
163 temperature to provide a constant vapor pressure. For oxalic, butyric, glycolic, propionic and
164 valeric acids, the water bath temperature was set to 0 °C. For malonic and succinic acids, the water
165 bath temperature was set to 40 °C in order to generate large enough gas phase concentrations for
166 calibration. 6 to 10 mL min⁻¹ of nitrogen gas (N₂) was passed over the organic acid in the glass
167 impinger. This organic acid air stream was diluted with different N₂ flows (1 to 5 L min⁻¹) to obtain
168 different mixing ratios of the organic acid. We calculated the mixing ratios based on the acid's
169 emission rate from the impinger or the acid's vapor pressure. Emission rates of gas-phase oxalic,
170 malonic and succinic acids from the impinger were measured by scrubbing the output of the
171 impinger in deionized water, followed by ion chromatography analysis. We measured the vapor
172 pressures of butyric and propionic acids at 0 °C using a capacitance manometer (MKS
173 Instruments). We estimated the vapor pressures of glycolic and valeric acids at 0 °C using their
174 literature vapor pressures at 25 °C and enthalpies of vaporization (Daubert and Danner, 1989; Lide,
175 1995; Acree and Chickos, 2010).

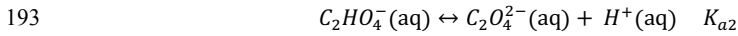
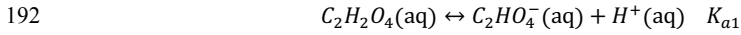
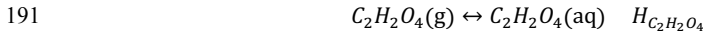
176 **S2. WSOC_p and OC**

177 We estimated the water-soluble fraction of OC by comparing the WSOC_p and OC
178 measurements. The time series of organics, WSOC_p and OC are shown in Fig. S11a. As shown in
179 Fig. S11b, WSOC_p is moderately correlated with OC at the site. The orthogonal distance regression
180 fit suggests that 30 % of the OC is water-soluble (estimated measurement uncertainty of 19 %),

181 which is significantly smaller than the fraction (61 %) measured during the SOAS study (Xu et al.,
 182 2017). This difference may be due, in part, to the WSOC_p/OC ratio for this study being under-
 183 estimated. WSOC_p are PM₁ measurements while OC are PM_{2.5} measurements. This is in contrast
 184 to the SOAS study where both WSOC_p and OC are PM_{2.5} measurements. PM₁ organics mass
 185 concentration is highly correlated with OC and has an orthogonal distance regression slope of 1.94
 186 (Fig. S9c), which is similar to the value (1.92) reported for the SOAS study (Xu et al., 2017).

187 S3. C₂H₂O₄- C₂O₄²⁻ partitioning

188 Here, we show the detailed derivation of equation (4) in that paper. Equilibrium between
 189 gaseous C₂H₂O₄ and particle-phase C₂O₄²⁻ involves the dissolution of C₂H₂O₄ into the aqueous
 190 phase (assuming particles are liquids), followed by dissociation of the dissolved C₂H₂O₄:



194 for which the reaction equilibriums are expressed as follows:

$$195 \quad H_{C_2H_2O_4} = \gamma_{C_2H_2O_4} [C_2H_2O_4] / p_{C_2H_2O_4} \quad (1)$$

$$196 \quad K_{a1} = \frac{\gamma_{H^+} [H^+] \gamma_{C_2HO_4^-} [C_2HO_4^-]}{\gamma_{C_2H_2O_4} [C_2H_2O_4]} \quad (2)$$

$$197 \quad K_{a2} = \frac{\gamma_{H^+} [H^+] \gamma_{C_2O_4^{2-}} [C_2O_4^{2-}]}{\gamma_{C_2HO_4^-} [C_2HO_4^-]} \quad (3)$$

198 where $H_{C_2H_2O_4}$ (mole L⁻¹ atm⁻¹) is the Henry's law constant for oxalic acid, K_{a1} and K_{a2} (mole L⁻¹)
 199 are the first and second acid dissociation constants for oxalic acid, $p_{C_2H_2O_4}$ (atm) is the partial
 200 pressure of oxalic acid in the atmosphere, and γ_i 's are activity coefficients. In equations (1) to (3),
 201 [x] represents aqueous concentrations (mole L⁻¹).

202 The total dissolved C₂H₂O₄ or particle-phase oxalate ($C_2O_4^T$) can be expressed as:

$$203 \quad [C_2HO_4^T] = [C_2H_2O_4] + [C_2HO_4^-] + [C_2O_4^{2-}] \quad (4)$$

204 Using equations (1) to (3), $[C_2O_4^{T}]$ can be expressed as:

$$205 \quad [C_2O_4^T] = H_{C_2H_2O_4} p_{C_2H_2O_4} \left(\frac{1}{\gamma_{C_2H_2O_4}} + \frac{K_{a1}}{\gamma_{H^+} + \gamma_{C_2HO_4^-} [H^+]} + \frac{K_{a1}K_{a2}}{\gamma_{H^+} + \gamma_{C_2O_4^{2-}} [H^+]^2} \right) \quad (5)$$

206 The ideal gas law gives:

$$207 \quad c(C_2H_2O_4) = \frac{p_{C_2H_2O_4}}{RT} \quad (6)$$

208 where R is the gas constant, T is temperature, and $c(x)$ represents concentration per volume of air
209 (mole m^{-3}). The particle-phase fraction of oxalate can then be expressed as:

$$210 \quad \varepsilon(C_2O_4^{2-}) = \frac{c(C_2O_4^T)}{c(C_2H_2O_4) + c(C_2O_4^T)} = \frac{[C_2HO_4^-]W_i}{c(C_2H_2O_4) + [C_2HO_4^-]W_i} \quad (7)$$

211 where W_i is the particle liquid water content associated with inorganic species ($\mu g\ m^{-3}$; mass per
212 volume of air). Note that the particle liquid water content associated with organic species is not
213 considered in this case, but it can be included. Alternatively, the measured particle water can be
214 used.

215 By putting equations (5) and (6) into equation (7), $\varepsilon(C_2O_4^{2-})$ can be expressed as:

$$216 \quad \varepsilon(C_2O_4^{2-}) = \frac{H_{C_2H_2O_4} W_i RT \left(\frac{1}{\gamma_{C_2H_2O_4}} + \frac{K_{a1}}{\gamma_{H^+} + \gamma_{C_2HO_4^-} [H^+]} + \frac{K_{a1}K_{a2}}{\gamma_{H^+} + \gamma_{C_2O_4^{2-}} [H^+]^2} \right)}{1 + H_{C_2H_2O_4} W_i RT \left(\frac{1}{\gamma_{C_2H_2O_4}} + \frac{K_{a1}}{\gamma_{H^+} + \gamma_{C_2HO_4^-} [H^+]} + \frac{K_{a1}K_{a2}}{\gamma_{H^+} + \gamma_{C_2O_4^{2-}} [H^+]^2} \right)} \quad (8)$$

217 At 298 K, $K_{a1} = 5.62 \times 10^{-2}$ mole L^{-1} and $K_{a2} = 1.55 \times 10^{-4}$ mole L^{-1} (Haynes, 2014). Assuming
218 that $\gamma_{H^+} = 1$, $K_{a1}K_{a2} \ll \gamma_{H^+} + \gamma_{C_2O_4^{2-}} [H^+]^2$ for the conditions of our study. Hence, equation (8)
219 can be simplified to:

$$220 \quad \varepsilon(C_2O_4^{2-}) \cong \frac{H_{C_2H_2O_4} W_i RT \left(\frac{\gamma_{H^+} + \gamma_{C_2HO_4^-} [H^+] + K_{a1}}{\gamma_{C_2H_2O_4}} \right)}{\gamma_{H^+} + \gamma_{C_2HO_4^-} [H^+] + H_{C_2H_2O_4} W_i RT \left(\frac{\gamma_{H^+} + \gamma_{C_2HO_4^-} [H^+] + K_{a1}}{\gamma_{C_2H_2O_4}} \right)} \quad (9)$$

221 After accounting for the SI units and substituting $[H^+] = 10^{-pH}$, equation (9) becomes:

$$\varepsilon(C_2O_4^{2-}) \cong \frac{H_{C_2H_2O_4} W_i RT \left(\frac{Y_H + Y_{C_2HO_4^-}}{Y_{C_2H_2O_4}} 10^{-pH + K_{a1}} \right) \times 0.987 \times 10^{-14}}{Y_H + Y_{C_2HO_4^-} 10^{-pH} + H_{C_2H_2O_4} W_i RT \left(\frac{Y_H + Y_{C_2HO_4^-}}{Y_{C_2H_2O_4}} 10^{-pH + K_{a1}} \right) \times 0.987 \times 10^{-14}} \quad (10)$$

Note that 0.987×10^{-14} comes from using $R = 8.314 \text{ m}^3 \text{ Pa K}^{-1} \text{ mol}^{-1}$, and hence needing to convert 1 atm to 1 Pa and 1 L to 1 μg . We used the average of $H_{C_2H_2O_4}$ values provided by Clegg et al. (1996), Compernelle and Muller (2014) and Saxena and Hildemann (1996) ($6.11 \times 10^8 \text{ mole L}^{-1} \text{ atm}^{-1}$ at 25 °C), and accounted for the effect of temperature using equation 19 in Sander (2015). Although K_{a1} also depends on temperature, the K_{a1} value at 25 °C (5.62×10^{-2} , (Haynes, 2014)) is used for all the oxalic acid S curve calculations in this paper since equations that determine temperature-dependent K_{a1} values are not available. In addition, the temperatures observed in this study are close to 25 °C.

Figure S12 provides a conceptual picture of how the relationship between $\varepsilon(C_2O_4^{2-})$ and particle pH can change based on the time of the day. Different S curves for $\varepsilon(C_2O_4^{2-})$ are calculated using equation (10) and 1-hour average values obtained from the diurnal profiles of temperature and W_i (specifically at 00:30, 06:30 and 12:30). The S curves are shown to differ substantially due to the diurnal variations of temperature and W_i . For example, a decrease in temperature and an increase in W_i from 00:30 to 06:30 will result in the S curve shifting to the left, which indicates that a substantially higher fraction of gas-phase oxalic acid will partition to the particle phase for a given particle pH at 06:30 compared to at 00:30. Higher W_i also increases the fraction of oxalate that partitions to the particle phase due solely to solubility, as seen from the plateau regions at low pH in Fig. S12. Conversely, an increase in temperature and a decrease in W_i from 06:30 to 12:30 will result in a considerably lower fraction of gas-phase oxalic acid partitioning to the particle phase for a given particle pH at 12:30 compared to at 06:30.

S4. PILS-HPIC denuder efficiency

Post-field laboratory experiments were performed to determine if disagreements between the measured and predicted molar fractions of formic and acetic acid in the particle phase were due to positive biases in particle-phase PILS-HPIC measurements as a result of less than 100 % gas removal denuder efficiency and uptake of gases in the PILS liquid system. While experiments were done solely with formic acid, similar results are expected for acetic acid. In these

249 experiments, liquid formic acid (Sigma Aldrich, $\geq 99\%$) was diluted with ultrapure deionized
 250 water and placed in a bubbler. A flow of 18 mL min^{-1} of N_2 was passed through the formic acid in
 251 the bubbler. This formic acid air stream was then passed through a nafion dryer and diluted with
 252 52 L min^{-1} of N_2 . Two experiments were performed. In the first experiment, the diluted formic
 253 acid air flow was introduced directly into the PILS, which was connected to a Metrohm 761
 254 Compact IC (Metrohm AG). In the second experiment, the diluted formic acid air flow was passed
 255 through a 28 cm parallel plate carbon denuder (Sunset Lab) prior to introduction into the PILS-IC
 256 system.

257 Our experiments showed that the IC detected formate when the diluted formic acid air flow
 258 was introduced directly into the PILS-IC system. IC analysis revealed that the gas-phase formic
 259 acid concentration was $\sim 75\text{ }\mu\text{g m}^{-3}$. However, no formate was detected above the limit of detection
 260 ($0.02\text{ }\mu\text{g m}^{-3}$) when the diluted formic acid air flow was passed through the carbon denuder prior
 261 to introduction into the PILS-IC system. These measurements indicated that the carbon denuder
 262 has a $\geq 99.97\%$ formic acid gas removal efficiency. Hence, these experiments indicate that the
 263 carbon denuder removes the formic acid gas completely. We conclude that disagreements between
 264 the measured and predicted molar fractions of formic and acetic acid in the particle phase were not
 265 due to positive biases in particle-phase formate and acetate PILS-HPIC measurements as a result
 266 of less than 100% gas removal denuder efficiency.

267 **S5. Particle-phase formic and acetic acid dimers**

268 Previous studies have shown that formic and acetic acid dimers may form in the aqueous
 269 phase (Schrier et al., 1964; Gilson et al., 1997; Chen et al., 2008). If the aforementioned acid
 270 dimers are present in aerosols, equilibrium between gas-phase formic/acetic acid (denoted as HA)
 271 and particle-phase formate/acetate (denoted as A^-) will differ from that predicted assuming no
 272 dimers existed, as done in the main text.

273 The dissolution of HA into the aqueous phase (assuming particles are liquids), followed by
 274 the formation of particle-phase dimers (denoted as $(\text{HA})_2$) and dissociation of the dissolved HA:





for which the reaction equilibriums are expressed as follows:

$$H_{HA} = \gamma_{HA}[HA]/p_{HA} \quad (11)$$

$$K_{dim} = \frac{[(HA)_2]}{[HA]^2} \quad (12)$$

$$K_{a1} = \frac{\gamma_{A^-}[A^-]\gamma_{H^+}[H^+]}{\gamma_{HA}[HA]} \quad (13)$$

where H_{HA} (mole L⁻¹ atm⁻¹) is the Henry's law constant for formic or acetic acid, K_{a1} (mole L⁻¹) is the first acid dissociation constants for formic or acetic acid, p_{HA} (atm) is the partial pressure of formic or acetic acid in the atmosphere, K_{dim} (L mole⁻¹) is the dimerization constant, and γ_i 's are activity coefficients. In equations (11) to (13), [x] represents aqueous concentrations (mole L⁻¹).

The total dissolved formate or acetate (A^T) can be expressed as:

$$[A^T] = [HA] + [A^-] + [(HA)_2] \quad (14)$$

Using equations (11) to (13), $[A^T]$ can be expressed as:

$$[A^T] = H_{HA}p_{HA} \left(\frac{1}{\gamma_{HA}} + \frac{K_{a1}}{\gamma_{H^+}\gamma_{A^-}[H^+]} + \frac{K_{dim}H_{HA}p_{HA}}{\gamma_{HA}\gamma_{HA}} \right) \quad (15)$$

The ideal gas law gives:

$$c(HA) = \frac{p_{HA}}{RT} \quad (16)$$

where R is the gas constant, T is temperature, and $c(x)$ represents concentration per volume of air (mole m⁻³). The particle-phase fraction of formate or acetate can then be expressed as:

$$\varepsilon(A^-) = \frac{c(A^T)}{c(HA) + c(A^T)} = \frac{[A^T]W_i}{c(HA) + [A^T]W_i} \quad (17)$$

where W_i is the particle liquid water content associated with inorganic species (μg m⁻³; mass per volume of air). Particle liquid water content associated with organic species is not considered in this case, but it can be included. Alternatively, the measured particle water can be used.

By putting equations (15) and (16) into equation (17), and accounting for the SI units, $\varepsilon(A^-)$ can ultimately be expressed as:

$$\varepsilon(A^-) = \frac{H_{HA} W_i RT \left(\frac{1}{\gamma_{HA}} + \frac{K_{a1}}{\gamma_{H^+} \gamma_{A^-} 10^{-pH}} + \frac{K_{dim} H_{HA} p_{HA}}{\gamma_{HA} \gamma_{HA}} \right) \times 0.987 \times 10^{-14}}{1 + H_{HA} W_i RT \left(\frac{1}{\gamma_{HA}} + \frac{K_{a1}}{\gamma_{H^+} \gamma_{A^-} 10^{-pH}} + \frac{K_{dim} H_{HA} p_{HA}}{\gamma_{HA} \gamma_{HA}} \right) \times 0.987 \times 10^{-14}} \quad (18)$$

At 298 K, K_{a1} values are 1.78×10^{-4} mole L⁻¹ and 1.75×10^{-5} mole L⁻¹ for formic and acetic acid, respectively (Haynes, 2014). K_{dim} values are 0.56 L mole⁻¹ and 0.92 L mole⁻¹ for formic and acetic acid, respectively (Chen et al., 2008). Temperature-dependent H_{HA} values for formic and acetic acid can be obtained from Sander (2015). p_{HA} can be calculated from the measured gas-phase formic or acetic acid concentrations ($\mu\text{g m}^{-3}$) and the ideal gas law. We used the web version of AIOMFAC (www.aiomfac.caltech.edu) (Zuend et al., 2008; Zuend et al., 2011; Zuend et al., 2012) to compute study-averaged γ_{HA} values of 0.334 and 2.150 for formic and acetic acid, respectively. We assumed that $\gamma_{H^+} \gamma_{A^-} = \gamma_{H^+} \gamma_{NO_3^-} = 0.07$ for both formic and acetic acid.

Comparison of S curves generated from equation (18) and those generated from equations (5) and (6) in the main text (which assumed that no dimers existed) showed that accounting for the presence of acid dimers increased predicted $\varepsilon(A^-)$ values by less than 1 % for particle pH 0.9 to 3.8 (i.e., pH values in this study). S curves generated by equation (18) also do not match our measured molar fractions of formic and acetic acid in the particle phase. This analysis shows that the molar fractions of formic and acetic acid in the particle phase do not change substantially when the presence of particle-phase acid dimers is accounted for due to the somewhat low H_{HA} values for formic and acetic acid. Hence, disagreements between the measured and predicted molar fractions of formic and acetic acid in the particle phase are not due to the presence of particle-phase formic and acetic acid dimers.

323 **References**

- 324 Acree, W., and Chickos, J. S.: Phase Transition Enthalpy Measurements of Organic and
325 Organometallic Compounds. Sublimation, Vaporization and Fusion Enthalpies From 1880 to
326 2010, J. Phys. Chem. Ref. Data, 39, 942, 10.1063/1.3309507, 2010.
- 327 Chen, J. H., Brooks, C. L., and Scheraga, H. A.: Revisiting the carboxylic acid dimers in aqueous
328 solution: Interplay of hydrogen bonding, hydrophobic interactions, and entropy, Journal of
329 Physical Chemistry B, 112, 242-249, 10.1021/jp074355h, 2008.
- 330 Clegg, S. L., Brimblecombe, P., and Khan, L.: The Henry's law constant of oxalic acid and its
331 partitioning into the atmospheric aerosol, Idojaras, 100, 51-68, 1996.
- 332 Compernelle, S., and Muller, J. F.: Henry's law constants of diacids and hydroxy polyacids:
333 recommended values, Atmos. Chem. Phys., 14, 2699-2712, 10.5194/acp-14-2699-2014, 2014.
- 334 Daubert, T. E., and Danner, R. P.: Physical and thermodynamic properties of pure chemicals: data
335 compilation, Taylor & Francis, Washington, DC, 1989.
- 336 Farmer, D. K., Matsunaga, A., Docherty, K. S., Surratt, J. D., Seinfeld, J. H., Ziemann, P. J., and
337 Jimenez, J. L.: Response of an aerosol mass spectrometer to organonitrates and organosulfates and
338 implications for atmospheric chemistry, Proceedings of the National Academy of Sciences of the
339 United States of America, 107, 6670-6675, 10.1073/pnas.0912340107, 2010.
- 340 Gilson, M. K., Given, J. A., Bush, B. L., and McCammon, J. A.: The statistical-thermodynamic
341 basis for computation of binding affinities: A critical review, Biophysical Journal, 72, 1047-1069,
342 10.1016/s0006-3495(97)78756-3, 1997.
- 343 Haynes, W. M.: CRC handbook of chemistry and physics: A ready-reference book of chemical
344 and physical data. , Boca Raton: CRC Press, 2014.
- 345 Lide, D. R.: CRC handbook of chemistry and physics: a ready-reference book of chemical and
346 physical data, CRC Press, Boca Raton, FL, 1995.

347 Nah, T., Ji, Y., Tanner, D. J., Guo, H., Sullivan, A. P., Ng, N. L., Weber, R. J., and Huey, L. G.:
 348 Real-time measurements of gas-phase organic acids using SF₆- chemical ionization mass
 349 spectrometry, *Atmos. Meas. Tech. Discuss.*, 2018, 1-40, 10.5194/amt-2018-46, 2018.

350 Neuman, J. A., Ryerson, T. B., Huey, L. G., Jakoubek, R., Nowak, J. B., Simons, C., and
 351 Fehsenfeld, F. C.: Calibration and evaluation of nitric acid and ammonia permeation tubes by UV
 352 optical absorption, *Environmental Science & Technology*, 37, 2975-2981, 10.1021/es0264221,
 353 2003.

354 Sander, R.: Compilation of Henry's law constants (version 4.0) for water as solvent, *Atmos. Chem.*
 355 *Phys.*, 15, 4399-4981, 10.5194/acp-15-4399-2015, 2015.

356 Saxena, P., and Hildemann, L. M.: Water-soluble organics in atmospheric particles: A critical
 357 review of the literature and application of thermodynamics to identify candidate compounds,
 358 *Journal of Atmospheric Chemistry*, 24, 57-109, 10.1007/bf00053823, 1996.

359 Schrier, E. E., Pottle, M., and Scheraga, H. A.: The Influence of Hydrogen and Hydrophobic Bonds
 360 on the Stability of the Carboxylic Acid Dimers in Aqueous Solution, *Journal of the American*
 361 *Chemical Society*, 86, 3444-3449, 10.1021/ja01071a009, 1964.

362 Xu, L., Suresh, S., Guo, H., Weber, R. J., and Ng, N. L.: Aerosol characterization over the
 363 southeastern United States using high-resolution aerosol mass spectrometry: spatial and seasonal
 364 variation of aerosol composition and sources with a focus on organic nitrates, *Atmos. Chem. Phys.*,
 365 15, 7307-7336, 10.5194/acp-15-7307-2015, 2015.

366 Xu, L., Guo, H. Y., Weber, R. J., and Ng, N. L.: Chemical Characterization of Water-Soluble
 367 Organic Aerosol in Contrasting Rural and Urban Environments in the Southeastern United States,
 368 *Environmental Science & Technology*, 51, 78-88, 10.1021/acs.est.6b05002, 2017.

369 Zuend, A., Marcolli, C., Luo, B. P., and Peter, T.: A thermodynamic model of mixed organic-
 370 inorganic aerosols to predict activity coefficients, *Atmos. Chem. Phys.*, 8, 4559-4593,
 371 10.5194/acp-8-4559-2008, 2008.

372 Zuend, A., Marcolli, C., Booth, A. M., Lienhard, D. M., Soonsin, V., Krieger, U. K., Topping, D.
 373 O., McFiggans, G., Peter, T., and Seinfeld, J. H.: New and extended parameterization of the

374 thermodynamic model AIOMFAC: calculation of activity coefficients for organic-inorganic
375 mixtures containing carboxyl, hydroxyl, carbonyl, ether, ester, alkenyl, alkyl, and aromatic
376 functional groups, *Atmos. Chem. Phys.*, 11, 9155-9206, 10.5194/acp-11-9155-2011, 2011.

377 Zuend, A., Marcolli, C., Luo, B. P., and Peter, T.: A thermodynamic model of mixed organic-
378 inorganic aerosols to predict activity coefficients (vol 8, pg 4559, 2008), *Atmos. Chem. Phys.*, 12,
379 10075-10075, 10.5194/acp-12-10075-2012, 2012.

380